The Pennsylvania State University

The Graduate School

WATER-MEDIATED INTERACTIONS IN AQUEOUS SALT SOLUTIONS

A Dissertation in

Chemistry

by

Chad Isaac Drexler

Submitted in Partial Fulfillment
of the Requirements
for the Degree of

Doctor of Philosophy

May 2021

The dissertation of Chad Isaac Drexler was reviewed and approved by the following:

Paul S. Cremer
J. Lloyd Huck Chair in Natural Sciences
Professor of Chemistry & Biochemistry and Molecular Biology
Dissertation Advisor
Chair of Committee

Lasse Jensen
Professor of Chemistry

Christine Keating
Professor of Chemistry

Ralph H. Colby
Professor of Materials Science and Engineering & Chemical Engineering

Philip Bevilacqua
Distinguished Professor of Chemistry & Biochemistry and Molecular Biology
Head of the Department of Chemistry

ABSTRACT

Previous studies of the liquid phase have revealed intermolecular interactions between ions and surfaces in aqueous solution. Such work points to the importance of water structure in the first hydration shell around ions and their specific binding sites. An interaction often exists between two ions, ions and dipoles or ions and hydrophobic groups. The resulting 'ion-receptor' complexes can form either direct contacts or water-mediated structures. Contact pairs exist when both the ion and the binding site dehydrate and directly interact. Water-mediate pairs exist between species that share hydration water. While contact pairs have been shown previously to be important for numerous processes, water-mediated binding events have received less attention. Herein, ion-ion and ion-dipole interactions are studied in aqueous solutions. These investigations revealed consequences of water-mediated pairing in two separate phenomena. In a first set of studies, the impact of water-mediated ion pairs on the conductivity of salt solutions was investigated. Hydroxide has been shown previously to undergo transport by a phenomenon known as the Grotthuss mechanism. This results in fast diffusion of OH^- compared to simple ions like Na^+ or Cl^- due to proton transfer between water and OH^-. Here, water-mediated ion pairs modulated the diffusion constant of alkali hydroxide salts. In a second set of studies, Onsager's reaction field theory was tested in salt solutions. Water-mediated interactions between polar organic molecules and metal halide salts were of central importance to this study. Focus was given to molecules containing either carbonyl or nitrile bonds. The C=O oxygen atom formed water-separated pairs with well-hydrated metal cations like Mg^{2+}, while the C≡N nitrogen did so with poorly-hydrated ones like Cs^+. Moreover, I^- formed these pairs with the positive terminus of either dipole better than Cl^-. Such interactions resulted in the establishment of a local electric field. These findings revealed that Onsager's model breaks down in electrolytes due to water-mediated ion-dipole interactions.

TABLE OF CONTENTS

LIST OF FIGURES

LIST OF TABLES

ACKNOWLEDGEMENTS

First and foremost, I thank God for care and guidance. I would be beyond lost without divine help and love. I have been blessed with a family that loves me including Gina, my son Aniello, my parents Alane and Mike and extended family members as well. Gina and Aniello, my love for you is eternal. My father's work ethic and drive in the face of great adversity were instilled in me from a young age. My late cousin, Haresh, inspired my interest in mathematics. He will be forever loved and remembered. My uncle, David, has been an inspiration to me as well.

I am incredibly grateful for my advisor Dr. Paul Cremer. Paul recognized my passion for physical chemistry from the moment we met, and he has taken every opportunity to cultivate me. His impact on me cannot be adequately described with words on paper. I am thankful for holistic guidance and care from Dr. Bratoljub Milosavljevic. I also would like to thank my committee members Dr. Lasse Jensen, Dr. Christine Keating and Dr. Ralph Colby, all of whom have engaged with me in useful discussions along this journey. I would not be where I am today without Dr. Thomas Mallouk who has served as a scientific, professional and personal advisor throughout my time at Penn State. My work would not have been possible without Dr. Tinglu Yang who has served as a professional, technical and personal mentor. I also would like to thank Dr. Steven Corcelli from Notre Dame who provided valuable insights throughout my time in graduate school.

My work at Penn State has been enriched by experiences with my colleagues. Dr. William Noid taught me so much during our time together. I am thankful to have met and worked with Ryan Myers, Stephen Koehler and Dr. Chris Li. Finally, I would like to thank Dr. TJ Mullen, Dr. Tao Ye, Dr. Michael Lufaso, Dr. Rick Troendle, Dr. Jose Jimenez, Dr. Mark Sito, Mr. Mills, Mr. Cargill, Mr. Orndorff, Todd and Ali. TJ, my career would not have evolved without influences from both you and your brother, Patrick. My work was funded by the National Science Foundation (CHE-1709735 & CHE-2004050), but does not necessarily reflect the view of this agency.

Chapter 1

AN INTRODUCTION TO SOLVENT-MEDIATED INTERMOLECULAR INTERACTIONS IN WATER

Association between dissolved solute molecules in water underpins numerous biological and technological processes. One such process is the hydrophobic effect in which oily molecules come together and reduce the number of broken water-water hydrogen bonds in the first hydration shell of the organic compound. This has a variety of important consequences ranging from protein folding to liquid-liquid phase separation. Recently, molecular-level details of hydrophobic hydration and aggregation have been revealed with vibrational hydration shell spectroscopy.[1,2] It is now recognized that hydration water drives oily compounds together through what has been termed as "water-mediated hydrophobic interactions" in aqueous solutions.[3] Namely, disordered hydration shells are liberated when aggregation occurs, and the resulting formation of water-water hydrogen bonds in the bulk solution drives the hydrophobic effect. By comparison, the role of hydration water in ion binding events has not been comprehensively explored. Such a set of studies promises to disentangle numerous phenomena including ion hydration, receptor-water interactions, inductive effects, hydrogen bonding and electrostatic forces as they relate to ion binding.

In order to embark upon a broad study of ion binding, one must first define a limited number of classifications into which rectors commonly found in nature may be sorted. These three classes are 1) hydrophobic moieties, 2) polar functional groups and 3) ionic binding sites. Hydrophobic receptors have been important in studying the origins of the Hofmeister effect where anions bind to aliphatic moieties in the peptide backbone.[4] Ion-ion interactions, of class three, have been extensively studied in attempts to understand ion pairing in simple salt solutions, and even in the case of charged protein side chains.[5-7] Ion-dipole interactions have received far less attention

than classes one and three, but yet are found in numerous systems ranging from those containing proteins to electrochemical interfaces.[4,8,9] This work sheds light on how hydration water mediates ion-ion and ion-dipole interactions in the bulk solution. Additionally, fundamental insight into hydration of cations and anions alone is provided. Importantly, several types of ion-receptor structures are shown to have thermodynamic and macroscopic consequences for numerous material properties. These include ion transport coefficients in alkaline fuel cells, the color emitted from dye molecules dissolved in solution and the surface tension at the air/water interface.[10,11]

This chapter highlights topics and tools that are of central importance for studies of intermolecular interactions in aqueous electrolytes. First, the Hofmeister effect is summarized to provide a foundation for understanding implications of findings throughout this work. Next, the law of matching water affinities provides a foundation for understanding the nature of water-mediated structures formed between ions and receptors. Finally, vibrational spectroscopic tools and methodologies for studying ion-ion and ion-dipole interactions at the molecular-level are described, in addition to a summary of the systems studied herein and key findings.

Specific Ion Effects in Aqueous Solution: The Hofmeister Effect

Ions influence and direct numerous processes that occur in water. These processes include protein folding, protein aggregation, micelle formation, macromolecular precipitation, phase separation, self-assembly, charge transfer at electrode surfaces, as well as enzyme function and catalysis.[4,10,12-17] Importantly, the influence of an ion on such properties depends on its chemical identity. This was first pointed out by Franz Hofmeister in 1888.[18,19] Hofmeister added numerous salts to aqueous solutions containing egg proteins. He systematically varied the identity of the cation and anion, as well as the salt concentration. Only small amounts of certain salts were needed to precipitate proteins. Other salts had to be added in large excess in order to observe salting-out.

By assessing the ease with which a cation (anion) led to precipitation while the anion (cation) identity was held constant, Hofmeister was able to rank both ions based on their precipitation power. Over the past 132 years since Hofmeister's seminal work, his rankings have been shown to underpin numerous processes that occur in water aside from protein solubility. As such, the Hofmeister effect, also called a specific ion effect, is rather general. Common rankings for specific ion effects are given by the following series of anions and cations[4]:

$$CO_3^{2-} > SO_4^{2-} > S_2O_3^{2-} > H_2PO_4^- > F^- > Cl^- > Br^- \approx NO_3^- > I^- > ClO_4^- > SCN^-$$

$$N(CH_3)_4^+ > NH_4^+ > Cs^+ > Rb^+ > K^+ > Na^+ > Li^+ > Ca^{2+} > Mg^{2+}$$

Ions on the left side of these series lead to protein precipitation upon adding only small amounts to solution. Conversely, ions found on the right have to be added in excess for precipitation to occur.

Before circa 2000 researchers believed that ion specificity was a result of differing impacts form ions on bulk water structure.[20-22] Specifically, it was thought that ions which readily salt-out biomacromolecules do so by enhancing the strength of the hydrogen bonding network. These ions were called kosmotropes. On the contrary, ions that lie on the right-hand side were thought to weaken the bulk network and help organic compounds to remain in solution until large amounts of salt is added. These ions were called chaotropes. However, there are some problems with the idea of a bulk effect. First, the trend in charge density observed for anions is reversed in the case of cations. It is unclear why anions that are highly charged should rigidify the bulk network while highly charged cations should weaken it. Additionally, if a bulk effect were at play, the ordering of ions in the series would be universal and not depend on the system under investigation. However, different systems are known to give rise to different series. In fact, systems containing charged biomolecules are known to completely reverse the anionic Hofmeister series.[23,24] Moreover, on thermodynamic grounds, the molar compressibility of an electrolyte should reveal weather ions strengthen or weaken hydrogen bonds beyond the first hydration shell. Interestingly, pressure perturbation calorimetry measurements carried out as a function of salt identity are not able to

predict the Hofmeister series.[25] Finally, Bakker and coworkers have famously shown that neither cations or anions impact the stiffness of the hydrogen bonding network beyond the first hydration shell at the molecular-level *via* ultrafast and time-resolved infrared (IR) measurements of water's stretching mode.[26] In light of such issues and findings, researchers have concluded that the notion of a bulk effect should be replaced by a chemically-specific set of mechanistic rules governed by the local chemical environment in which an ion resides.

The current understanding of specific ion effects is related to ion hydration and direct binding events with organic molecules.[27,28] In order to comprehensively understand the typical Hofmeister series provided above, one has to first consider how ion-protein interactions should influence macromolecular solubility. If an ion binds, then one expects an excess of charge to be present on the macromolecular surface. This should result in charging and salting-in of the organic compound. As such, relatively large amounts of such an ion would be required to precipitate the protein. This is consistent with what Hofmeister observed for ions on the right-hand side of the series. On the other hand, if an ion does not bind then one expects aggregation of the organic compound to increase the free volume accessible to the ion. This is, ultimately, a depletion force and only a small amount of such an ion would be required to salt-out proteins. Indeed, this is what Hofmeister observed for ions on the left-hand side of the series. Importantly, if this idea of binding vs. depletion is correct then the ordering of the series could change in different systems. This is, indeed, observed for charged proteins like Lysozyme, which bears a net positive charge at physiological pH.[29]

In order to better understand how and why ions bind to proteins, it is important to consider the nature of the binding site and the hydration affinities of the ions. Our lab has taken advantage of model systems to understand ion-specific interactions at the protein backbone. One such model system is elastin-like polypeptides (ELPs).[30] An example of an ELP and the respective interactions of cations and anions with backbone moieties is schematically depicted below (Figure **1-1)**.[4]

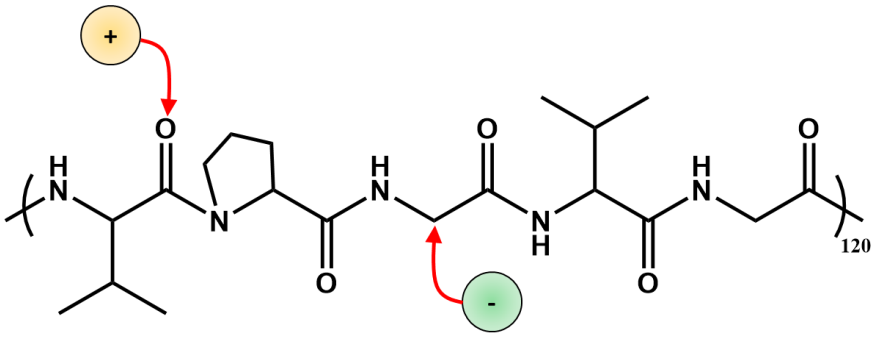

Figure **1-1**: Schematic of an ELP which is composed of hydrophobic residues. Specifically, this polymer consists of a pentameric unit repeated ~ 120 times. The amino acid residues which comprise the pentamer are valine, proline, glycine, valine and glycine in order from left to right. Direct interactions between the polymer and ions are shown with red arrows. A cation (yellow) is shown to bind with the amide oxygen atom. An anion (green) is shown to bind with an aliphatic group in the backbone.

The ELP depicted in Figure **1-1** is a model hydrophobic peptide which links together glycine, proline and valine residues. In the case of such hydrophobic polymers, highly charged and well-hydrated cations such as Mg^{2+}, Ca^{2+} and Li^{+} bind to the carbonyl dipoles.[31] Indeed, one may expect an ion-dipole interaction to occur best in the case of these cations as opposed to poorly-hydrated ones, like Cs^{+}, on electrostatic grounds. However, anions which lie on the right-hand side of the anionic Hofmeister series such as SCN^{-}, ClO_4^{-} and I^{-} are poorly-hydrated. As such, these ions bind to hydrophobic portions of the peptide including CH and CH_2 protons in the backbone.[4,30] Clearly, interactions between ions and dipoles is different than those between ions and hydrophobic groups. This demonstrates that both the nature of the binding site and hydration properties of the ion are fundamentally important in directing ion binding events.

The Law of Matching Water Affinities: Beyond Contact Ion Pairing

This work will build off of the idea that interactions between ions and receptors depend on the nature of the binding site and the hydration properties of the ion. As such, binding sites are

sorted into one of three groups based on their electrostatic properties as mentioned previously. Such classifications are depicted below (Figure **1-2**).

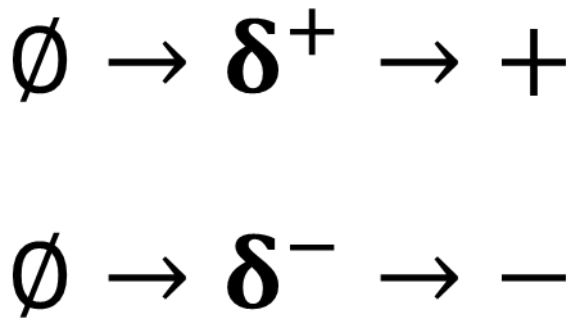

Figure **1-2**: Schematic of three different classifications for common receptors. The first class is composed of hydrophobic functional groups, which are electrically neutral and nonpolar. This is denoted by the null symbol (left most symbol on top and bottom). The second class consists of polar functional groups which do not bare a net charge, but are polarized and bare partial charges (center symbols on top and bottom). Finally, the binding site can bare either a formal positive charge (top right) or a formal negative charge (bottom right).

This work will primarily focus on ion-dipole and ion-ion interactions, but will also be concerned with ion-hydrophobe interactions as such a category captures the influence of salts on the surface tension at the air/water interface. Such an interface represents an ideal example of a hydrophobic surface.

An important question arises as to how ion-receptor interactions influence thermodynamic properties of a system which contains salt. In order to better understand the nature of this question, one can turn to the simple example of ion pairing in solutions of salt for which numerous types of structures are known to exist. These are sorted into two groups as shown in Figure **1-3**.

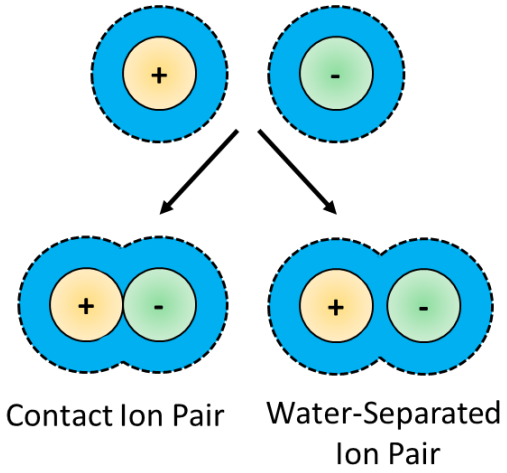

Figure **1-3**: Schematic of two types of ion pairing structures. Free ions (yellow and green; top) and their first hydration shells (blue regions) are shown to bind in an ion pair. The pairs can either be in direct contact (bottom left) or separated by water molecules (bottom right).

The two classes are broadly defined by considering both the ion and its first hydration shell. In a first case, both ions dehydrate and directly interact in a contact ion pair. In a second case, a layer of water molecules remains present between the ions in a water-separated ion pair.[32,33]

One may think that contact ion pairs modulate solution properties more readily than water-separated ones. Dehydration of the ions modulates their Gibbs free energy compared to when they are hydrated. As such, contact pair formation impacts the ions not only by way of ion-ion interactions, but also removes ion-water interactions. This is not necessarily true for water-separated pairs. Such pairs represent correlations between the ions which do not completely remove portions of the hydration shell. As such, contact ion pairs may nominally be expected to have greater effects. However, this work will show that water-separated pairs also impact macroscopic properties in electrolytes. Moreover, this work demonstrates that these two classifications of ion-ion interactions can describe the nature of interactions between ions and organic dipoles as well.

It is important to understand why some ion-ion interactions adopt contact pair motifs while others adopt water-separated ones. This has been explained previously by a set of guidelines known

as the Law of Matching Water Affinities (LMWA). This rule can be best used to predict formation of contact ion pairs when simple alkali halide salts are dissolved in water.[34,35] The LMWA predicts that contact ion pairs will form between a cation and anion if their affinities for water are similar. For example, this rule predicts that LiF and CsI form contact ion pairs. However, pairs which form in solutions of LiI or CsF should adopt water-separated motifs. The reasoning behind this rule stems from the competitive nature of ion-water and ion-ion interactions. Both Li^+ and F^- are highly charged and well-hydrated. One might suspect that well-hydrated ions should form water-separated pairs. However, high charge density allows both ions to overcome their free energies of hydration and form contact ion pairs due to strong electrostatic attraction. On the other hand, Cs^+ and I^- are rather large and their charge densities are small. As such, these ions are poorly-hydrated and readily overcome their dehydration penalties to form contact pairs. In the case of LiI, Li^+ cannot overcome its dehydration penalty because I^- does not provide a sufficiently strong electrostatic force, especially compared to F^-. As such, water-separated pairs are expected to be more abundant in solutions of LiI and CsF, but contact pairs are expected to be more abundant in LiF and CsI.

Kim Collins proposed to expand the LMWA beyond ion pairing in simple alkali halide systems to those of relevance for the Hofmeister effect.[36] For example, Collins argued that the imbalance of Na^+ and K^+ cations across the cell membrane is made possible by contact ion pair formation between carboxylate groups and Na^+ cations.[36] Moreover, oxyanions represent important biological receptors which behave differently than halide anions. For example, the negative charge on polyatomic phosphate or carboxylate groups is spread over multiple oxygen atoms by resonance. One may expect to find deviations from the LMWA when the receptor is more complicated than simple halide anions. An important question arises as to whether ion-dipole interactions are also governed by relative differences in ion hydration. The topics of ion hydration, ion pairing, dipole hydration and ion-dipole interactions will be reoccurring themes throughout this work.

Measuring Ion Binding Events at the Molecular-Level with Vibrational Spectroscopy

This work combines thermodynamic measurements with spectroscopic experiments in an effort to illuminate connections between ion-receptor structures and macroscopic properties. Vibrational spectroscopy will be used to provide insights into the structure of ion-receptor complexes at the molecular-level by helping to disentangle signatures of contact pairs from water-separated ones. Two types of vibrational resonances are used in all of the chemical systems studied here. Namely, one can monitor vibrations of the solute, and those of hydration shell water molecules. These vibrations can be monitored before and after ion binding in order to obtain structural information about the resulting complex. This methodology is schematically depicted below in Figure **1-4**.

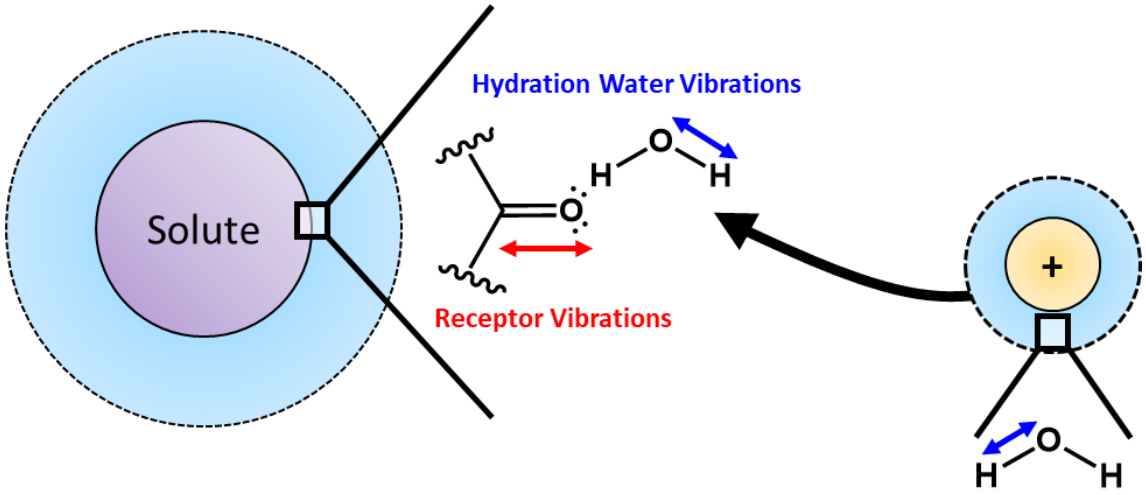

Figure **1-4**: Schematic of a carbonyl moiety on the surface of a macromolecule (purple) exposed to hydration shell water (blue regions). The back squares and extending lines indicate visual enlargement. Stretching modes of both the solute and solvent can be measured with vibrational spectroscopy in order to explore ion binding. The carbonyl represents a binding site in this schematic. This dipole could, in principal, be replaced with a charged moisty or a hydrophobic one. One can imagine measuring the O-H stretching mode of ion hydration water as well. The black arrow pointing from the ion to the binding site indicates that these vibrational modes can be monitored upon ion binding.

This schematic emphasizes the generality of this approach. The solute could be small or macromolecular in nature. The binding site could be charged, polar or hydrophobic. Both cation and anion binding events can be studied in this way. If one measures vibrations at the binding site and in the hydration shell then molecular-level structures may be deduced rather generally.

This work employs both infrared (IR) and Raman vibrational spectroscopies to explore intermolecular interactions in the bulk solution. These techniques probe the transition from the ground state to the first excited state of an anharmonic vibrational energy well. This is depicted in Figure **1-5**.

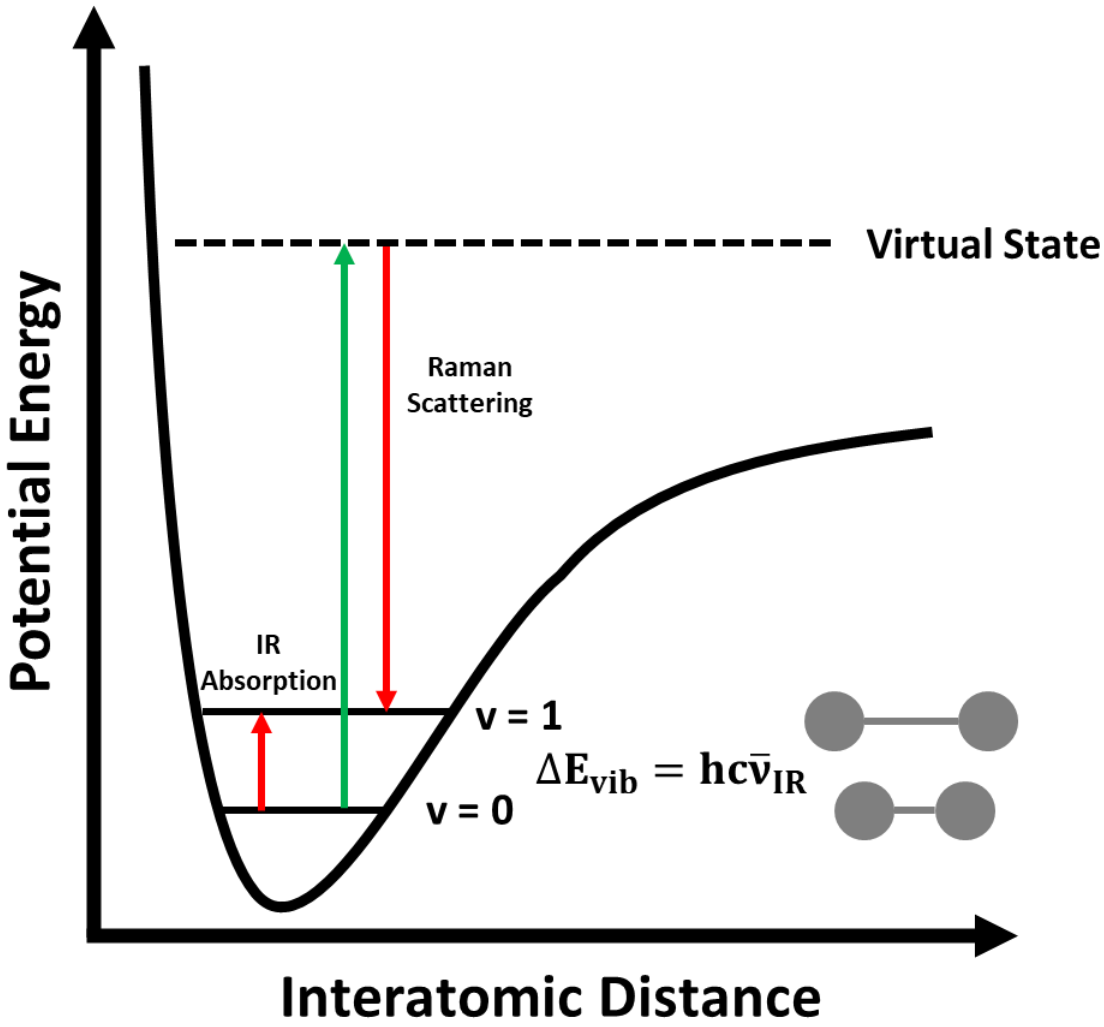

Figure **1-5**: Schematic of the vibrational energy landscape for the stretching mode of a chemical bond. IR spectroscopy probes absorption from the ground (v = 0) to the first excited (v = 1) vibrational energy levels. Raman spectroscopy probes light scattering by bond vibrations. The difference in energy between v = 0 and v = 1 levels (ΔE_{vib}) can be related to the frequency of infrared light ($\bar{\nu}_{IR}$; in cm^{-1}) by the well-known Plank-Einstein postulate $\Delta E = E_{photon}$. As usual, $\bar{\nu}_{IR} = (\bar{\nu}_{Excitation} - \bar{\nu}_{Raman\ Scatter}) \equiv \bar{\nu}_{Raman\ Shift}$. The grey cartoon depicts bond anharmonicity by showing a greater dipole moment in the excited state compared with the ground state.

Vibrational Hydration Shell Spectroscopy of Aqueous Electrolytes

This work explores hydration shells around ions in the bulk solution with IR and Raman spectroscopies. Specifically, spectra of pure water and a salt solution are collected. The difference between these two spectra should provide information on two types of vibrational modes. First, solute vibrations should be present in the difference spectrum. Second, O-H stretching and H-O-H bending modes of water in the difference spectrum should arise from water molecules which are perturbed by the solute. Such perturbations are assumed to occur in the first hydration shell. Moreover, the anion of a salt is assumed to perturb its hydration waters far more than the cation due to an asymmetry between cation-water and anion-water interactions.[37] This asymmetry is related to a small amount of charge transfer that occurs from anions, such as halides like Cl^- or I^-, into antibonding orbitals on water. Importantly, transfer of charge from water lone pairs into orbitals on cations, like Na^+, is negligible. This is depicted below (Figure **1-6)**.

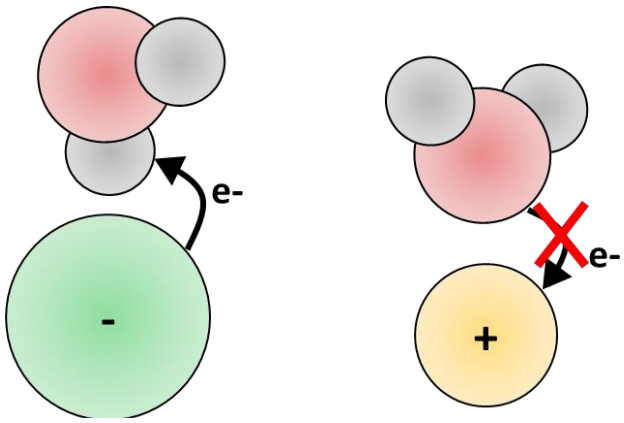

Figure **1-6**: Schematic highlighting differences between anion-water (left) and cation-water (right) interactions. Charge transfer occurs from an anion like Cl^- into the σ* antibonding orbital of the water O-H bond. Such charge transfer is not expected to occur from water lone pairs into the unfilled s-orbital of a cation like Na^+ as indicated by a red X.

While both ions definitively structure water around them, which can be measured with neutron scattering experiments, vibrational modes of water are not expected to display symmetry due to charge transfer.[22] This means that vibrational difference spectroscopy is expected to

predominantly report on the signatures of anion hydration when the solute is a simple salt. This is a manifestation of the charge transfer to solvent transition between anions and water which is known to be present in electronic spectra.[38-42] Moreover, transition metal cations may be an exception to this idea due to unfilled d-orbitals. A comparison between the so-called Hofmeister metal cations and first-row transition metal cations of the Irving-Williams series will be provided in chapter 5.

Our lab uses a rather sophisticated form of vibrational difference spectroscopy known as Multivariant Curve Resolution (MCR).[43,44] Software was provided to us by Dor Ben-Amotz from the Department of Chemistry at Purdue University (West Lafayette, IN). Specifically, we use a version of MCR known as Self-Modeling Curve Resolution (SMCR), which shall be called 'MCR' throughout this work. The algorithm performs a component analysis where two spectra are provided as inputs and two are returned as outputs. MCR spectra are guaranteed to have positive intensities at every frequency in the analyzed spectrum. The two input spectra are pure water and a mixture solution (M). The first spectrum returned by the algorithm is one which has the same line shape as pure water, and describes the bulk solvent component (S_B) in M. The second output captures everything which is different between pure water and M. This contains information about the solute modes and the hydration shell. As such, this is known as the solute-correlated (SC) spectrum (S_{SC}). Once S_B and S_{SC} spectra have been determined, the intensities of each are scaled by their species concentration (C_B or C_{CS}) to provide two components, C_B*S_B and C_{SC}*S_{SC}, which add together to describe M as shown in Equation **1-1**.

$$M = C_B * S_B + C_{SC} * S_{SC} \qquad \text{Equation } \mathbf{1\text{-}1}$$

In this approach, S_B and S_{SC} are analogous to orthonormal basis vectors. These unit vectors can be thought of as describing the spectral line shape of bulk and solute-affected components. Mathematically, there are an infinite number of solutions for C_{SC}*S_{SC}. In this work, the minimum area spectrum is used, and all hydration shell spectra describe only the most perturbed features of

the hydration shell. In principal, C_{SC}*S_{SC} may not correspond to a complete first shell in the O-H stretch region, but rather to only the most perturbed water molecules. While MCR is a matrix approach, C_{SC}*S_{SC} simply represents the minimum area non-negative difference between pure water and M. One could manually obtain C_{SC}*S_{SC} by scaling the pure water spectrum until every intensity value in the difference spectrum is positive, and the area under the curve is minimized. This is extremely cumbersome and would not provide results in a systematic way. As such, we take advantage of the MCR algorithm throughout this work.

In an effort to clearly demonstrate the advantage of our MCR approach, an example of a NaOH solution is provided in Figure **1-7**. This salt will be of central importance in Chapter 2.

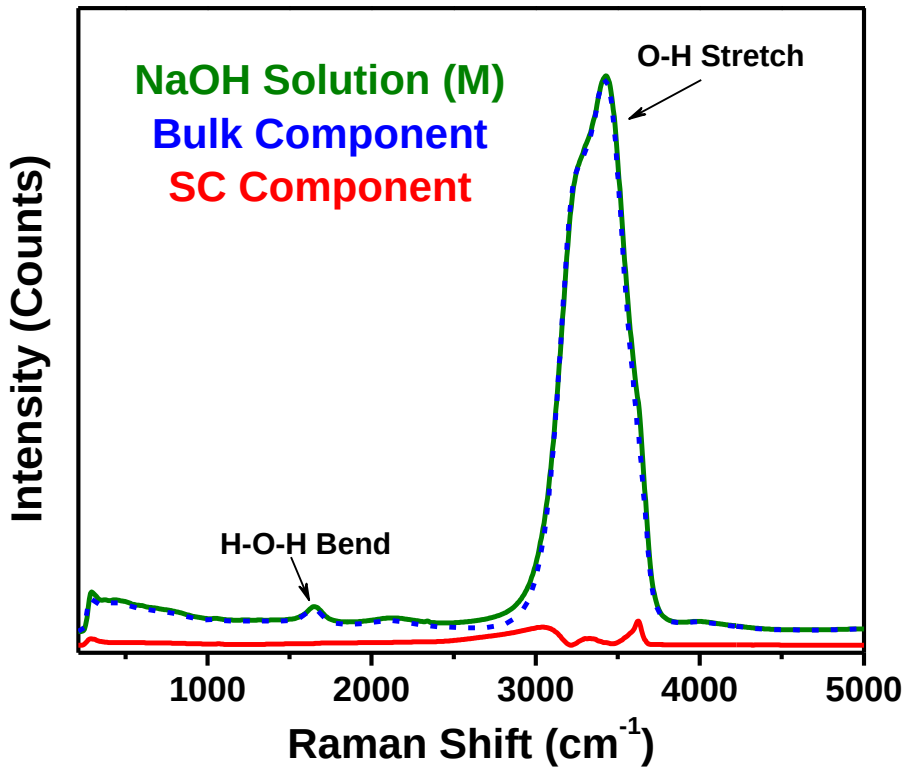

Figure **1-7**: Raman-MCR data of a 1 M NaOH solution. The M spectrum is shown as a green curve. The component of M given by C_B*S_B is shown as a dotted blue curve. The component given by C_{SC}*S_{SC} is shown in red.

The small features in the SC spectrum may have negative intensities in a typical and direct difference spectrum, if unconstrained. Clearly, constraining the difference to have positive intensities can provide a way to address changes in hydration shell structure systematically. This is demonstrated by the remarkably clear SC spectrum (red) presented in Figure **1-7**, which is intrinsically buried beneath large bulk intensities in the O-H stretching region.

Systems and Key Findings

In a first set of studies, we explore ion paring in aqueous hydroxide solutions as a function of the identity of the counter cation. Specifically, chapter 2 seeks to test the role of counterions on the Grotthuss mechanism. We find evidence that diffusion of OH^- is much slower in solutions of LiOH than in those containing either NaOH or KOH. These transport properties are investigated at the molecular-level with a combination of *ab inito* molecular dynamics simulations and vibrational-MCR spectroscopy. We find evidence for formation of water-separated ion pairs in solutions containing LiOH at millimolar concentrations. By contrast, ion pairing in solutions containing NaOH is not observed until much higher concentrations. Moreover, water-separated motifs in solutions of LiOH promote proton sharing and delocalization within hydroxide's first hydration shell. This indicates that proton transfer properties can be decoupled from the overall diffusion mechanism as a result of structural properties of water-separated ion pairs.

In a second set of studies, we test Onsager's reaction field theory in solutions containing salt. This model has long been used to calibrate Stark shifts in vibrational and optical probes employed to study catalysis. Such efforts have previously demonstrated that calibration of the probe may be accomplished by studying solvatochromism across a large series of organic solvents and water. In chapter 3, we find that the addition of salt gives rise to 'anti-Onsager' solvatochromism

in solutions of carbonyl, nitrile and PRODAN probes. Moreover, we find that this arises from water-separated ion-dipole interactions that follow trends which are reminiscent of the LMWA. Specifically, water-separated pairs form between carbonyls and well-hydrated cations like Mg^{2+} or Li^{+} whereas nitriles form water-separated pairs with poorly hydrated cations like Cs^{+}. Importantly, the anion follows a direct Hofmeister series for all vibrational probes. Namely, I^{-} salts Stark shift these probes more than those containing Cl^{-}. We conclude the local electric field around a dipole arises from a double-ion bound motif. Importantly, the formation of such structures is governed by water-separated binding as opposed to intrinsic properties of ions dissolved in the bulk, such as their charge density.

In chapter 4, we explore impacts of cation-carbonyl interactions on the electronic structure of the dipole. Specifically, we synthesize both *N*-methylacetamide (NMA) and ^{15}*N*-NMA and measure the amide I vibration upon the addition of either Ca^{2+} or hydrochloric acid. We find evidence that tautomer formation in solutions containing acid gives rise to a $C{=}N^{+}$ resonance which can be clearly distinguished from dehydration of the carbonyl by interaction with a metal cation. As such, cation binding only impacts the electronic structure of the amide by disrupting charge transfer through the hydrogen bond between the carbonyl and water.

Chapter 5 explores the mechanisms of metal cation hydration in bulk water. Specifically, the Hofmeister series contains simple metal cations; however, first-row transition metal cations of the Irving-Williams series are often studied in very different contexts than those of the Hofmeister series. For example, the Hofmeister series is often studied in solutions of proteins, polymers and small organic molecules. However, the Irving-Williams series is often used to rationalize trends in the formation constants of coordination compounds as a function of the metal center. Hofmeister cations should only be able to interact with lone pairs on hydration water by electrostatic forces, while transition metals should be able to participate in charge transfer. As such, the Hofmeister and Irving-Williams series should be governed by fundamentally different means of cation dehydration,

which must be overcome for contact pairing to occur. Interestingly, some studies have attempted to make direct comparisons between Hofmeister and transition metal cations. This may not be entirely fair. An important question arises as to whether Zn^{2+} is hydrated more similarly to Hofmeister cations due to its d^{10} electronic structure. We find evidence for charge transfer in the hydration shell of Zn^{2+} which is absent from hydration shells of Hofmeister cations like Ca^{2+} and Mg^{2+}.

In a final set of studies, we explore the mechanism underlying controversial measurements of surface tension at the air/water interface. It has been known for some time that the surface tension increases over a wide range of salt concentrations upon titrating nearly any simple salt into water. However, at very low concentrations (< 1 mM) the surface tension decreases. Specifically, the surface tension decreases slightly from the value measured for pure water and reaches a minimum at ~ 1-2 mM salt before starting to rise. This is known as the Jones-Ray dip, and it has puzzled researchers for some time. This dip in the surface tension is nearly the same for all salts and occurs at absurdly low concentrations of salt. Such a decrease in surface tension implies that ions accumulate at the surface, while the following linear increase in surface tension suggests the ions are depleted. Some researchers have come to think that ions bind to the air/water interface at these low concentrations. However, the driving force for such binding events has remained unclear until recently. A reasonable explanation is that ions influence ultrafast (femtosecond) correlations between water dipoles over long distances as should readily occur within the Debye length. This is limited by the average distance between ions, and thus is most relevant at low concentrations. The impact of ions on water dipole correlations has been shown to give rise to large domains of collective hydration which results in an entropic penalty. This is a phenomenon in the bulk whereby ion-water interactions drive the ion to the air/water interface. Moreover, this explains differences in the Jones-Ray dip between H_2O and D_2O solvents. Yet, a very different mechanism for Jones-Ray has also been proposed. Namely, trace, nanomolar, contaminates such as surfactants have

charged head groups which can be screened by salt. Some researchers suggest that surfactant contaminates are ubiquitous to liquid solutions. They have proposed that formation of an organic monolayer occurs when very dilute salt is added. In chapter 6, we intentionally add nanomolar amounts of a surfactant to solution and, indeed, observe changes to the Jones-Ray dip. However, we clean the surface by aspirating it which reveals the Jones-ray dip cannot be eliminated by repeated stirring and surface cleaning cycles. This suggests that contamination is not the fundamental reason for the Jones-Ray dip.

All five of these studies explore the ways in which hydration drives ions and binding sites together. In one instance the binding site is another ion, in others it is an organic dipole dissolved in the bulk solution. In yet a last case, it is the air/water interface. Finally, we remove the binding site entirely to study hydration of cations alone, which is inevitably important for binding events.

Collaborations

This work has been aided by collaboration with four external research groups. Molecular dynamics simulations presented in chapter 2 and chapter 3 were conducted by Steven Corcelli's group in the Department of Chemistry and Biochemistry at the University of Notre Dame (Notre Dame, IN). Spectral calculations presented in chapter 2 were also carried out in Steven Corcelli's group. Two-dimensional infrared spectra presented in chapter 3 were measured in Arnaldo Serrano's research group in the Department of Chemistry and Biochemistry at the University of Notre Dame (Notre Dame, IN). Synthesis of NMA and ^{15}N-NMA presented in chapter 4 was carried out in Elizabeth Elacqua's group in the Department of Chemistry at The Pennsylvania State University (University Park, PA). Finally, surface tension measurements in chapter 6 were

independently conducted by both myself and Sylvie Roke's group at EPFL (Lausanne, Switzerland).

Chapter 2

COUNTER CATIONS AFFECT TRANSPORT IN AQUEOUS HYDROXIDE SOLUTIONS WITH ION SPECIFICITY

Diffusion coefficients for ions in aqueous solutions of HCl and NaOH have been reported to be larger than those in NaCl by factors of ~ 5.5 and ~ 3.1, respectively.[45-47] These enhancements result from the structural diffusion of H^+ and OH^- via a Grotthuss mechanism, as opposed to the hydrodynamic diffusion of alkali metal cations and halide anions.[48-51] The difference between the acid and base enhancement factors has been widely debated. Moreover, this subject has been explored by path integral and *ab initio* molecular dynamics (AIMD) simulations capable of describing proton transfer (PT) and proton sharing between oxygen nuclei.[52,53] The general consensus is that the hydration shell structure and proton jump dynamics differ for H^+ and OH^-.[49,53-55] Conversely, vibrational spectra have long suggested similarities between acids and bases, as both display broad continuous absorption bands.[56-62]

While significant differences in hydration structure exist between aqueous H^+ and OH^-, the similarities displayed in their vibrational spectra suggest that other factors may also help to account for the disparity in the diffusion constant data. For instance, the presence and identity of counterions can impact PT. In fact, experimental and theoretical studies of HCl solutions have shown that ion pairing pulls one proton in H_3O^+ towards Cl^- at concentrations greater than 2 M.[63-66] Moreover, structural diffusion of OH^- is thought to follow a mechanism in bulk solution where the lowest energy structures contain four water molecules donating hydrogen bonds to an OH^- oxygen.[49] Solvent fluctuations rupture one of these four hydrogen bonds, ultimately resulting in a tetrahedral configuration around the OH^- ion that is more favorable for PT.[49] The role of counter cations has not been closely considered in this dynamical hypercoordination mechanism.[49,67,68]

Herein, we explore the impact of alkali metal counter cations on OH^- hydration and mobility in bulk solution. Impedance measurements show that the diffusion coefficient is attenuated by more than 20% in the presence of Li^+ compared to Na^+ and K^+ at concentrations from 10 mM to 1 M. Complementary AIMD simulations show that Li^+ cations exhibit stronger electrostatic attraction to OH^- and form more ion pairs compared to Na^+. These findings agree with Raman multivariate curve resolution (MCR) spectroscopy that also suggests stronger ion pairing between Li^+ and OH^- compared with Na^+ or K^+. Moreover, infrared (IR) MCR spectra suggest subtly greater proton delocalization in the first hydration shell of hydroxide when Li^+ is the counterion compared to Na^+ or K^+. This is consistent with quantum mechanical calculations of the proton nuclei in the first hydration shell of hydroxide which report enhanced proton delocalization for water molecules in solvent-shared configurations between Li^+ and OH^-. Strikingly, our findings demonstrate that ion mobility is slower in LiOH solutions compared with NaOH or KOH, despite having more delocalized proton intensity in the corresponding IR spectrum. This is a surprising result because greater proton delocalization in the presence of Li^+ might be expected to increase solution conductivity and ion mobility. As such, cation-anion interactions would appear to be a more important factor in modulating ion mobility compared to a counterion's effect on proton transfer.

Counter Cations Impact Diffusion of OH^-

Ion mobility was measured using electrochemical impedance spectroscopy (EIS). EIS data was collected with two identical gold disc electrodes that were solidified in epoxy resin to fix the separation distance at about 2 mm. Our home-built electrode is shown here (Figure **2-1)**. This was built and operated in Tom Mallouk's group at Penn State (State College, PA).

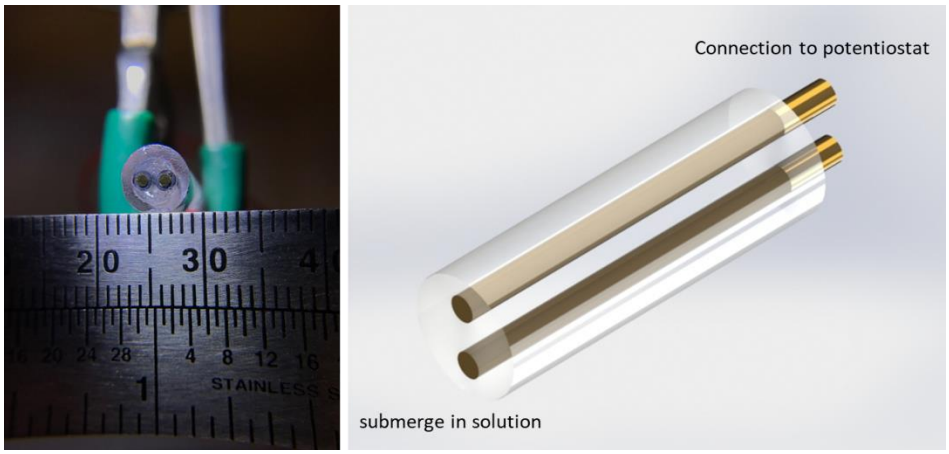

Figure **2-1**: Image and illustration of the gold disc electrode for the EIS measurements.

The gold surface was polished with sandpaper (from coarse to fine) and smoothed with 0.05 µm alumina particles to achieve a mirror finish. Alkali hydroxide solutions at different concentrations were prepared and the electrode was submerged as indicated in Figure **2-1**. EIS spectra were collected in a two-electrode/open circuit configuration having an AC frequency swept from 10 kHz and 1 Hz and a zero-to-peak amplitude of 20 mV on a Metrohm Autolab potentiostat (Model PGSTAT128N). The solution resistance was determined after fitting the Nyquist plot to an equivalent circuit. A sample of the Nyquist plot and the equivalent circuit are shown here (Figure **2-2)**.

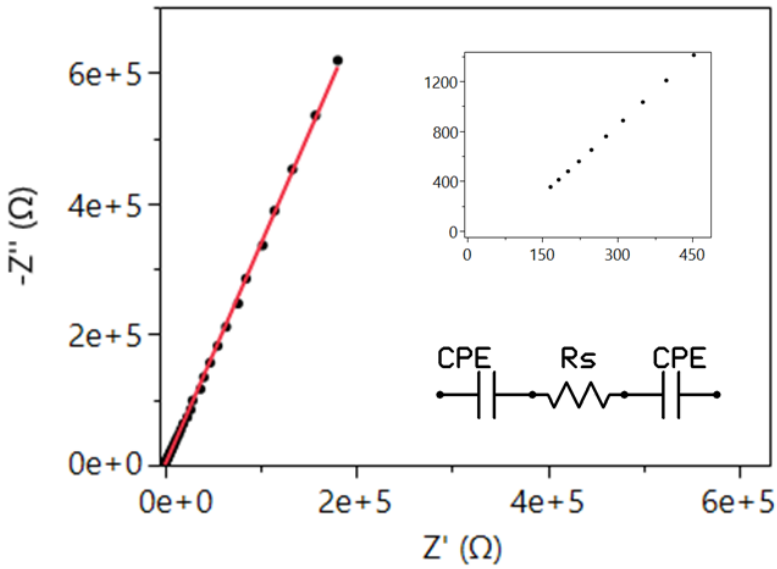

Figure **2-2**: Sample EIS spectrum for a hydroxide solution and an equivalent circuit. Z' and Z'' represent the real and imaginary portions of the impedance, respectively. The inset is a blow up of the low impedance regime. Solution resistance (Rs) was determined by fitting to the equivalent circuit. A constant phase element (CPE) was used instead of an ideal capacitor to model the microscopic roughness of the electrodes. The x-intercept is the purely real portion of the system's impedance. This is taken to be the solution's resistance and used to obtain molar conductivity values.

Standardized conductivity solutions (200, 100, 10 and 1.4 uS/cm) were used to calibrate the disc electrodes. The effective diffusion coefficients of the ions in solution were determined from molar conductivities according to the Nernst-Einstein relation given below (Equation **2-1)**.[69]

$$D_{eff} = \frac{RT\lambda_m^0}{F^2} \qquad \text{Equation } \mathbf{2\text{-}1}$$

D_{eff} is the effective diffusion coefficient, R is the gas constant, 8.314 J mol^{-1} K^{-1}, T is the absolute temperature, λ_m^0 is the equivalent molar solution conductivity obtained from the solution resistance given by the x-intercept of the Nyquist plot and the physical dimensions of the disc electrodes, and F is Faraday's constant (96,458 C mol^{-1}). The diffusion constant cannot always be quantified with Equation **2-1**. In this work, changes in D_{eff} are really changes just representing changes to λ_m^0.

Obtaining the solution resistance from EIS spectra requires isolating the real component of the complex impedance. This is obtained from a Nyquist plot which depicts the imaginary (y-axis) and real (x-axis) components of the impedance (Figure **2-2**). Our interpretation of the electrode-solution-electrode system is modeled ideally with capacitors representing the electric double layers at the disk surfaces, and the solution modeled by an ohmic resistor (Figure **2-2**). This is validated by the separation of charge in the double layer, and lack of impedance phase dependence in the bulk solution. The solution resistance is taken to be the purely real contribution to the complex impedance as the solution has no phase dependence and the capacitors have no resistance, ideally. The experimental data in Figure **2-2** are linearly extrapolated to the real axis (Figure **2-2** inset).

If the double layers behaved as ideal capacitors, the only contribution to the real component of the impedance at any point in the EIS spectra would be that attributed to the solution resistance. We simulated such an ideal configuration, and the resulting Nyquist plot is vertical a line. However, the double layers are not ideal capacitors, and this introduces a tilt to the Nyquist plot along the real axis (Figure **2-2**) which was verified via circuit simulations. As a result, our measured Nyquist plots, as exemplified in Figure **2-2**, are physically captured by a constant phase element-resistor-constant phase element model.

All samples were prepared immediately before use. All materials were used as received. NaOD in D_2O (40% wt. 99.5 atom % D) was acquired from Sigma-Aldrich (St. Louis, MO). NaOH (reagent grade, ≥ 98%, pellets (anhydrous)) and LiOH (powder, reagent grade, ≥ 98%) were acquired from Sigma-Aldrich (St. Louis, MO). KOH (min. 90.0%) was purchased from Spectrum Chemical (New Brunswick, NJ). All water (18 MΩ·cm) was produced from a Barnstead Nanopure Water System (Thermo Fisher). D_2O solvent (99.8 atom % D) and KCl (extra pure) were purchased from Acros Organics (West Chester, PA). All solutions were prepared by mass and diluted to the desired volume. The samples and solvent were purged with argon gas to eliminate CO_2. Although

this did not have any effect on the Raman or IR spectra shown below, it was necessary for EIS measurements which are discussed in this section.

In a first set of experiments, we have measured the electrochemical impedance of LiOH, NaOH, and KOH solutions using EIS. The results were used to determine the corresponding diffusion coefficients as a function of salt concentration. This data is shown below (Figure **2-3)**.

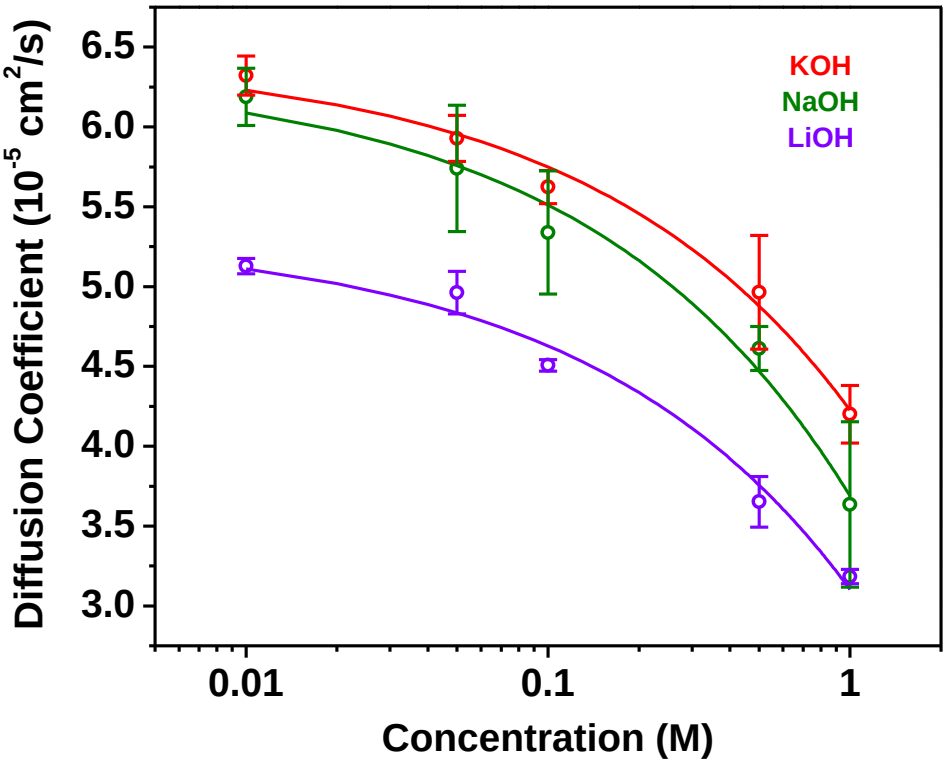

Figure **2-3**: Effective diffusion coefficients as a function of concentration obtained by EIS. Open circles are averages and the solid curves are fits to Onsager's model for the Kohlrausch effect. Error bars are from standard deviations of triplicate measurements.

Li^+ counter cations impede diffusion at all measured concentrations (Figure **2-3**, purple curve), which is in agreement with previous measurements.[70] Moreover, the hydroxide salts of all three cations display a decreasing trend in ion mobility that goes as the square root of the ionic strength. While these effective diffusion coefficients incorporate hydrodynamic contributions from

both the cation and hydroxide, the elevated diffusion constants compared to alkali halides are a hallmark of a structural diffusion process, i.e. a Grotthuss mechanism.

Concentration dependent diffusivity data was fit to Onsager's model for the Kohlrausch effect.[71] This follows a dependence as given below (Equation **2-2)**.

$$D(C) = D_0 + \alpha\sqrt{C} \qquad \text{Equation } \mathbf{2\text{-}2}$$

$D(C)$ is the effective diffusion coefficient of ions at a salt concentration C, D_0 is the effective diffusion coefficient of very dilute solutions and α is a constant. Diffusion coefficients in the above data (Figure **2-3**) are not for a specific cation or anion, but rather the effective values for both ions in solution. Ion diffusion coefficients are only additive in the absence ion-ion interactions.[71] The square root dependence on concentration is indicative of retarding forces between counterions, and thus ion additivity is not expected in our measurements. The constant α describes the shape of the fitted data, and these values agree very well for differing counter cations and are given below (Table **2-1)**.

Table **2-1**: Fit parameters to Onsager's model for the Kohlrausch effect. Experimental uncertainties are given in parentheses.

Species	$\boldsymbol{\alpha}$ **(10^{-5} cm^2 s^{-1} M$^{-1/2}$)**	$\boldsymbol{D_0}$ **(10^{-5} cm^2 s^{-1})**
LiOH	-2.2 (0.1)	5.3 (0.1)
NaOH	-2.7 (0.5)	6.3 (0.3)
KOH	-2.2 (0.1)	6.5 (0.1)

While α values are nearly independent of counter cation identity, differing D_0 values suggest that OH^- mobility is impacted by the counter cation in even very dilute solutions. This appears to occur well below the concentrations used in pioneering AIMD studies which was 0.5 M.

We attribute differences in effective diffusion coefficients (Figure **2-3**) to differences in structural diffusion of OH^- in the presence of various cations. However, differences in hydrodynamic diffusion of cations or OH^- can affect electrochemical data. First, hydrodynamic and structural mechanisms of diffusion are not necessarily additive for an OH^- anion moving independently from the counter cation. In fact, the directions of hydrodynamic and Grotthuss-like motions should be highly correlated. Regardless, literature values for cation diffusion coefficients in very dilute solutions (1.0, 1.3, and 2.0 $x10^{-5}$ cm^2/s for Li^+, Na^+ and K^+, respectively) do not explain our hydroxide data. The literature value for OH^- hydrodynamic diffusion (< $0.7x10^{-5}$ cm^2/s) cannot explain the difference between LiOH and NaOH or KOH curves.[55] In general, hydrodynamic diffusion coefficients are on the order of ~ 1-$2x10^{-5}$ cm^2/s. Our data are enhanced (> $5x10^{-5}$ cm^2/s) due to structural diffusion.

Investigating Ion Pairing with AIMD

The non-additive offset in mobility in the presence of Li^+ (Figure **2-3)** suggests that this ion may reduce the diffusion coefficient because of greater interactions with hydroxide. To explore this possibility further at the molecular level, our collaborators in the Corelli group (Notre Dame, IN) performed AIMD simulations with aqueous hydroxide solutions.

Simulations of 0.5 M OH^-, 1.0 M LiOH and 1.0 M NaOH were performed utilizing the CP2K open source Molecular Dynamics package on the XSEDE supercomputer resources.[72,73] Simulation boxes were built with Packmol, where the 0.5 M system contained one OH^- anion solvated by 110 H_2O molecules, and the 1.0 M systems contained 110 H_2O, 2 OH^-, and 2 counter cations.[74] A short geometry optimization of the atomic coordinates was performed before AIMD equilibration and production in the NVT ensemble, similar to a prior protocol used for studying the excess proton.[54,75] We implemented a form of AIMD called Born-Oppenheimer molecular

dynamics to propagate the nuclei with a timestep of 0.5 fs. CP2K uses the Quickstep method for force evaluations wherein the Gaussian and Plane Waves scheme is utilized.[76] We applied the Goedecker-Teter-Hutter (GTH) pseudopotentials for treatment of core electrons, the TZVP-GTH basis set, and the BLYP functional for exchange-correlation contributions with Grimme's D3 correction.[77-82] Initial simulations on all three systems were performed for 120 picoseconds (ps), where the first 20 ps were treated as equilibration. The LiOH and NaOH simulations were then extended an additional 100 ps to support ion pairing analyses (*vide infra*). Trajectories were collected in cubic boxes with periodic boundary conditions with a box length of 14.869 Å for 0.5M OH^- simulations, and 15.041 Å for both 1.0 M LiOH and NaOH simulations. We sampled each production trajectory at a frequency of 125 fs to obtain 800 independent snapshots to calculate hydration shell spectra for the 0.5 M OH^- simulation. These statistics were doubled for the 1.0 M systems as they each contain two, independent, OH^- anions.

We provide integrated ion number density values as shown below (Figure **2-4)**.

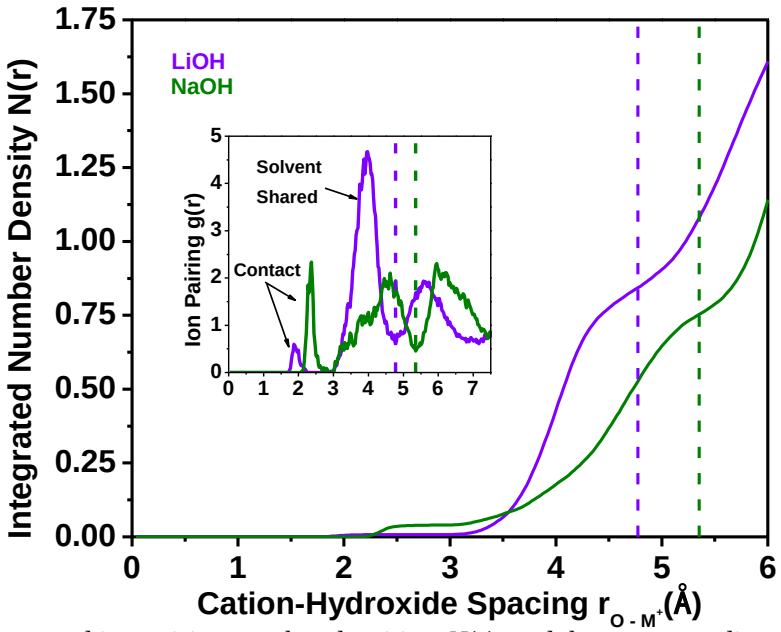

Figure **2-4**: Integrated ion pairing number densities, $N(r)$, and the corresponding radial distribution functions (inset), $g(r)$, for 1 M LiOH (purple) and 1 M NaOH (green) calculated from AIMD simulations. The *x*-axis denotes the spacing between the OH^- oxygen atoms and the metal counter cation, M^+. The dashed vertical lines depict the respective second minimum for each $g(r)$.

At a concentration of 1 M, there is greater ion pairing between Li^+ and OH^- compared to Na^+ and OH^-. The cations held on average 5.88 and 3.99 hydration waters, respectively, for Na^+ and Li^+ over each 100 ps trajectory. There were well-defined shells of counter cations around OH^- (Figure **2-4**, inset). The cutoff after the second shell is depicted by the dashed lines. Over this range of separation distances, cations form two distinct shells around OH^-. contact ion pairs, where the OH^- and counter cation directly interact, and solvent-shared ion pairs, where a water molecule resides in the first hydration shell of both ions.[83] Integrated number densities reveal that there are more ion pairs in LiOH solutions than in NaOH solutions over this spatial region. Furthermore, the $g(r)$ plot shows that Li^+ in solvent-shared pairs resides closer to OH^- than solvent-shared Na^+ pairs. The LiOH contact ion pair peak also resides closer to OH^- than the corresponding peak for NaOH due to Li^+ having a smaller radius, although there are very few contact pairs. Based on these

observations, it would appear that ion pairing and electrostatic attraction between Li^+ and OH^- should play a significant role in the measured diffusion differences in Figure **2-3.** It should be noted that the $g(r)$ data and integrated ion number densities were calculated from extended 200 picosecond (ps) simulations, while all subsequent analyses came from the first 100 ps trajectories.

Due to the short simulation timescales of AIMD, the convergence of the data was a question. The disparity in both the prevalence of ion pairing in NaOH solutions compared to LiOH as well as the contact ion pair lifetime was of concern for a 100 ps production trajectory. As such, we have extended both the simulations for 1.0 M LiOH and 1.0 M NaOH to 200 ps and recomputed the radial distribution functions for hydroxide oxygen to cation separations. These data are shown below (Figure **2-5)**.

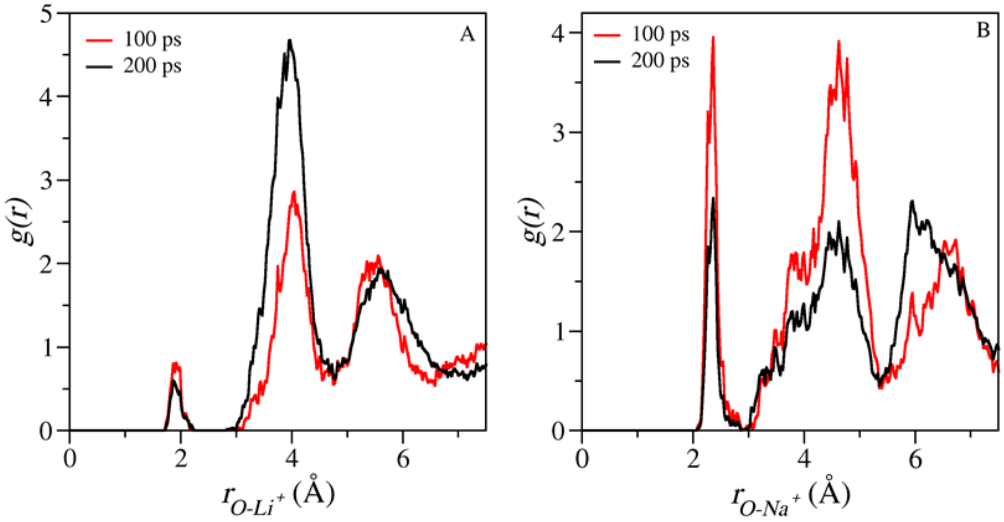

Figure **2-5**: Radial distribution functions of hydroxide oxygen to specific cations (A- LiOH, B-NaOH). RDF calculated from 100 ps simulations are shown in red and those from 200 ps simulations are in black.

In the case of LiOH, the prevalence of solvent-shared ion pairs increased with the addition of 200 ps while the contact ion pair peak stayed about the same. Moreover, the height of the solvent-shared pair population is extremely large. Since the height is related to the free energy it is extremely unlikely that the presence of solvent-shared ion pairs would not persist into even longer

simulations. Moreover, both contact and solvent-shared NaOH peaks changed by roughly the same amount upon increasing the simulation time. All together these findings suggest that the relative differences in ion pairing between LiOH and NaOH simulations is qualitatively robust.

Vibrational Hydration Shell Spectroscopy of OH^- in Water

Structural diffusion of both OH^- and H^+ ions in water is affected by quantum mechanical delocalization of proton nuclei.[48,49,51-53] The diffusion constant data presented in Figure **2-3** might lead one to wonder whether proton sharing between the oxygen nuclei should be diminished by Li^+. Moreover, vibrational spectra have long been known to show very broad vibrational bands for OH^- solutions, where the low frequency tails on the red side of the O-H stretch resonance have been attributed to shared/delocalized protons.[58] As such, Raman-MCR and attenuated total reflection (ATR) IR-MCR measurements are used in this section to better understand the impact of counter cations on OH^- and its hydration shell.

All unpolarized Raman spectra were collected on a home-built backscattering setup with an ArKr ion laser (514.5 nm line; Spectra Physics). The power at the sample stage was ~50 mW. Laser light was spectrally narrowed by a notch filter and sent though a half wave plate (Thor labs, Newton, NJ). It then passed through a polarized beam splitter (Thor Labs, Newton, NJ) and a second half wave plate. This setup allows for control of the incident power at the sample stage. Laser light was directed to the sample with a 514 nm notch filter (Thor Labs, Newton, NJ). A quartz cuvette was placed in a thermoelectrically controlled temperature jacket that was modified in house to accommodate a 10X microscope objective. The spectra were collected at 20.00 ± 0.01 °C. Stokes-shifted photons traveling along the backscattered path and passed through a notch filter before being focused onto an optical fiber with a lens. This fiber was connected to a spectrometer

(IsoPlane SCT 320; Princeton Instruments, Trenton, NJ) which used a grating (300 g/mm) to spread photons onto a cryogenically-cooled PyLoN 100BR CCD camera (Princeton Instruments) which binned the light every ~ 4 cm^{-1}. All spectra used for MCR analysis were collected on the same day at the exact same power with greater than 1,000:1 signal-to-noise. Subpixel drifts were corrected for by using the Rayleigh signal which leaked through the notch filter.

All experimental Fourier Transform (FT) IR spectra were collected on a Bruker spectrometer (VERTEX 70; Thermo Fisher Scientific, Billerica, MA) with an MVP Pro (Harrick Scientific Products Inc., Pleasantville, NY) attenuated total internal reflection (ATR) stage located in the Millennium Science Complex's Materials Characterization Laboratory at The Pennsylvania State University's University Park Campus. Data were collected at ambient temperature in an environmentally controlled room. All spectra were normalized to the bare ATR window (made of diamond) signal with a spectral resolution of ~5 cm^{-1} and an optical mirror velocity of 2.6 cm/s with an incident beam angle of 45°. A narrow band mercury-cadmium-telluride detector was cooled with liquid nitrogen before use. The ATR window on this instrument was made of diamond and allowed for exploration of concentrated basic solutions.

All MCR data was produced with software provided by Dor Ben-Amotz and operated in Igor Pro® v. 6.37. Following decomposition of the input spectra, all solute-correlated (SC) spectra had a constant background subtracted. All OH^- and Cl^- solutions were referenced to H_2O solvent, and all OD^- solutions were referenced to D_2O solvent. Cation- and isotope-specific SC spectra were left unnormalized because all species were present at 1 M. Concentration dependent spectra could be left unnormalized, but are also normalized by their concentrations where indicated.

Raman and IR data were first collected as a function of counter cation in an effort to better understand ion pairing in alkali hydroxide solutions and impacts of the cation on proton delocalization. This data is shown in Figure **2-6**.

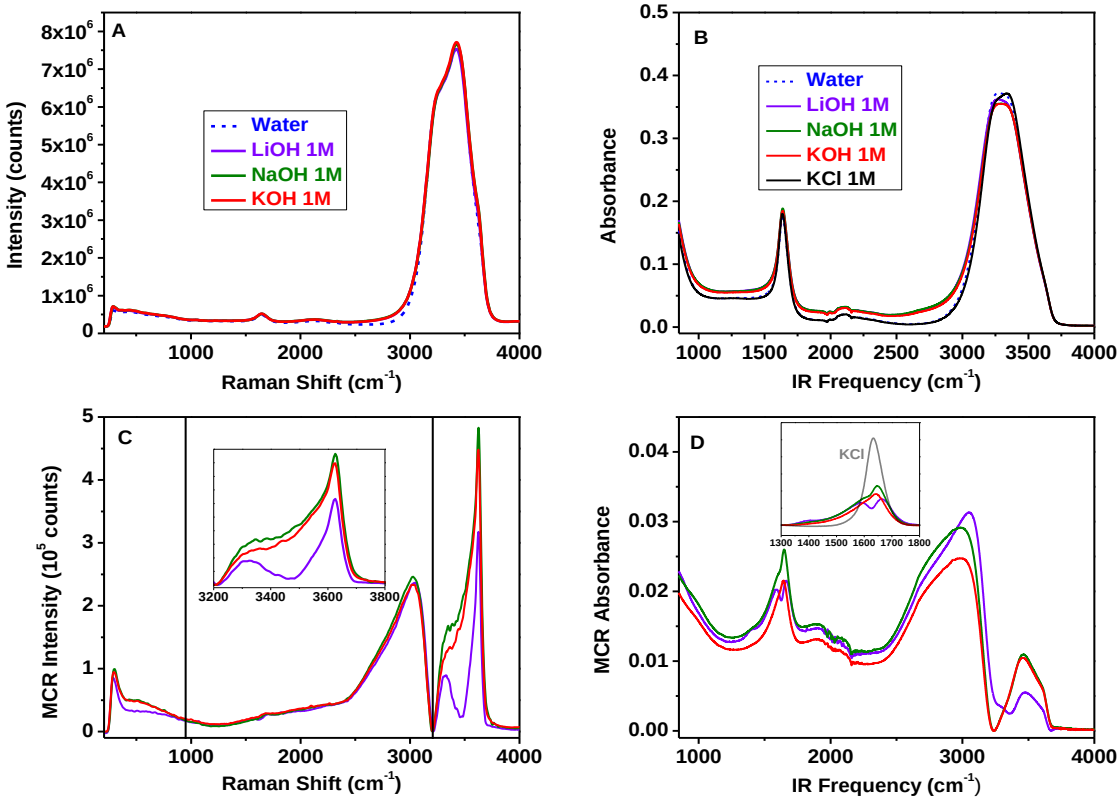

Figure **2-6**: (A) Raman spectra of 1 M hydroxide solutions and neat water. (B) ATR-FTIR spectra of 1 M hydroxide solutions, neat water, and 1 M KCl. (C) Raman-MCR spectra of 1 M hydroxide solutions. The inset shows the frequency region corresponding to the localized proton O-H stretch vibrations. (D) IR-MCR spectra of 1 M hydroxide solutions. The inset shows the line shapes of the water bending mode as a function of counter cation for the hydroxide salts as well as for a 1 M KCl solution (grey).

The bulk Raman and IR spectra do not reveal an obvious counter cation dependence (Figure **2-6** A & Figure **2-6** B), in agreement with previous findings.[84,85] The Raman data show a modest red tail just below 3000 cm^{-1} for the O-H stretch mode in all three OH^- solutions (Figure **2-6** A). This tail spans a significantly greater frequency range in the IR spectra (Figure **2-6** B), reaching as low as ~950 cm^{-1}. By contrast, KCl solutions have intensities that almost exactly match pure H_2O across this frequency range (Figure **2-6** B). Therefore, the broad continuum found in hydroxide solutions can be attributed to the hydration sphere around OH^- anions.

An MCR algorithm (Figure **2-6** C & Figure **2-6** D) was applied to these spectra to remove the background bulk water response. The resulting hydration shell spectra represent the minimum non-negative area difference between the hydroxide mixture spectra and pure water. When considering salt solutions, the MCR hydration shell spectra predominantly arise from anion hydration.[37,86,87] The dominance of anions over cations in these spectra should result from the different nature of water-cation and water-anion interactions. Namely, a small amount of electron density from the anions is donated into the antibonding orbitals of the surrounding hydration water molecules.[88,89] This leads to a significant perturbation of water vibrational modes. On the other hand, cations can only interact electrostatically with the oxygen atoms of their hydrating waters and thus have a smaller effect on the vibrational modes.[90]

The Raman-MCR spectra show a drop in intensity to near baseline around 3205 cm^{-1} for all three cations (Figure **2-6** C). This frequency provides a remarkably clear demarcation line between the intensity for localized protons at higher frequencies, and the more delocalized protons in the hydration shell of hydroxide between ~ 950 and 3205 cm^{-1}. Such an assignment for this region will be rigorously discussed below. By contrast with the Raman data, only the KOH and NaOH IR-MCR spectra display a similar minimum in this range, which is blue-shifted to near 3238 cm^{-1} (Figure **2-6** D). The LiOH IR-MCR spectrum, however, has significant intensity around this frequency. Moreover, the LiOH IR-MCR data reveals greater proton delocalization in the hydroxide hydration shell as indicated by somewhat enhanced intensity below 3238 cm^{-1} as compared to Na^+ and K^+. This enhancement corresponds to protons in water O-H bonds that donate hydrogen bonds to OH^-, as will be described below. Nevertheless, the Raman-MCR spectrum for LiOH solutions display essentially the same intensity as found for NaOH and KOH for the delocalized proton signature (intensity between the vertical black lines in Figure **2-6** C), but substantially less intensity above 3205 cm^{-1} and below 950 cm^{-1}.

The reduced intensity in the high frequency region of the LiOH Raman-MCR spectra compared to NaOH and KOH is related to the identity of the counterion and the concentration of solvent-shared ion pairs. First and foremost, this region of the spectrum results from water O-H bonds which point away from the hydroxide. The simplest interpretation of the Raman-MCR data would be that contact ion pairs between Li^+ and OH^- lead to fewer first hydration shell water molecules around the hydroxide ion. However, the integrated ion pairing number densities from AIMD simulations speak against this idea (Figure **2-4**) and show that there is only a minimal number of contact-ion pairs in either LiOH or NaOH at 1 M concentration. Moreover, the intensity in both high frequency and low frequency regions should be attenuated by contact ion pairing. Li^+ is well hydrated and small which allows this cation to sit closer to and interact more strongly with a bridging water in solvent-shared ion pairs as revealed in AIMD simulations. In light of these results, Corcelli's group also performed quantum chemical calculations (MP2/aug-cc-pVTZ) of the Raman cross section of optimized H_2O --- Li^+ and H_2O --- Na^+ complexes in the gas-phase were conducted and showed that Li^+ diminishes the water symmetric stretch Raman intensity by ~ 50% relative to Na^+. The substantially higher concentration of more closely spaced solvent-shared ion pairs in LiOH, along with the greater attenuation of Raman intensities by Li^+ compared to Na^+, support the idea that the dip in the MCR-Raman spectra at ~3470 cm^{-1} (inset of Figure **2-6** C) is a result of solvent-shared ion pairing which arises from impacts of Li^+ on the oscillator strength of O-H bonds which point away from hydroxide. Na^+ can also give rise to a comparable dip at this frequency, when 6 M NaOH is in solution, as will be shown below. Of course, in this case, the salt saturation limit has been reached and the fraction of Na^+ solvent-shared ion pairs is quite substantial.

Additional Raman-MCR data was taken with 0.5 M LiOH and a similar intensity attenuation was found in the low and high frequency regions as for 1.0 M LiOH. This is shown here (Figure **2-7)**.

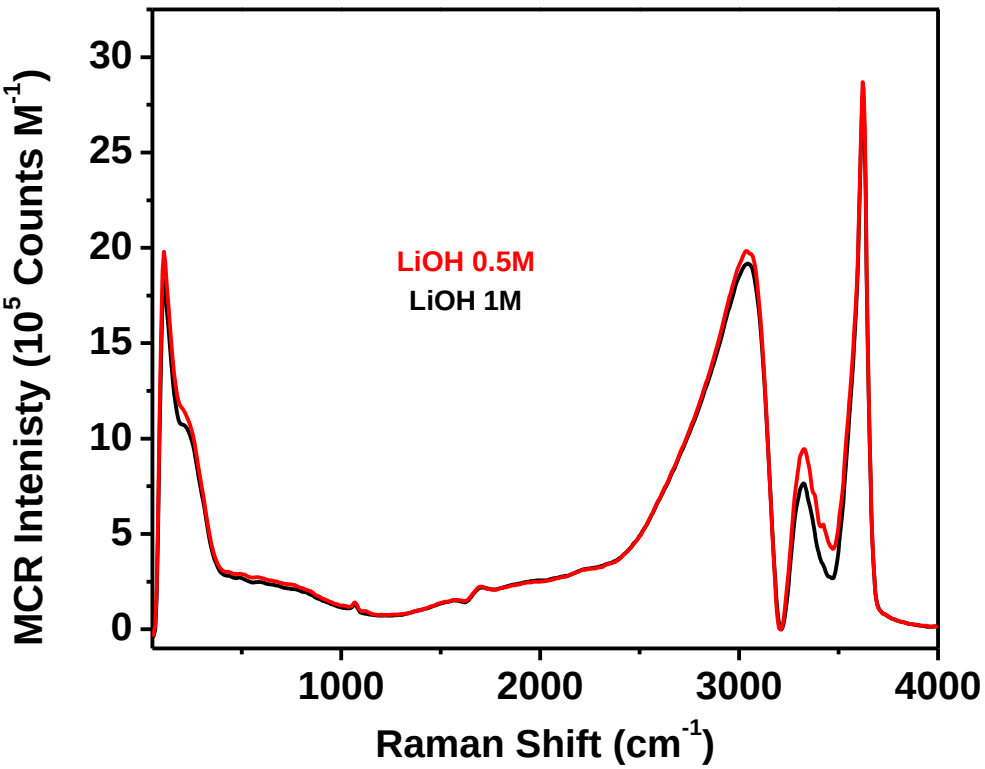

Figure **2-7**: Concentration normalized LiOH spectra at two different concentrations. This was collected with a sharper filter that cuts off at a lower frequency.

This is strong evidence that ion pairing persists below 1 M in the case of this salt. These results stand in sharp contrast to data for acid solutions (e.g. HCl), where the lowest concentration at which ion pairing could be detected between acid protons and halide anions was just above 2 M.[63,64,75] Given these observations, it should be concluded that Li^+ interactions with OH^- are significantly stronger than Cl^- interactions with H^+. Finally, the sharp feature at ~ 3630 cm^{-1} in the Raman-MCR spectra has long been assigned to the hydroxide ion stretch.[61,84,85,91,92]

Vibrational Frequency Calculations

Next, the vibrational frequency of water and hydroxide stretching modes was calculated from simulation trajectories. The O-H bond of interest in an AIMD snapshot was stretched over a range from 0.70 to 1.90 Å in 16 steps to calculate a one-dimensional (1D) potential energy curve. We used CP2K to perform these single-point energy (SPE) calculations, deviating from previously implemented methods. This allowed us to use the exact same basis set, functional, and dispersion correction as in our AIMD simulation protocol, as well as to preserve the periodic conditions of the box for the SPE calculations. The resulting 1D Schrödinger equation was solved with the discrete variable representation (DVR) approach.[93] The frequency of interest was calculated by subtracting the ground state energy from the first excited state energy, and dividing by $\hbar$.

For each of the 800 (or 1,600) individual snapshots extracted from each simulation, vibrational frequencies of O-H stretching modes were compiled, and either transition dipole moment integral (TDMI)-weighted or transition polarizability integral (TPI)-weighted histograms were constructed to represent IR or Raman spectra, respectively, which incorporate nuclear quantum effects of proton nuclei. The hydroxide in every snapshot is defined by systematically assigning every oxygen atom to a hydrogen atom governed by whichever oxygen was spatially closest to each hydrogen. The first solvation shell waters for every OH^- are similarly assigned by oxygen-to-oxygen distances, described in detail below.

As mentioned above, the current protocol for vibrational frequency analysis deviates from previous methods which employed the B3LYP functional and the 6-311++G(d,p) basis set, as this combination was found to accurately capture O-H stretch frequencies in line with experiment.[75,94-96] With the prior method, there exists a tradeoff between the accuracy of the vibrational frequency calculated and the cost of the DFT calculations: as the number of molecules included in the explicit quantum region increases the cost of the calculation increases, but so does

the accuracy of the calculated frequency. We removed the need for a defined quantum region with our CP2K vibrational frequency protocol. There is a clear dependence of the vibrational frequencies on the choice of functional; however, this discrepancy was mitigated by employing a scaling factor, *c*, to adjust our BLYP-D3/TZVP-GTH frequencies to correspond to those from B3LYP/6-311++G(d,p) calculations. The scaling factor is defined below (Equation **2-3)**.

$$c = \frac{\sum(\nu_i \cdot \omega_i)}{\sum \omega_i^2} \qquad \text{Equation } \mathbf{2\text{-}3}$$

c is the scaling factor, $\{\nu_i\}$ is the set of B3LYP/6-311++G(d,p) vibrational frequencies and $\{\omega_i\}$ is the set of BLYP-D3/TZVP-GTH frequencies for the same set of snapshots. This is shown in Figure **2-8**.

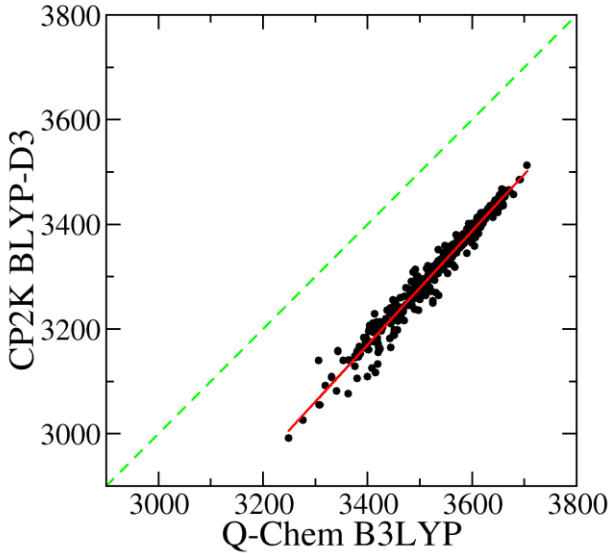

Figure **2-8**: Correlation between calculated vibrational frequencies from the new CP2K protocol against those from the Q-Chem protocol (black points). The green dashed line shows perfect correlation between the two protocols.

We calculated a scaling factor of 1.065 from a set of 509 frequencies from the 0.5 M OH^- simulation. This scaling factor was subsequently used to scale all calculated vibrational frequencies in our three simulations. Prior to calculating the scaling factor, frequencies from our CP2K protocol

were compared against experimental data. We found that for the O-H stretch frequency, B3LYP/6-311++G(d,p) frequencies aligned better with experimental data than unscaled BLYP-D3/TZVP-GTH frequencies.

Frequency histograms can be converted into IR and Raman spectra to compare to experimental data with the application of a judicious weighting factor as described above. Such practices account for non-Condon effects, which are known to be manifest in liquids with strong hydrogen bonding networks, and they indicate a dependence on the coordinates of all molecules in the system of the vibrational transition dipole moment.[94,96] Thus, by weighting frequencies with the TDMI, we more accurately produce an IR spectrum while TPI weighting produces a comparable Raman spectrum.[75] The TDMI can be calculated by $\mu_{01} = \sqrt{\sum_{i=x,y,z}\langle 0|\mu_i(r_{OH})|1\rangle}$ where $\langle 0|$ is the ground state wave function and $|1\rangle$ is the wave function of the first excited state for proton nuclei produced by the DVR analysis. Each component of the dipole moment (x, y, z) as experienced along the distance, r_{OH}, between the oxygen and hydrogen of the O-H bond of interest is represented by $\mu_i(r_{OH})$. The TPI is given by $\alpha_{01} = \langle 0|\alpha(r_{OH})|1\rangle$ where $\alpha(r_{OH})$ is the isotropic static polarizability experienced along the length of the O-H bond. Daly *et al.* derived a relationship between the TDMI squared and vibrational frequencies, to which we then fit a quadratic function, and a linear relationship between the TPI squared and frequencies.[75] This allowed corresponding TDMI and TPI data to be calculated solely from vibrational frequencies with the correct relation equation. The quadratic relationship for the TDMI is $\mu_{01} = (4.986 \times 10^{-5})^2\omega^2 - 0.3857\omega + 756.8$, and the linear relationship for the TPI is $\alpha_{01} = 1.0785 + (9.6337 \times 10^{-4})\,\omega$.[75]

It is important to note that the relationships for the TDMI and TPI depend *only* on the vibrational frequency, ω. Thus, the Li^+ and Na^+ counterions can only impact the calculated IR and Raman intensities in so much as they perturb individual OH vibrational frequencies. Quantum chemical calculations using an explicit electron correlation method (MP2) and a large triple-zeta

basis set with diffuse functions (aug-cc-pVTZ) reveal specific effects of the counterions on Raman intensities in optimized X^+ --- OH_2 complexes in the gas-phase. In particular, the ratio of the Raman intensity of the symmetric stretch vibration of water in Li^+ --- OH_2 relative to Na^+ --- OH_2 is 0.676, which represents a ~ 50% attenuation for Li^+ compared to Na^+. Thus, intensity weighted histograms are shown below only for a control simulation of 0.5 M OH^- without any counterions because the frequency-dependent relationship for the TPI is not appropriate for NaOH and LiOH solutions. Unfortunately, the cost of directly calculating the TPIs and TDMIs for the thousands of OH vibrations in the sampled snapshots from the LiOH and NaOH AIMD simulations is prohibitively expensive. The effect of the counterions on the IR transition dipoles is less dramatic (there is an 11.7% enhancement of the transition dipole moment of the asymmetric stretch of water in Li^+ --- OH_2 relative to Na^+ --- OH_2), thus we report TDMI values for solvent shared ion pairs below.

Consistent with previous studies, the AIMD simulations revealed a distinct hydration structure around the OH^- solute.[49,55] This is demonstrated below (Figure **2-9)**.

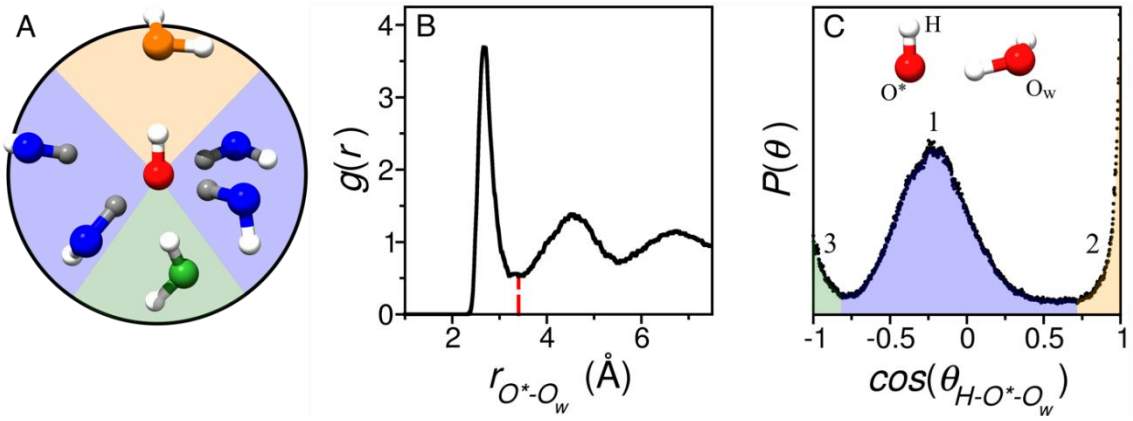

Figure **2-9**: (A) Schematic representation of first solvation shell water molecules of hydroxide. Region 1 water molecules are shaded in blue. (B) The radial boundary of the first solvation shell is defined by the first minimum (vertical dashed red line) of the radial distribution function, $g(r)$, for the hydroxide oxygen, O*, to the water oxygen, O_W. (C) The angular boundaries of the three distinct regions of first solvation shell water molecules are defined by the minima in the distribution of cos(H-O*-O_W). The colored coding in (C) corresponding to coding used in (A).

Based on the structural analysis, the hydration shell water molecules were sorted into three regions using both distance (Figure **2-9** B) and angular (Figure **2-9** C) criteria. These criteria are summarized below (Table **2-2)**.

Table **2-2**: Criteria for each system used to define and sort water molecules around hydroxide into regions within the first solvation shell. Boundary 1 refers to the cutoff between Regions 1 and 2 (blue and orange) and Boundary 2 is the cutoff between Regions 1 and 3 (blue and green).

System	1st Minimum RDF (Å)	H-O-O Boundary 1 (º)	H-O-O Boundary 2 (º)
0.5 M OH^-	3.4075	43.92	144.00
1.0 M LiOH	3.2212	51.48	155.88
1.0 M NaOH	3.3215	44.82	159.30

The first and most populated region is comprised of water molecules donating hydrogen bonds to the OH^- oxygen (Figure **2-9**, blue shading, Region 1). Region 2 consists of water accepting a hydrogen bond from the OH^- hydrogen (orange shading) and Region 3 falls directly below the OH^- oxygen (green shading). The O-H bonds in Region 1 could be further sorted into Regions 1a

and 1b, corresponding to OH groups donating hydrogen bonds to OH^- and OH groups donating hydrogen bonds to second hydration shell water molecules, respectively.

From all calculated O-H stretch vibrational frequencies, calculated spectra comparable to experimental IR and Raman spectra are developed by TDMI- and TPI-weighting histograms, respectively. The weighted histograms below (Figure **2-10)** are from the 0.5 M OH^- simulation.

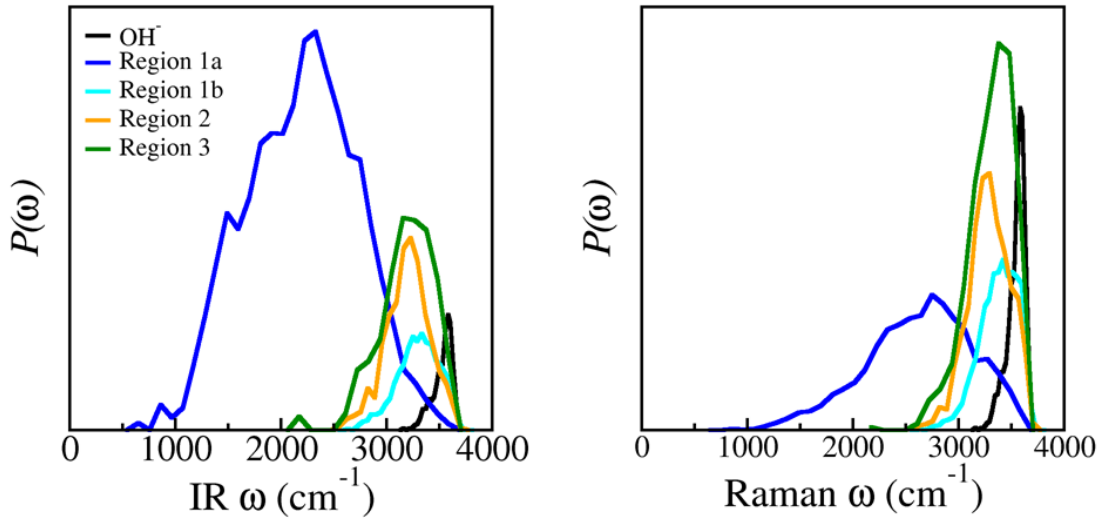

Figure **2-10**: Calculated TDMI-weighted histogram (left) and TPI-weighted histogram (right), corresponding to IR and Raman spectra, respectively. The data are plotted as individual regions as previously defined (Figure **2-9**) to help determine which type of hydration shell water molecules give rise to particular frequencies.

Qualitatively, these spectra can be compared with experimental MCR spectra given above (Figure **2-6** & Figure **2-7**). The largest intensities are observed for Region 1a protons in the IR spectrum between ~ 950 and 3200 cm^{-1}. Raman intensities provide richer detail in the high frequency region of the spectrum between ~ 3000 and 3700 cm^{-1}, which is dominated here by localized hydration shell protons and OH^-. The hydroxide O-H stretching mode peak at ~ 3550 cm^{-1} aligns with the experimental feature observed at ~ 3630 cm^{-1} in the Raman-MCR spectrum and prior assessments of this feature. The most striking difference between these theoretical spectra and those collected experimentally is that these do not drop to zero intensity around 3200 cm^{-1} as

do the MCR spectra. This is likely a result of the minimum area assumption of the experimental algorithm. In fact, the area under the NaOH spectrum (green curve in Figure **2-6** C) reveals that ~ 4 water molecules contribute to the experimental MCR spectra. These should be the most perturbed waters in the hydration shell which correspond to Region 1 (Figure **2-9** A & Figure **2-9** C) due to proton delocalization described below. We conclude that Region 2 and Region 3 waters are not likely to contribute to our experimental data.

Ion Pairing Motifs

In order to better understand how solvent-shared ion pairs in LiOH impact the different frequency regions of the vibrational spectrum, we have measured concentration dependent spectra of NaOH. This is shown in Figure **2-11**. This is made possible by understanding that O-H bonds which point at the hydroxide oxygen atom are found between ~ 950 and 3205 cm^{-1} while those which point away are found at higher vibrational frequencies as revealed below (Figure **2-11)**.

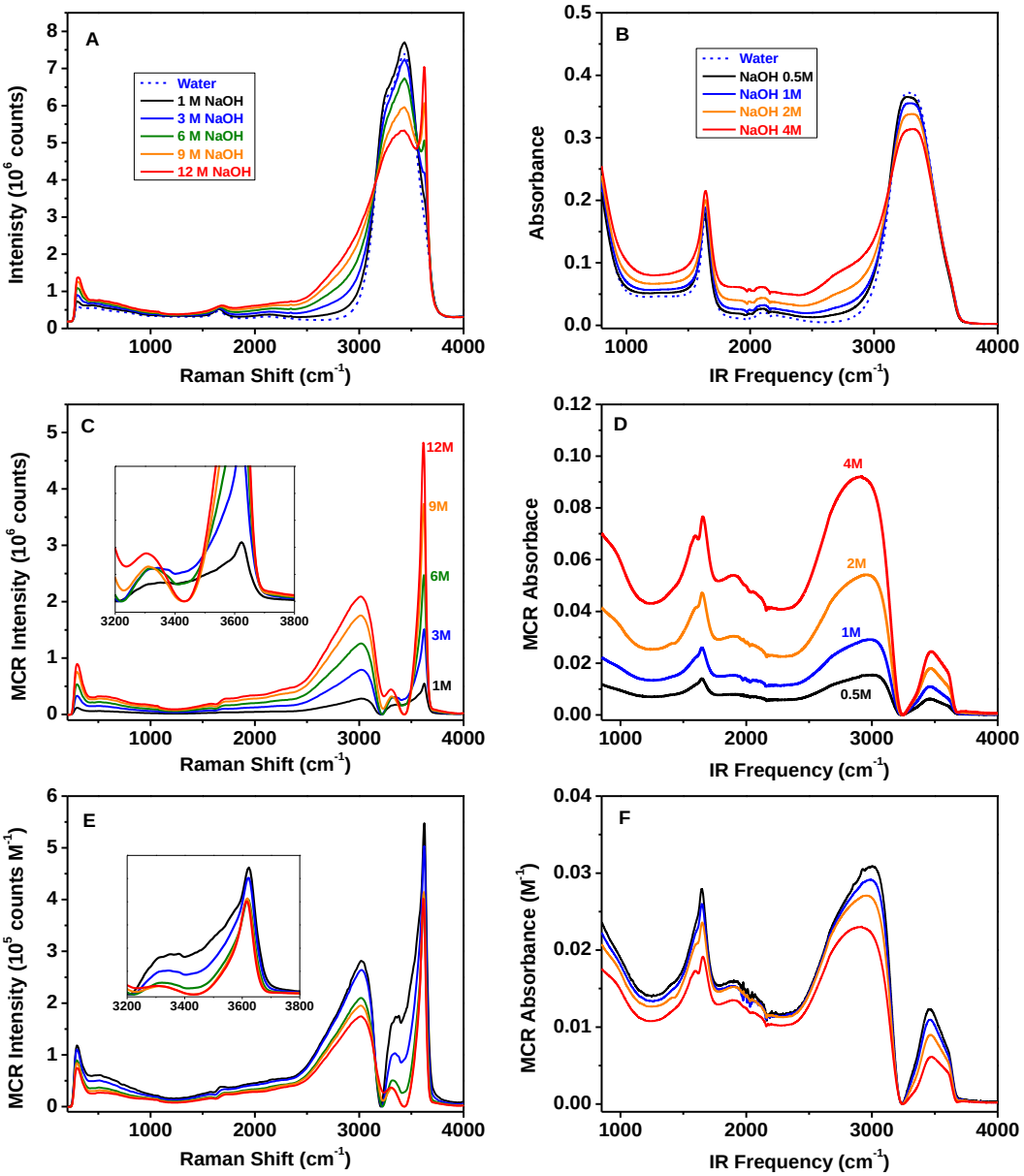

Figure **2-11**: (A) Raw Raman spectra of water as a function of NaOH concentration. (B) Raw ATR-FTIR spectra of water as a function of NaOH concentration. (C) Raman-MCR SC component spectra of NaOH solutions as a function of concentration. The inset shows a close-up of the 3200 to 3800 cm^{-1} region. (D) IR-MCR SC component spectra of NaOH solutions as a function of concentration with constant background subtraction. (E) Raman-MCR data from (C) normalized to the solute concentration. Again, the inset is a close-up of the 3200 to 3800 cm^{-1} region. (F) IR-MCR data from (D) normalized to the solute concentration.

Concentration dependent spectra (Figure **2-11** A & Figure **2-11** B) show an enhancement in intensity in the spectral region assigned to Region 1a protons (between 950 and 3200 cm^{-1}, Figure **2-10** dark blue curves) with increasing concentration. Simultaneously, the intensity at high frequencies decreases with increasing NaOH concentration, as the concentration of bulk water decreases. The Raman spectra (Figure **2-11** A) show an increase in the OH^- signature intensity (~ 3630 cm^{-1}) as a function of concentration. When the MCR algorithm is applied to these spectra (Figure **2-11** C & Figure **2-11** D), the total concentration of Region 1a protons (between 950 and 3200 cm^{-1}) increases in both the Raman and IR spectra with increasing NaOH concentration. However, the Raman-MCR spectra reveal details of Region 1b modes (Figure **2-11** C inset). As the concentration increases, the intensity at 3470 cm^{-1} is attenuated, which can nominally be considered to be a result of ion pairing. This is not nearly as discernable in IR-MCR spectra (Figure **2-11** D) due to non-Condon effects.

As the concentration increases, so does the total amount of perturbed water molecules. The raw SC component intensities can be normalized by the concentration to give "per ion" intensities (Figure **2-11** E & Figure **2-11** F). In the Raman-MCR spectra, intensity below 950 cm^{-1} is assigned to collective modes of water molecules (hydrogen bond stretches and liberations) perturbed by OH^-. This intensity is attenuated as the number of perturbed waters "per ion" decreases. The intensity between 950 and 3200 cm^{-1} in both Raman-MCR and IR-MCR spectra is also attenuated as the concentration of Region 1a protons is reduced. The intensity above 3200 cm^{-1} in both Raman-MCR and IR-MCR spectra is attenuated in the same manner as that below 950 cm^{-1} in Raman-MCR spectra as NaOH concentration increases.

These findings suggest that direct contacts between hydroxide and metal cations attenuate intensity across the entire spectrum, while the conclusions provided above which are based on Figure **2-4**, Figure **2-6** and quantum chemical calculations of the solvent-shared water Raman cross section suggest that solvent-shared pairs attenuate the intensity of Region 1b bonds alone. To

determine if solvent-shared pairs in LiOH are the most consistent with the above data and Figure **2-10**, we have added extra Li^+ cations to these solutions by spiking them with LiCl. In this case, the reference solution used in the MCR analysis was a solution of matching LiCl concentration, instead of pure water. This was done in an effort to eliminate intensity of Cl^- hydration shells from mixed LiOH/LiCl solutions. The results are shown below (Figure **2-12)**.

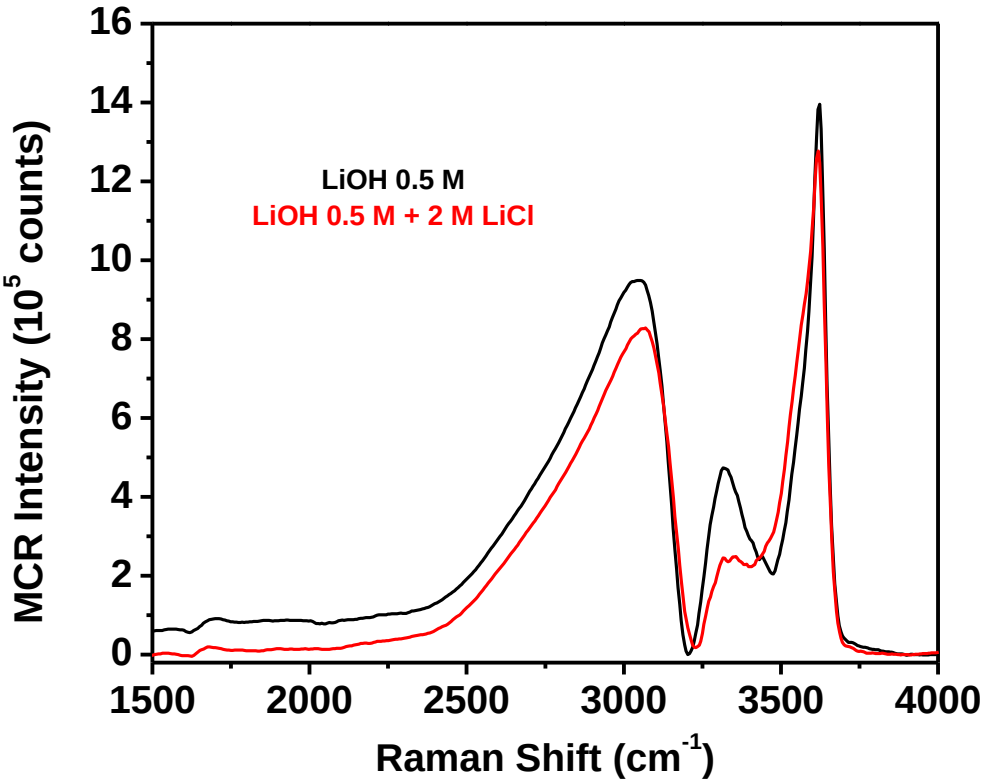

Figure **2-12**: Raman-MCR of mixed salt solutions. A spectrum of the hydroxide hydration shell is given for a solution of 0.5 M LiOH (black curve). This spectrum is analogous to that provided in Figure **2-7**. A spectrum of a solution containing both 0.5 M LiOH and 2 M LiCl (red curve) is also shown.

The red spectrum in Figure **2-12** shows the vibrations of hydroxide's hydration shell in the mixed salt solution. It is apparent that addition of extra cation gives rise to a contact ion pair because the intensity is attenuated across the entire vibrational spectrum including the region assigned to

Region 1a O-H bonds. This supports our conclusion that solvent-shared ion pairs are present in solutions containing LiOH alone.

Interpreting Vibrational Spectra with AIMD

Different degrees of proton delocalization in the AIMD simulations can be quantified through a delocalization parameter, σ, which is defined as the full width at half-maximum (FWHM) of the proton probability density ($|\Psi_0|^2$) in the vibrational ground state as shown below (Figure **2-13**).

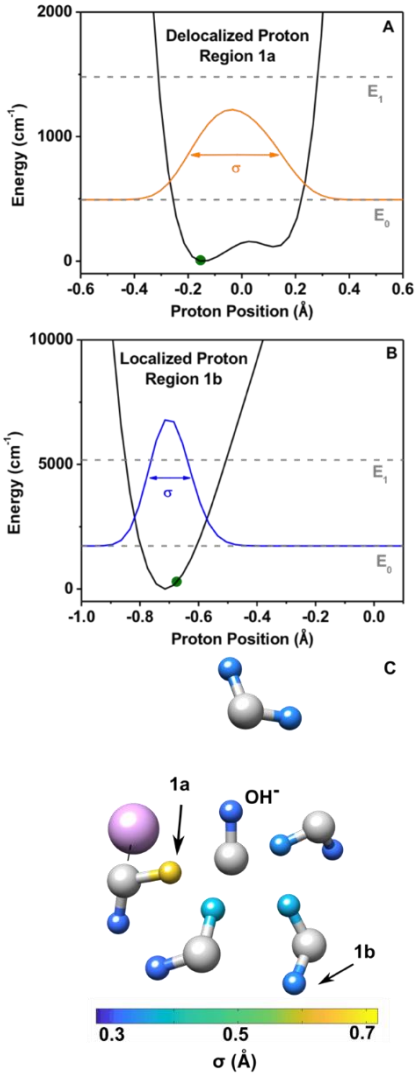

Figure **2-13**: (A) Potential energy curve (shown in black) of a Region 1a proton. The ground and first excited state energy levels are depicted by grey, dashed lines, while the ground state proton wave function squared, $|\Psi_0|^2$ is represented by the orange curve. (B) Potential energy curve (shown in black) of a Region 1b proton, ground and first excited state energy levels (grey, dashed lines), and $|\Psi_0|^2$ (blue). Different scaling of x- and y- axes are used in (A) and (B). Negative x-axis positions correspond to protons closer to the hydration shell water oxygen, and positive positions correspond to the proton being closer to (A) the hydroxide oxygen and (B) a second hydration shell water oxygen, respectively. The green circles on each potential energy curve depict the classical position of each proton, respectively. (C) A delocalization heat map of a hydrated hydroxide complex from the 1.0 M LiOH simulation, where σ is calculated as depicted in (A) and (B). The data in (A) corresponds to the yellow proton labeled 1a, and the same for the data in (B) and the blue 1b proton. Each of these protons are marked with an arrow. All oxygen atoms are colored grey to highlight differences in σ between the protons. The purple sphere represents Li^+.

Region 1a protons are quantum mechanically delocalized to a greater extent than other protons in the hydration shell. For comparison, $\langle\sigma\rangle$ for Region 1a protons averaged over all snapshots was 0.382 Å and 0.376 Å for the LiOH and NaOH simulations, respectively. Averages for every other region in both simulations fell near the average of bulk water simulations at 0.336 Å. Moreover, Region 1a protons gave rise to vibrational intensity primarily between 1000 and 3200 cm^{-1}, while localized protons (Regions 1b, 2, 3 in Fig. 4) and the OH^- itself gave rise to intensity above 3200 cm^{-1} (Figure **2-10**). These calculations support the assignments of distinct frequency regions in the vibrational spectra (Figure **2-6**). Although there are typically three or four water molecules donating hydrogen bonds to the OH^- oxygen within the dynamical hypercoordination mechanism, the delocalization mapping shows that there is always one Region 1a proton that is more delocalized than the others (Figure **2-13** C, yellow proton). This is consistent with the concept of a "most active" hydrogen bond within the confines of the dynamical hypercoordination mechanism.[49,53] Furthermore, Region 1a protons are shared more evenly between oxygen nuclei compared to Region 1b protons (i.e., the proton position in Figure **2-13** A is closer to zero than in Figure **2-13** B).

By contrast with the Raman spectra, the transition dipole moments in the IR spectra for the delocalized protons are far more sensitive to the local environment of the proton (Figure **2-6** D).[94-96] As a result, IR-MCR hydration shell spectra can report on proton delocalization as a function of counter cation identity. These spectra display subtly enhanced intensity in the presence of Li^+ relative to Na^+ or K^+ counter cations at frequencies that can be assigned to Region 1a protons. As noted above, in the Li^+ spectrum, the IR-MCR intensity does not show a pronounced minimum near 3238 cm^{-1}. This suggests proton sharing is enhanced in LiOH solutions. This result raises an interesting question as to how counter cations influence proton sharing. As such, in the AIMD simulations, we focused on snapshots with a solvent-shared water molecule between OH^- and a metal cation. Specifically, the average displacement coordinate, $\langle\delta\rangle$, $\langle\sigma\rangle$, and the TDMI were

calculated for any Region 1a proton within a solvent-shared ion pair for the LiOH and NaOH trajectories. The averaged values are shown below (Table **2-3)**.

Table **2-3**: Averages of the proton displacement coordinate, $\langle\delta\rangle$, the FWHM of the ground vibrational state proton density, $\langle\sigma\rangle$, and the transition dipole moment integral, $\langle\psi_0|\mu|\psi_1\rangle$, for solvent-shared ion pairs. Solvent-shared ion pairs occur when a water molecule simultaneously resided in the first hydration shell of both hydroxide and a counter cation. Standard deviations of the averages are included in parentheses.

Solution	$\langle\boldsymbol{\delta}\rangle$ (Å)	$\langle\boldsymbol{\sigma}\rangle$ (Å)	$\langle\boldsymbol{\psi_0}\|\boldsymbol{\mu}\|\boldsymbol{\psi_1}\rangle$ ($\boldsymbol{D}$)
LiOH, 1 M	-0.868 (0.075)	0.383 (0.016)	112.3 (27.6)
NaOH, 1 M	-0.970 (0.072)	0.367 (0.019)	84.2 (32.8)

Based on these calculations, the modest enhancement of Region 1a intensity in the IR-MCR spectra of LiOH arose from greater proton sharing within Li^+-OH_2-OH^- complexes. The proton displacement coordinate is defined using the classical position of the proton nucleus (green dots in Figure **2-13** A & Figure **2-13** B) as $\delta = R_{O_aH} - R_{O_bH}$, where O_a is the hydration shell water oxygen and O_b is the hydroxide oxygen.[48] Given this definition, the displacement coordinate values will always be negative. The closer in magnitude δ is to zero, the more equally shared a proton is between the oxygen nuclei of hydroxide and first shell water. As shown in Table **2-3**, Region 1a protons are shared more equally between oxygen nuclei and Li^+ compared to Na^+. This trend is also observed in the average σ value. Namely, the average is slightly broader for Li^+, indicating that protons are more quantum mechanically delocalized than in the presence of Na^+. Moreover, the calculated TDMI values from Table **2-3** roughly correlate to the spectral intensity observed in the experimental IR-MCR spectra (Figure **2-6** D).

Finally, the bending mode is split in the OH^- IR-MCR spectra in the presence of Li^+ (Figure **2-6** D inset). The line shape is similar to that from direct subtraction difference spectra and MCR spectra for hydrated proton IR data.[60,75,97] These findings suggest that the splitting of the bending mode for the hydration shell water in 1D spectra reports on sharing of proton nuclei. To explore

this point further, experiments were performed in D_2O and showed significantly less splitting. This data is shown below (Figure **2-14)**. This was expected, as delocalization and sharing should be attenuated in deuterated samples.[49] Also, the inset in Figure **2-6** D shows that switching from hydroxide solutions to KCl completely removed the splitting as well as the intensity on the low frequency side of the bending resonance. Therefore, the splitting is indeed related to the presence of the hydroxide. In the hydroxide solutions, there is a strong dependence for the splitting on the counter cation. The greatest splitting is observed in LiOH solutions, followed by NaOH, and then KOH. Based on these results, there appears to be enhanced proton delocalization and sharing in solutions containing Li^+ relative to other cations.

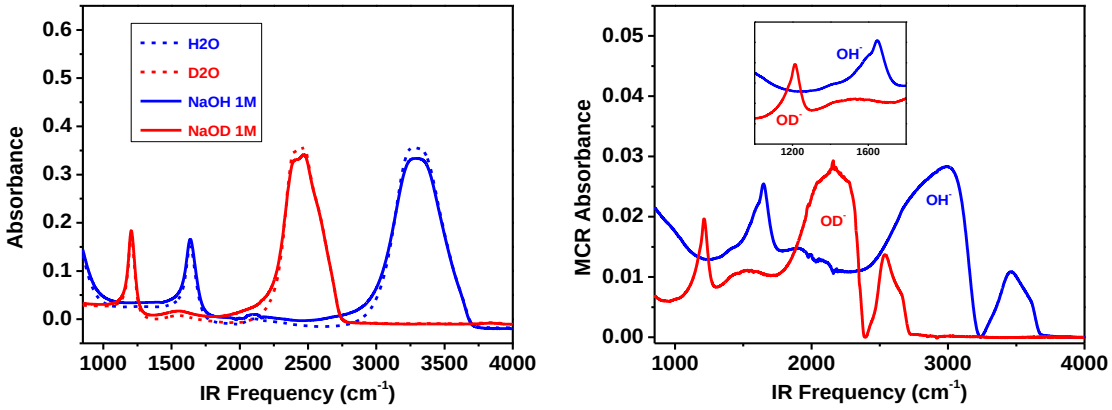

Figure **2-14**: (Left) Raw ATR-FTIR spectra of pure solvents H_2O and D_2O (dashed blue and red curves, respectively) and 1M NaOH and 1M NaOD solutions (solid blue and red curves, respectively). (Right) IR-MCR spectra of OH^- (blue) and OD^- (red) solutions. These spectra are attributed to features of the hydroxide anion and its first hydration shell.

The raw spectra in Figure **2-14** show little variation between pure solvent and mixture spectra as a function of isotope at 1 M concentrations. However, MCR spectra do show attenuation of the continuum region for shared nuclei in OD^- spectra, but direct comparison of intensity is difficult because analogous features in such spectra lie at different vibrational frequencies. As such, the non-Condon effect on transition dipole moments in these spectra differ for corresponding

resonances. The shape of the bending mode is most telling. The inset highlights differences in the bending mode of water molecules hydrating OH^- or OD^-. As discussed above, the shape and splitting of this mode in 1D spectra are known to arise in solutions which exhibit charge transfer and proton sharing.[60,75,97] This is more pronounced in the case of OH^- hydration compared to OD^- hydration. As such, the line shape of the bending mode for hydration water molecules split to a greater extent in solutions with enhanced sharing of proton nuclei. This is the effect of counter cations on the OH^- hydration shell. To verify that this line shape did not originate from cation hydration, we also collected IR-MCR spectra of LiCl and KCl and did not find any difference in the bending mode there.

Diffusion Data and Vibrational Spectra

The diffusion constant data in Figure **2-3** clearly show that that mobility is lower in the presence of Li^+ compared to the other two cations. On the other hand, the IR-MCR data indicate more proton delocalization with Li^+ (Figure **2-6** D). As such, there is not a straightforward relationship between the extent of proton delocalization in water molecules that are hydrogen bonded to hydroxide and the overall OH^- diffusion process. Li^+ counter cations have higher charge density than the other monovalent metal cations and polarize water around OH^- more efficiently. Moreover, water protons coordinating with the hydroxide oxygen are less tightly bound to the donating water molecule and more delocalized across the transfer coordinate with Li^+ compared to Na^+ or K^+. This increased delocalization, however, does not translate into increased solution conductivity and faster diffusion. In fact, despite increased proton delocalization, Li^+ exhibits stronger electrostatic attraction and ion pairing to OH^-, which reduces the diffusion coefficient,

rather than enhancing it. Such pairing explains the slower diffusion of ions in LiOH solutions at concentrations as low as 10 mM, where simple additivity fails to explain the experimental data.

Conclusions

We have shown that specific cation effects are important for hydroxide mobility and proton sharing in hydroxide solutions. AIMD simulations and experimental vibrational hydration shell spectra suggest strong electrostatic attraction between OH^- and Li^+ cations that results in stronger ion pairing than with other cations. This ion pairing is stronger than that previously reported in acidic solutions and persists into very dilute solutions. Li^+ enhances proton sharing in the first hydration shell compared with other cations, but this does not lead to an enhancement in the diffusion coefficient. In fact, direct interactions with well hydrated counter cations impede OH^- mobility. Importantly, ion pairing in solutions of HCl and HNO_3 have not been observed until higher concentrations of ~ 2 M. The fact that we find ion pairing in our data at 1 M, and below, reveals an asymmetry in counterion pairing where metal cations and OH^- pair more tightly than H^+ and halide anions. This allows us to comment on observations of greater Grotthuss enhancement for H^+ than OH^-. It appears that differences in counter ion pairing contribute to this asymmetry, in addition to the aforementioned differences in hydration shell structure proposed by the dynamical hypercoordination mechanism.

Chapter 3

LOCAL ELECTRIC FIELDS IN AQUEOUS ELECTROLYTES

The local response of a dielectric solvent to the presence of a polar solute molecule is described by Onsager's reaction field theory.[98] In this model, the dipole moment gives rise to polarization in the surrounding solvent which creates a local electric field aligned parallel with the dipole.[99] Onsager's theory is a continuum model that relates this field to the solvent polarity (Equation **3-1**).[99-101]

$$\vec{F}_{rxn} = \frac{\vec{\mu}}{4\pi\varepsilon_0 a^3}\frac{2(\varepsilon_r-1)(n^2+2)}{3(n^2+2\varepsilon_r)} \qquad \text{Equation } \mathbf{3\text{-}1}$$

$\vec{F}_{rxn}$ is the solvent reaction field, $\vec{\mu}$ is the dipole moment of the solute, ε_r is the relative static permittivity of the solvent (ε_r = 78.5 for pure water at 25 ^{o}C), n is the refractive index of the solute, and a is the radius of the cavity occupied by the solute. The local reaction field couples to the solute, which can give rise to Stark shifts in optical and vibrational spectra of polar chromophores.[102-105] As such, altering the solvent's polarity leads to pronounced changes in color of visible dyes through an effect known as optical solvatochromism. Moreover, vibrational solvatochromism has been observed in molecular probes including C=O and C≡N bonds, which can be exploited to measure electric fields in catalysis.[106-110] However, Onsager's theory has not been comprehensively tested upon the addition of salt to solution.

The use of molecular probes to measure local electric fields in the condensed phase relies on preservation of the bond force constant when the probe is exchanged from one environment to another.[111] A vibrational Stark shift is a dipole-field coupling phenomenon whereby the field interacts more strongly with the excited state than the ground state of an anharmonic oscillator due the difference in bond dipole.[102] This results in greater stabilization in the excited state, and the

frequency red shifts from the value observed in the gas phase with increasing solvent polarity. However, a change in electrical anharmonicity of the probe can occur when it participates in hydrogen bonding. For example, charge transfer from a lone pair on carbonyls or nitriles into anti-bonding orbitals on a first shell water molecule can modify the covalent character of the probe.[112] This complicates measurements of electric fields in water. Yet covalent modifications have not been disentangled from effects of through space electric fields in aqueous electrolytes.

Herein, we explore the reaction field in aqueous salt solutions with three forms of spectroscopic experiments and molecular dynamics (MD) simulations. We observe red shifts in the vibrational resonance of hydrated C=O and C≡N bonds as a function of salt concentration between 1 M and saturation conditions with linear vibrational spectroscopy. This observation is at odds with Onsager's model because the bulk dielectric constant of liquid water decreases upon the addition of salt. As such, a blue shift is expected instead of one to the red as we exemplify by dissolving $MgCl_2$ in aqueous solutions containing acetone (Figure **3-1**).

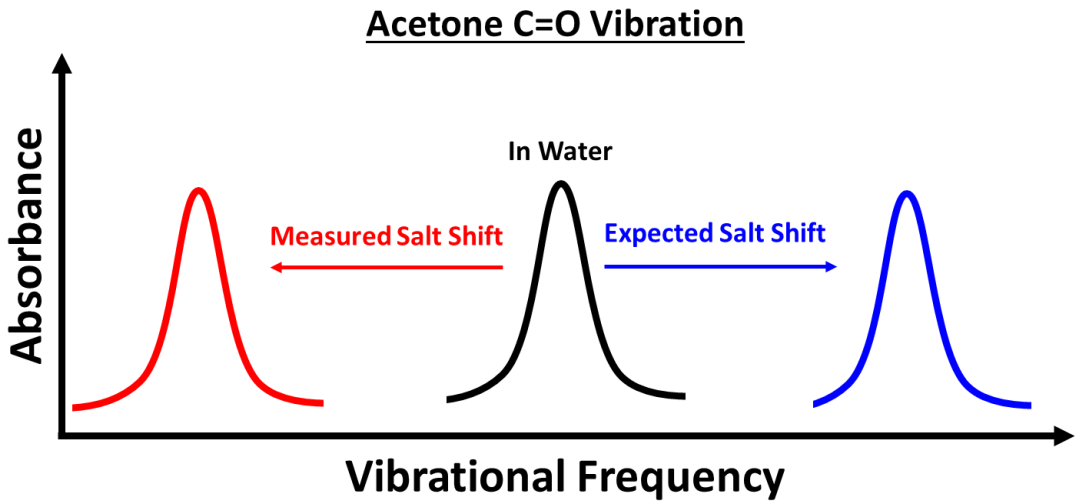

Figure **3-1**: Schematic illustration of the effect of $MgCl_2$ on the C=O stretching mode from acetone. Onsager's reaction field theory (Equation **3-1**) describes how the decrease in bulk dielectric constant should result in weakening of the local field, and thus a shift to higher frequency. Instead, a red shift is observed.

This idea of ‘anti-Onsager’ solvatochromism is in agreement with observations from other works.[113,114] However, the molecular-level mechanism for the red shift and an accurate description of the local field in a salt solution remains elusive.

We apply two-dimensional infrared (2DIR) spectroscopy to solutions containing acetone and do not observe a change in the anharmonicity of the C=O bond upon the addition of $MgCl_2$ to solution. This suggests that ion-induced red shifts do not result from covalent modifications to probe molecules, but rather from the vibrational Stark effect.[115] Moreover, we explore the Stark shift in a large number of experiments using linear spectra where the cation, anion and probe are systematically varied. These studies reveal a sizeable sensitivity of the Stark effect to the identity of both ions of the salt and the probe. Specifically, we find that water-separated pairing between the oxygen atom of carbonyl probes and well-hydrated cations is accompanied by a large red shift in comparison to weakly hydrated cations as described by a direct Hofmeister series. Interestingly, switching from LiCl to LiI nearly doubles the red shift. This suggests counter anions play a limiting role whereby they accumulate around the positive side of the dipole. We perform classical MD simulations and, indeed, find evidence for a double-ion bound structure in aqueous solutions containing acetone and salt. Importantly, switching to a nitrile probe reverses the Hofmeister series in the cation but not the anion. In fact, CsCl red shifts the C≡N stretch the greatest out of chloride salts, and CsI gives rise to yet a larger effect. Therefore, the Stark effect is limited by an apparent match in hydration properties of ions and the probe as opposed to intrinsic properties of ions dissolved in the bulk. These findings suggest that the ‘anti-Onsager’ shift in the bulk solution is governed by water-mediated binding of both the cation and anion to the probe. This structural motif gives rise a local electric field. Holistically, one can envision these findings comprehensively with the following schematic (Figure **3-2**).

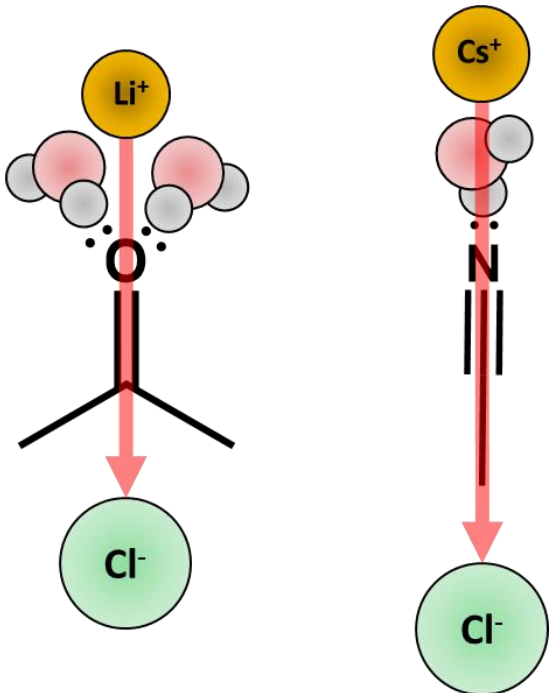

Figure **3-2**: Schematic highlighting our proposed mechanism which governs solvatochromism of vibrational probes in salt solutions. Namely, water-separated ion-dipole interactions form between the probe and both ions of the salt. Well-hydrated cations form pairs with carbonyls while poorly-hydrated cations form pairs with nitriles. The electric field which points from the cation to the anion governs the Stark effect. This is shown by a thick red arrow.

Finally, we find a red shift in fluorescence spectra when PRODAN is dissolved in salt solutions. This demonstrates that 'anti-Onsager' ion effects can impact fluorescence assays, in addition to those performed using vibrational probes.

Vibrational Solvatochromism of Acetone

All samples were freshly prepared before use. The concentration of all carbonyl or nitrile probes was fixed to be 100 mM unless stated otherwise. All carbonyl compounds and accompanying salts were dissolved in D_2O in order to avoid overlap between the H_2O bending mode and the carbonyl or amide I resonances. Reference solutions for linear IR measurements were

prepared by adding salt to D_2O. In future sections, acetonitrile and accompanying salts were dissolved in H_2O to avoid overlap between the D_2O stretch and C≡N resonances.

All materials were used as received. D_2O solvent (99.8% D atom) was purchased from Sigma-Aldrich (St. Louis, MO). All salts used for FTIR and Raman measurements were purchased from Sigma-Aldrich (St. Louis, MO). H_2O (18.2 MΩ·cm) was produced with a Barnstead Nanopure Water System (Thermo Fischer).

All linear IR spectra presented here were collected on a Nicolet Fourier transform (FT) IR spectrometer (Thermo Fischer Scientific, Billerica, MA) equipped with an attenuated total internal reflection (ATR) stage. The intrinsic resolution of our detector was 2 cm^{-1}. This was different from the ATR stage used in Chapter 2 because these experiments were conducted at neutral pH conditions and did not require the same ATR stage. Each spectrum was averaged over 64 scans. Blackman-Harris and ATR corrections were performed on the data. The ATR window was blanked to pure D_2O for experiments conducted at 0 M salt. A solution containing 100 mM of the carbonyl containing compound was then placed on the ATR window. For spectra of C=O vibrations in the presence of salt, the window was blanked to a salt in D_2O solution.

All 2DIR spectra were collected on a home built 2DIR spectrometer. Broadband midIR pulses are generated from an Astrella Laser System (Coherent) outputting 3.5 mJ, 30 fs, 800 nm pulses at a repetition rate of 1kHz. The beam is then directed to a TOPAS prime OPA (Light Conversion) and downconverted in a AgGaS2 based DFG. Pulses are then shaped using an AOM (PhaseTech Spectroscopy) generating the midIR pulses required for the 2D experiment. The waiting time between the pump and probe pulses was fixed at 0 fs for all reported spectra. The probe beam is recollimated after the sample and redirected along with the reference beam to a home-build monochromator then imaged onto a 128 x 128 mid-IR MCT array camera (Catalina, Teledyne). Samples were prepared under dry air and sandwiched between two CaF_2 windows. The laser table was purged under dry air to avoid interference with atmospheric water.

In a first set of experiments, we measured ATR-FTIR absorption spectra of the C=O stretching mode when acetone was dissolved in a series of organic solvents and aqueous $MgCl_2$ solutions (Figure **3-3**).

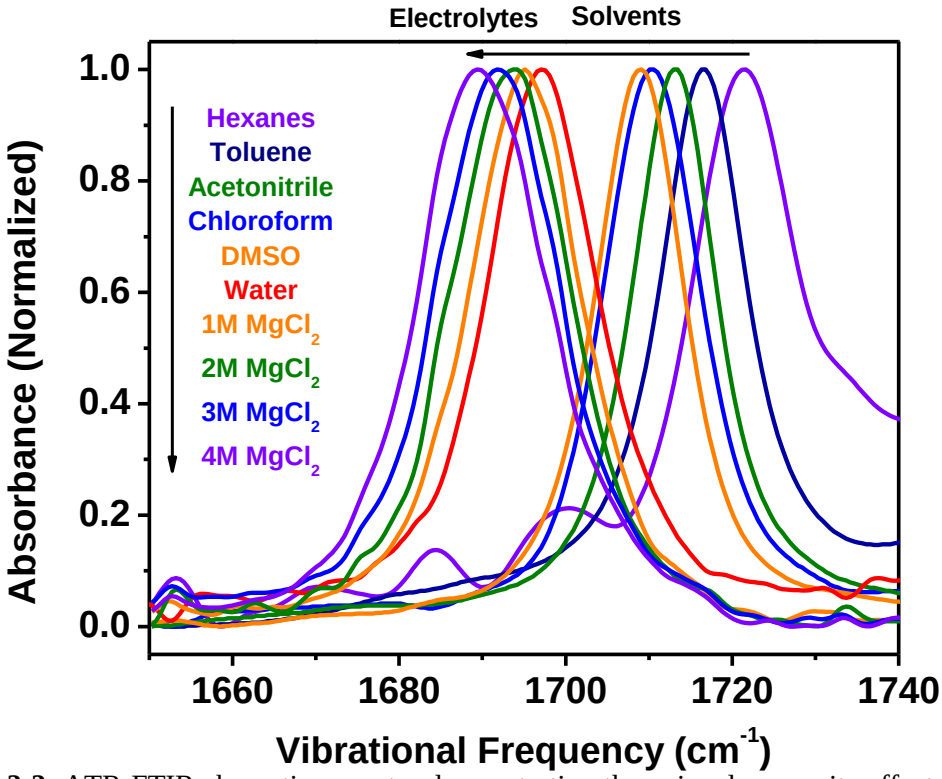

Figure **3-3**: ATR-FTIR absorption spectra demonstrating the uniquely opposite effects of organic solvents and salt solutions on the vibrational frequency of the C=O bond. The gas phase frequency is 1731 cm^{-1}. Both series of spectra are qualitatively color coded from large ε_r (red; D_2O) to low ε_r (violet; 4 M $MgCl_2$ ε_r = 42 on the left, or hexanes ε_r = 1.89 on the right). The black arrows indicate the shift in spectra from right to left correspond to progression down the legend.

Submerging acetone into hexanes from the gas phase leads to a red shift from 1731 cm^{-1} to 1721 cm^{-1}. This effect becomes larger with increasing solvent polarity and reaches 1709 cm^{-1} in DMSO. When the solvent is switched from DMSO to water, a pronounced red shift occurs from 1709 cm^{-1} to 1697 cm^{-1}.

Once in water, the bulk dielectric constant can be significantly lowered by adding large amounts of $MgCl_2$. At a concentration of 1 M, a small red shift is observed from 1697 cm^{-1} to 1695

cm^{-1}. Increasing the salt concentration in 1 M increments to a final condition of 4 M leads to a monotonic red shift in the C=O mode. This is surprising because the bulk dielectric constant of 4 M $MgCl_2$ (ε_r = 42) closely matches that of DMSO (ε_r = 46.84).[101,116] As such, a blue shift is expected instead of one to the red as is indicated by the color scheme in Figure **3-3**.

The continuous shift in the C=O spectrum as a function of salt concentration is reminiscent of a Stark shift.[117] However, it is possible that the C=O bond is instead weakened as salt is added to solution. To distinguish between these two possible explanations, Arnaldo Serrano's group (Notre Dame, IN) measured the anharmonicity of the carbonyl resonance with 2DIR (Figure **3-4**).

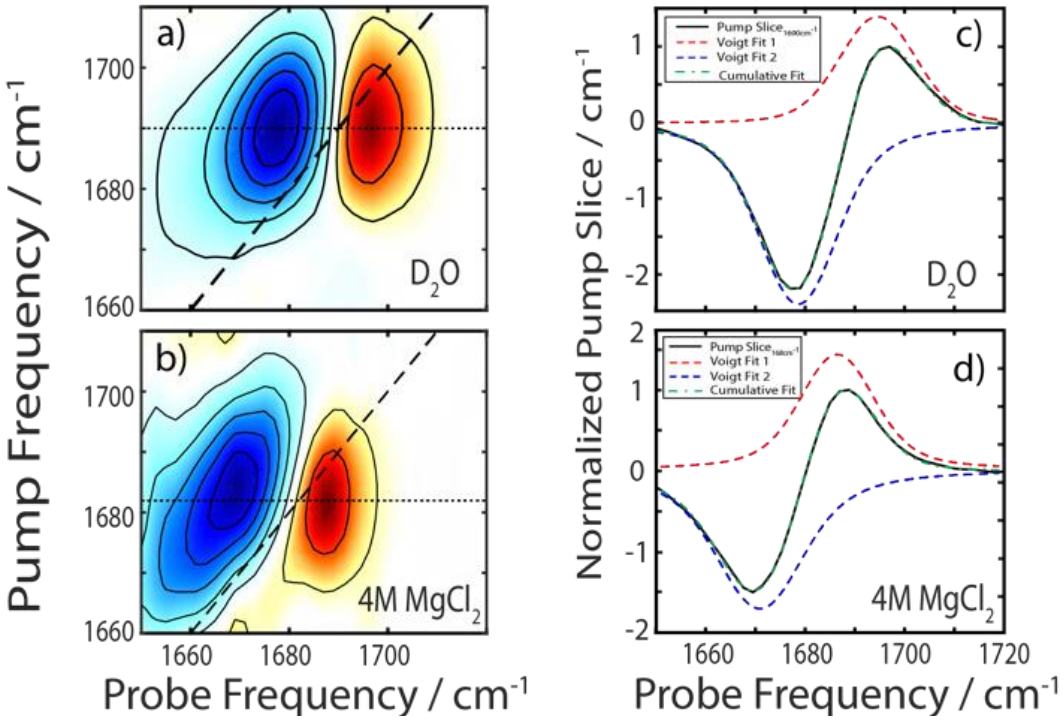

Figure **3-4**: 2DIR spectra of acetone in (A) D_2O and (B) 4 M $MgCl_2$ with horizontal slices taken along the dotted lines at the center of the fundamental frequency. Horizontal slices for each solvent (C) D_2O and (D) 4 M $MgCl_2$ were fit with Voigt functions to obtain the apparent anharmonicities.

Each vibrational mode in a 2DIR spectrum appears as a pair of peaks along the probe axis separated by the anharmonicity.[118,119] The red peak corresponds to the ground state bleach and stimulated emission (0-1 transition) while the blue peak corresponds to the excited state absorption

(1-2 transition) of the C=O bond. In the absence of salt, the frequency of the 0-1 transition is 1690.0 cm^{-1} while that of the 1-2 transition is 1673.8 cm^{-1} (Figure **3-4** A & Figure **3-4** C). Thus, the anharmonic shift of acetone dissolved in D_2O 16.2 cm^{-1}. Both of the resonances red shift upon adding 4 M $MgCl_2$ to solution (Figure **3-4** B & Figure **3-4** D). However, the anharmonic shift measured in the salt solution is 16.0 cm^{-1}. As such, the anharmonicity of the C=O bond is preserved upon addition of salt to solution. This suggests the ion-induced red shift arises from the vibrational Stark effect as opposed to a covalent modification in the probe.[115,117] Moreover, this Stark shift is not governed by Onsager's model.

Interactions Between Cations and Carbonyls

Despite our finding that salt-induced solvatochromisim is a Stark shift, disruptions to the hydration shell by cations are known to modulate the covalent character of C=O bonds.[31,120] We highlight such an effect by changing the identity of the probe from acetone to *N*-methylacetamide (NMA) as shown in Figure **3-5**.

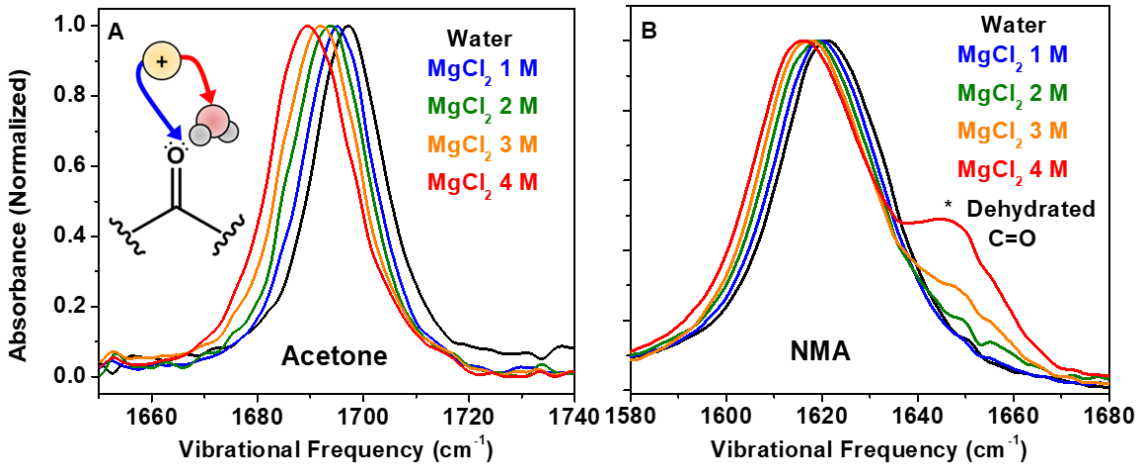

Figure **3-5**: ATR-FTIR absorption spectra of (A) the C=O resonance of acetone and (B) the amide I resonance of NMA. The schematic in (A) depicts how cations influence the frequency of C=O bonds in general. Namely, disruption to the hydrogen bond by contact pair formation results in a blue shift, while water-separated cations apparently contribute to a red shift in the hydrated mode. $MgCl_2$ was systematically added to solution in 1 M increments. The spectra of acetone correspond to the data in Figure **3-3**, shown here for visual comparison with NMA. The contact pair in NMA data denoted by an asterisk arises from disruption to the hydrogen bonds with water molecules, which results in covalent modification to the C=O bond.

The spectra of acetone show a monotonic red shift as a function of salt concentration (Figure **3-5** A) as was revealed in Figure **3-3**. Such an effect is also observed for NMA (Figure **3-5** B). Prior to the introduction of $MgCl_2$, the amide I peak appears at 1620 cm^{-1}. This is red-shifted from that observed for acetone (1697 cm^{-1}) due to contribution from the lone pair on nitrogen. Specifically, this resonance reduces the bond order of the C=O moiety and red shifts the amide I mode away from the ketone mode.

Upon the introduction of $MgCl_2$ to solutions containing NMA, a blue-shifted shoulder appears at 1645 cm^{-1}. This has been argued to arise from dehydration of the carbonyl when in close proximity to the cation in previous works.[120] Specifically, when the molecule is placed into water, a large red shift occurs with respect to the frequency observed in the gas phase due to 1) Onsager's reaction field theory and 2) charge transfer through hydrogen bonds formed between carbonyl lone pairs and first shell water molecules. As such, electron density is placed back onto the carbonyl

when Mg^{2+} disrupts C=O···H_2O hydrogen bonds.[112] This population of NMA molecules has been covalently modified (blue shoulder) compared to those that remain properly hydrated (initial peak).

When the molecule was switched from acetone to NMA in Figure **3-5**, additional electron density was placed on the oxygen atom by resonance with the nitrogen lone pair. This allows Mg^{2+} to overcome its dehydration penalty and interact better with the amide which leads to disruption of hydrogen bonds with water and a blue shift. However, when we change the salt and use $CaCl_2$, a blue-shifted shoulder is observed in spectra of both acetone and NMA (see chapter 4 and Appendix B). This is best explained by the smaller dehydration penalty of Ca^{2+}, which allows this cation to interact better with acetone compared to Mg^{2+}. Since dehydration of the carbonyl results in covalent modification, we hypothesize that the Stark shift in the hydrated mode arises from water-separated ions that act on the carbonyl *via* through space electric fields.

Cation-Specific Interactions with Hydrated Vibrational Probes

In this section, Raman spectroscopy is used to measure samples containing acetonitrile. This was done because the nitrile stretch is highly Raman active, but the signal is poor in the IR. As such, in order to get sufficient signal from samples containing 100 mM of acetonitrile we used Raman instead of IR However, we did increase the nitrile concentration to 500 mM in order to check our findings with IR spectra (see the 'Using Raman and ATR-FTIR to Explore Stark Shifts and Covalent Modifications' section below) and, indeed, found that all observations from Raman spectra were preserved in IR spectra. All Raman spectra were collected on a home-built spectrometer described in chapter 2. In this chapter, signal was sent to our detector that spread the light onto a different grating (1600 g/cm). The signal was binned every 0.7 cm^{-1}. Subpixel drifts were corrected with signal from a helium lamp employed as an internal reference.

In order to better understand how water-separated cations contribute to the Stark shift, we have tested a large number of combinations of probes and salts (Figure **3-6**).

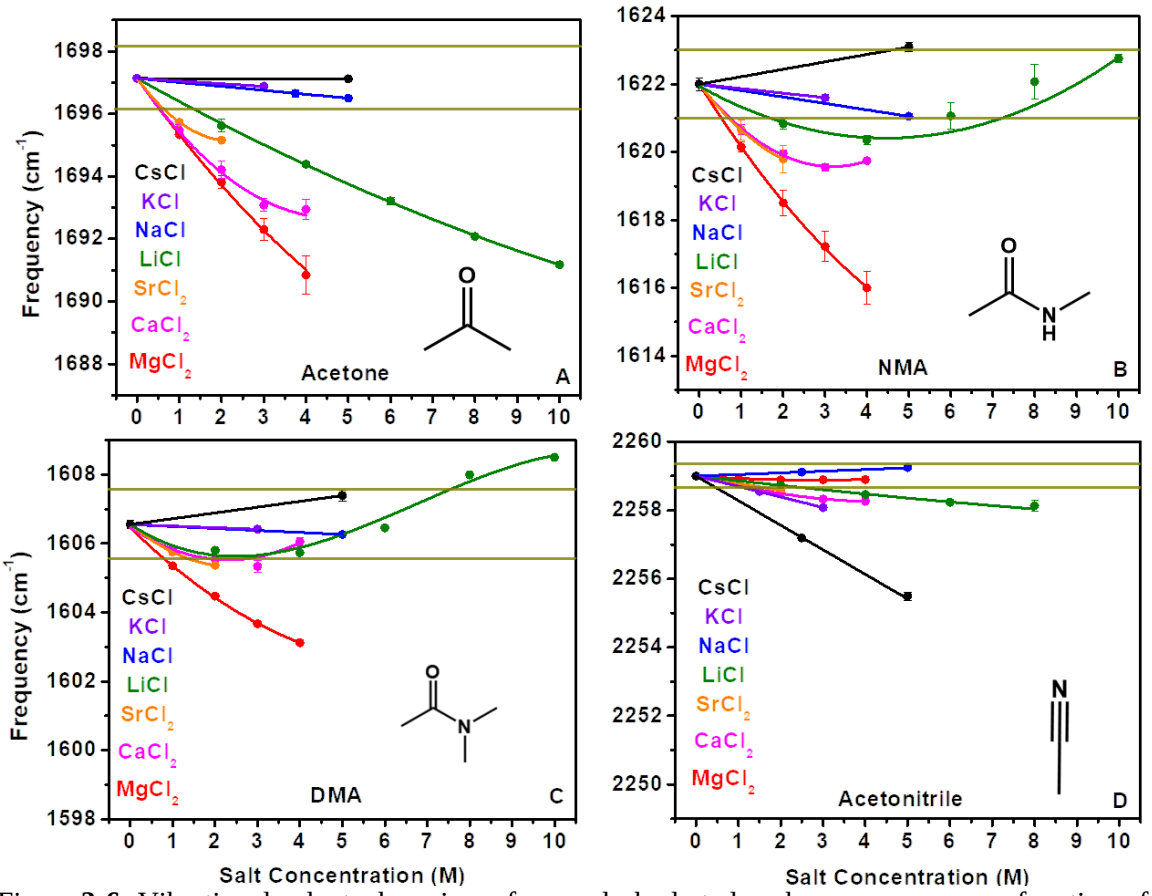

Figure **3-6**: Vibrational solvatochromism of properly hydrated probe resonances as a function of salt concentration and identity. This is shown for (A) acetone, (B) *N*-methylacetamide (C) *N*,*N*-dimethylacetamide and (D) acetonitrile. The colored curves are guides for the eye. Error bars correspond to averages of triplicate measurements. The solid yellow lines demarcate the intrinsic resolution for the data. Lewis structure representations of the probes are provided in their respective panels.

Our library of probe molecules consisted of a ketone (acetone), two amides (NMA & *N*,*N*-dimethylacetamide (DMA)) and acetonitrile. The frequencies provided on the vertical axes correspond to the peak frequency of the properly hydrated mode in each spectrum. We added a family of salts to solutions containing these probes and found evidence for both cation and probe-specific effects. Chloride salts possessing well-hydrated metal cations gave rise to the most

pronounced red shift in the carbonyl frequency (Figure **3-6** A, Figure **3-6** B and Figure **3-6** C). Specifically, a direct Hofmeister series describes this red shift which can be written as:

$$Mg^{2+} > Ca^{2+} > Sr^{2+} > Li^{+} > Na^{+} \approx K^{+} > Cs^{+} \qquad \textbf{(Carbonyl Series)}$$

Next, we observed a reverse cation series in the C≡N stretching frequency of acetonitrile when chloride salts were added to solution (Figure **3-6** D) which can be written as:

$$Cs^{+} > K^{+} > Ca^{2+} \approx Sr^{2+} > Li^{+} > Na^{+} \approx Mg^{2+} \qquad \textbf{(Nitrile Series)}$$

These trends demonstrate that intrinsic properties of ions do not govern the Stark effect. To be clear, our experiments using carbonyls show that highly charge dense cations give rise to the largest shift. This would seem to suggest that the density of electric field lines from ions dissolved in the bulk solution governs the observed effect. However, the complete reversal of the cation series in the case of nitriles speaks against such a mechanism. In fact, it is poorly-hydrated cations like Cs^{+} or K^{+} that give rise to the most pronounced red shift in acetonitrile, while well-hydrated Mg^{2+} cations do not give rise to a red shift at all. We conclude that ions dissolved in the bulk do not govern Stark shifts in our data.

Our observations can be explained based on ion binding in water-separated motifs. This occurs in a way that is reminiscent of the Law of Matching water Affinitas (LMWA). The LMWA is usually used to predict contact ion pair formation is a solution of salt, in which a cation and anion dehydrate and directly interact. Such an ion pair is often distinguished from water-separated ion pairs. These ion pairs are commonly classified as solvent-shared pairs where one water molecule resides in the first hydration shell of both ions simultaneously, or solvent-separated pairs where two waters reside between the ions. The LMWA predicts that ions with similar thermodynamic hydration properties, including ΔG_{hyd} and ΔH_{hyd}, tend to form contact pairs. A similar type of observation arises in this work. Namely, if one classifies C=O bonds as being well-hydrated then it is apparent that water-separated pair formation occurs between carbonyls and well-hydrated cations. Moreover, it is poorly-hydrated cations like Cs^{+} which give rise to the most pronounced

shift in acetonitrile, which suggests the C≡N bond behaves as a poorly-hydrated probe. This apparent application of the LMWA to formation of water-separated ion-dipole interactions has been realized here phenomenologically. As such, it is not quite clear as to why these probes behave as such. What can be said is that carbonyls apparently behave like well-hydrated probes while nitriles behave like poorly-hydrated ones in forming water-separated ion-dipole interactions. This idea suggests that the ion-specific curves in Figure **3-6** do not arise from an apparent change in the Stark tunning rate of the probe as a function of salt identity, but rather from differences in concentration of the ion-bound dipole.

If one were to map the frequency on the vertical axes in Figure **3-6** to a concentration of water-separated ion-dipole pairs, then the ion-specific shifts should quantify ion binding. The nonlinearity observed in our data is the result of a convolution of multiple factors. First, a binding event is expected to result in Langmuir isotherm behavior. However, this binding is extremely weak as it requires the salt to be at least 10 times more concentrated than the probe. Indeed, previous work has shown that cation-amide contact pairs reside on the linear portion of the Langmuir isotherm at these concentrations of salts.[31] There is also overlap between the hydrated peak and a blue shoulder, similar to that presented in Figure **3-5** B, present in many of our spectra. This complicates the expected Langmuir curve. Such overlap can give rise to a blue-shifted contribution instead of one to the red.

Using Raman and FTIR to Explore Stark Shifts and Covalent Modifications

We used Raman spectroscopy to study solutions containing acetonitrile. This was done because the C≡N stretch is far more active in the Raman than the IR, and we wanted to preserve the concentration of the probe in all of our experiments. An interesting question arises as to whether

switching between Raman and IR alters our findings. This can be answered by increasing the concentration of acetonitrile from 100 mM to 500 mM and collecting IR spectra (Figure **3-7**).

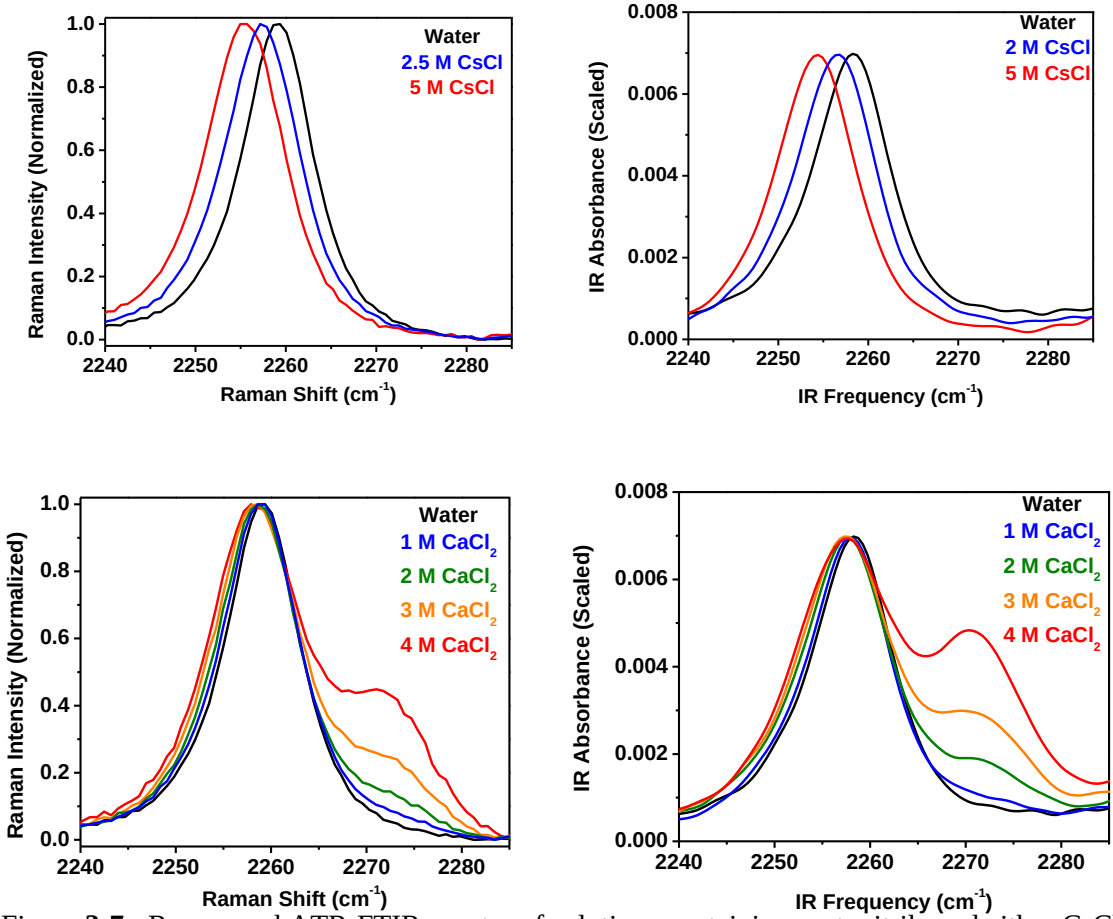

Figure **3-7**: Raman and ATR-FTIR spectra of solutions containing acetonitrile and either CsCl or $CaCl_2$ salts. Raman spectra are shown on the left and IR spectra are shown on the right. The nitrile concentration was 100 mM in Raman experiments, and 500 mM in IR experiments.

When we switched from Raman measurements to ones made with IR spectroscopy, no significant change was observed. Namely, Stark shifts and shoulders are preserved from one form of vibrational spectroscopy to the other. As such, our conclusions made above are valid. Moreover, neither the Stark shift or the blue-shoulder arise as the result of a non-Condon effect. This has the potential to impact the transition dipole in IR spectra or the transition polarizability in Raman spectra. However, if a non-Condon effect was the reason for either observation, then it should not

be observed in both IR and Raman spectra. We conclude that the use of shifts and shoulders to disentangle through space electric fields from covalent modifications in aqueous electrolytes is a valid methodology.

The Local Electric Field

In order to learn how vibrational frequencies of carbonyl and nitrile probes in the bulk solution is Stark-shifted by the presence of local ions, we have switched the counter anion from Cl^- to I^-. Specifically, this was done when well-hydrated Li^+ cations were introduced into solutions containing acetone and when poorly-hydrated Cs^+ cations were added to solutions containing acetonitrile (Figure **3-8**).

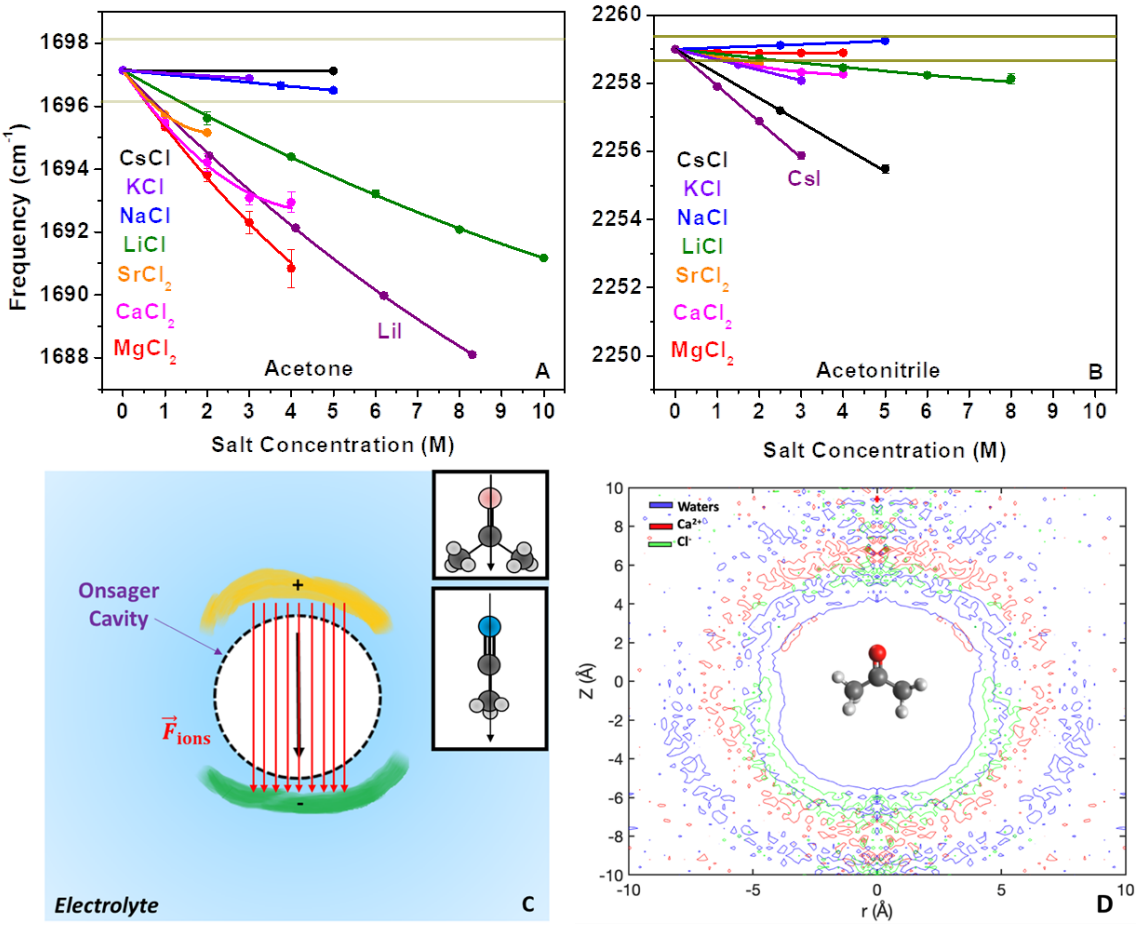

Figure **3-8**: The influence of anions on salt-induced Stark shifts of molecular probes dissolved in the bulk solution. Shifts in the vibrational frequency of hydrated C=O or C≡N bond are shown for (A) acetone and (B) acetonitrile upon replacing LiCl with LiI (dark purple), and CsCl with CsI (dark purple), respectively. (C) Schematic illustration of the proposed mechanism that gives rise to a Stark shift in bulk electrolytes. The yellow region corresponds to cation accumulation and the green region represents the anion. The electric field lines shown in red, $\vec{F}_{\text{ions}}$, depict the net field from accumulation of both ions. The insets depict the mean molecular dipole for acetone (top) and acetonitrile (bottom). (D) A cylindrical distribution function produced from MD simulations of acetone and $CaCl_2$ showing accumulation of Ca^{2+} cations (red), Cl^- anions (green) and water molecules (blue) around the dipole when 4 M of this salt is present in solution.

A much larger red shift is observed upon the addition of LiI to solutions containing acetone compared to when LiCl is present (Figure **3-8** A). In fact, changing the anion nearly doubles the red shift in this case. Moreover, when CsI is introduced to solutions containing acetonitrile, the red shift is enhanced from that caused by CsCl (Figure **3-8** B). These data suggest both ions influence the local electric field. While well-hydrated cations bind to hydrated carbonyl oxygen atoms, it is

pooly-hydrated cations which bind to hydrated nitrile probes. Furthermore, when one switches from Cl^- salts to ones containing I^-, the hydration properties of the anion are altered. Specifically, I^- is more poorly-hydrated than Cl^-. This should allow I^- to sit closer to the positive side of the organic dipole. Previous investigations of Hofmeister anions have, indeed, shown that I^- can interact with hydrophobic moieties better than Cl^-.[4] As such, one should think of the 'anti-Onsager' effect as arising from a double-ion bound structure which mimics a parallel plate capacitor (Figure **3-8** C). When such a structure is present in the bulk solution, the net local electric field from ions, $\vec{F}_{\text{ions}}$, points from the cation to the anion. By symmetry, $\vec{F}_{\text{ions}}$ will always possess a component aligned parallel to the dipole and result in a red shift as revealed by Equation **3-2**.

$$\mathrm{hc}\Delta\bar{\nu}_{\mathrm{salt}} = -\Delta\vec{\mu}\cdot\left(\vec{\mathrm{F}}_{\mathrm{ions}} - \vec{\mathrm{F}}_{\mathrm{water}}\right) \qquad \text{Equation } \mathbf{3\text{-}2}$$

$\Delta\bar{\nu}_{\mathrm{salt}}$ is the shift in the frequency of the probe upon addition of salt to the solution. $\Delta\vec{\mu}$ is the Stark tunning rate defined to be the difference in bond dipole between the ground and first excited vibrational energy levels of the C=O or C≡N bond (see derivation section below). In probes like acetone and acetonitrile, $\Delta\vec{\mu}$ should be well aligned with the mean molecular dipole. The quantity in parentheses, $\Delta\vec{F}$, is the change in local field upon water-mediated binding of cations and anions to the probe. Such a change in field should be intimately governed by $\vec{F}_{\text{ions}}$ (see derivation section below). Moreover, the red shift can be directly mapped to a density of local field lines (Equation **3-2**), which should increase as the concentration of double-ion bound dipoles increases or when the spacing between ions and the dipole changes.

In order to further explore the accumulation of salts around dipoles, Steve Corcelli's group (Notre Dame, IN) has performed classical MD simulations with acetone and $CaCl_2$ as the force fields for calcium are well established (Figure **3-8** D). We find it most informative to construct cylindrical distribution functions from trajectory snapshots. The transverse axis of the cylinder (Z)

is placed on the vertical axis and the radius of the cylinder (r) is placed on the horizontal one. In this approach, the system is centered around the carbonyl bond, which is oriented along the Z axis. Adding 4 M $CaCl_2$ to these simulations results in a clear ordering of ions around the dipole. Ca^{2+} cations accumulate adjacent to the first hydration shell above the oxygen atom. A small fraction of Cl^- ions are located here as well, which is likely due to formation of $CaCl^+$ ion pairs under 4 M conditions. However, the majority of the Cl^- anions sit underneath the dipole separated from acetone, again, by a layer of water molecules. This can be clarified by plotting the normalized density of each ion (see density profile section below), which reveals that most anions are located at negative Z positions in Figure **3-8** D while most cations are found at positive Z positions. These findings from our MD simulations support the structuring of ions around vibrational probes proposed in Figure **3-8** C. Namely, local ions above the dipole gives rise to a net positive region while those immediately below it gives rise to a net negative region.

Ion Density Profiles Around Acetone in 4 M $CaCl_{2(aq)}$

Results from MD simulations suggest that cations and anions support our suggestion that water-mediated ion binding events of both cations and anions lead to accumulation of these ions around opposite ends of an organic dipole. Here, we decompose the cylindrical distribution profile from above (Figure **3-8** D) into individual components for water, Ca^{2+} and Cl^- (Figure **3-9**).

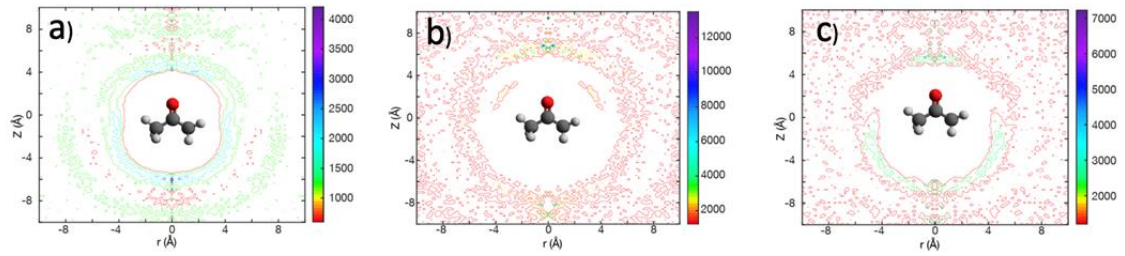

Figure **3-9**: Cylindrical distribution functions of acetone in 4 M $CaCl_2$ decomposed by atom type into (A) waters, (B) calcium ions and (C) chloride ions. Contours are scaled to the probability density as shown by the scale bars to the right of the plots.

Clearly, we can see that Ca^{2+} accumulates around the negative side of the dipole while Cl^- accumulates around the positive terminus. We, also, provide radial distribution functions (g(r)) of water and ions with respect to the carbonyl oxygen (Figure **3-10**).

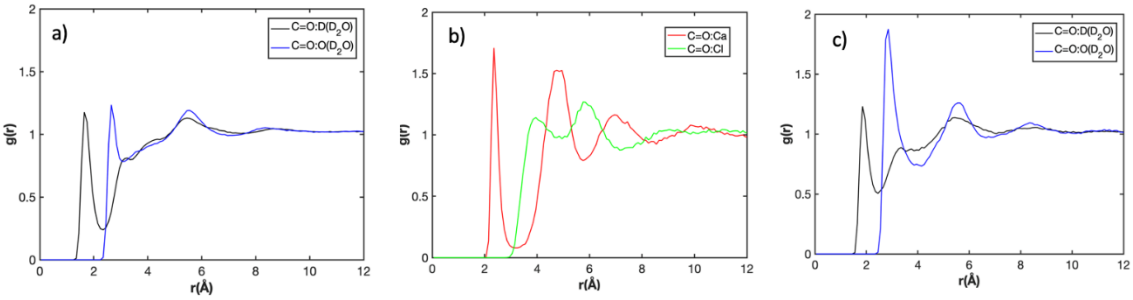

Figure **3-10**: Radial distribution functions from the carbonyl oxygen of acetone to the surrounding solvent in (A) neat D_2O, (B) 4 M $CaCl_2$ (ions) and (C) 4 M $CaCl_2$ (waters).

While the g(r)s provide 1-dimenstional structural information, they lack the ability to report on the locations of the atoms relative to the distance (or height) along the carbonyl bond axis as can be done with cylindrical distributions. Clearly the information provided from the g(r) are not as informative as the information one obtains from Figure **3-8** D and Figure **3-9**.

Electric Field Calculations

Above, we propose the presence of a net local electric field that points from the cation to the anion (Figure **3-8** C). However, an interesting question arises as to whether we can calculate this from our MD simulations. First, we have calculated the electric fields from water and ions which act on the carbonyl bond of acetone in pure water and a solution of 4 M $CaCl_2$ (Figure **3-11**).

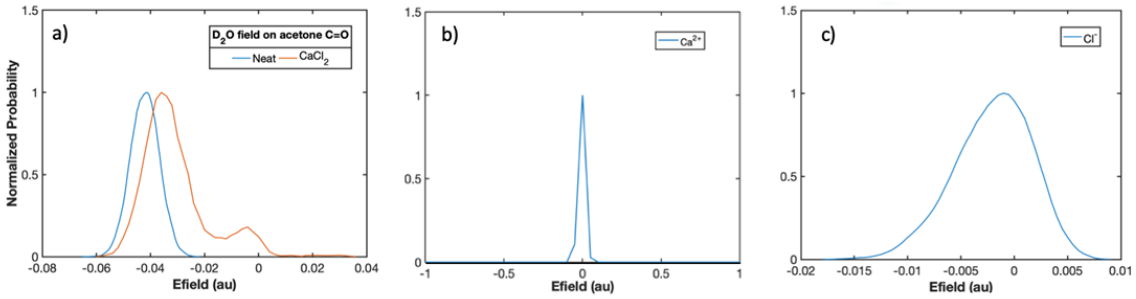

Figure **3-11**: Calculated electric field components of acetone in D_2O and 4 M $CaCl_2$. Panel (A) shows D_2O field on the carbonyl acetone with $CaCl_2$ present (orange) and without (blue). The ion field contributions are shown to be centered around zero in (B) Ca^{2+} and (C) Cl^-.

When the salt is added to solution, weakening in the field from water occurs. This is expected from Onsager's reaction field theory and the drop in the bulk dielectric constant. However, there is also a small field from the ions. These calculations reveal that when one averages over all ions in the simulation box, the resulting field is extremely weak. Importantly, this is not necessarily the most informative approach. Rather, it is likely only the most local of ions which are organized around the first hydration shell that give rise to the small ion-induced red shift. Indeed, vibrational modes are often thought to report on only the most local of effects from a surrounding chemical environment.[115] Averaging over long periods of time to obtain information on the most local of fields would come at a great computational cost and introduce large error. Moreover, the idea that such a small portion of the field is the relevant factor is in line with our observation that

the ion-induced red shifts are extremely small (only a few wavenumbers per mole of added salt). As such, we propose that our library of experimental data presented above is far more informative than the electric field calculations from MD simulations.

Ion-Nitrile Interactions in Aqueous Solution

The large library of data collected in this work (Figure **3-6**, Figure **3-8** and Appendix B) demonstrates that there are several different types of ion-dipole interactions. One type of interaction gives rise to a blue-shifted shoulder that coexists with the initial (hydrated) mode on the vibrational timescale. This makes since because the off rate of the cation should be far longer that femtoseconds, and as such both bound and unbound populations of probe molecules can be resolved in vibrational spectra. This holds for probes binding events which give rise to covalent modification *via* disruption to hydrogen bonding with water. However, population of the water-mediated sites above and below the dipole give rise to a Stark shift in the hydrated mode as the density of field lines, on average, increases as ions bind with increasing salt concentration. Such a uniform shift in the mode, as opposed to a second shoulder, is indeed what one would expect from a Stark effect mechanism.

While the shoulder has been well studied in the case of carbonyl bonds, it has not received attention in the case of nitrile probes. Here we explore this type interaction by starting with the solvatochromic series for acetonitrile and then adding salt (Figure **3-12** A).

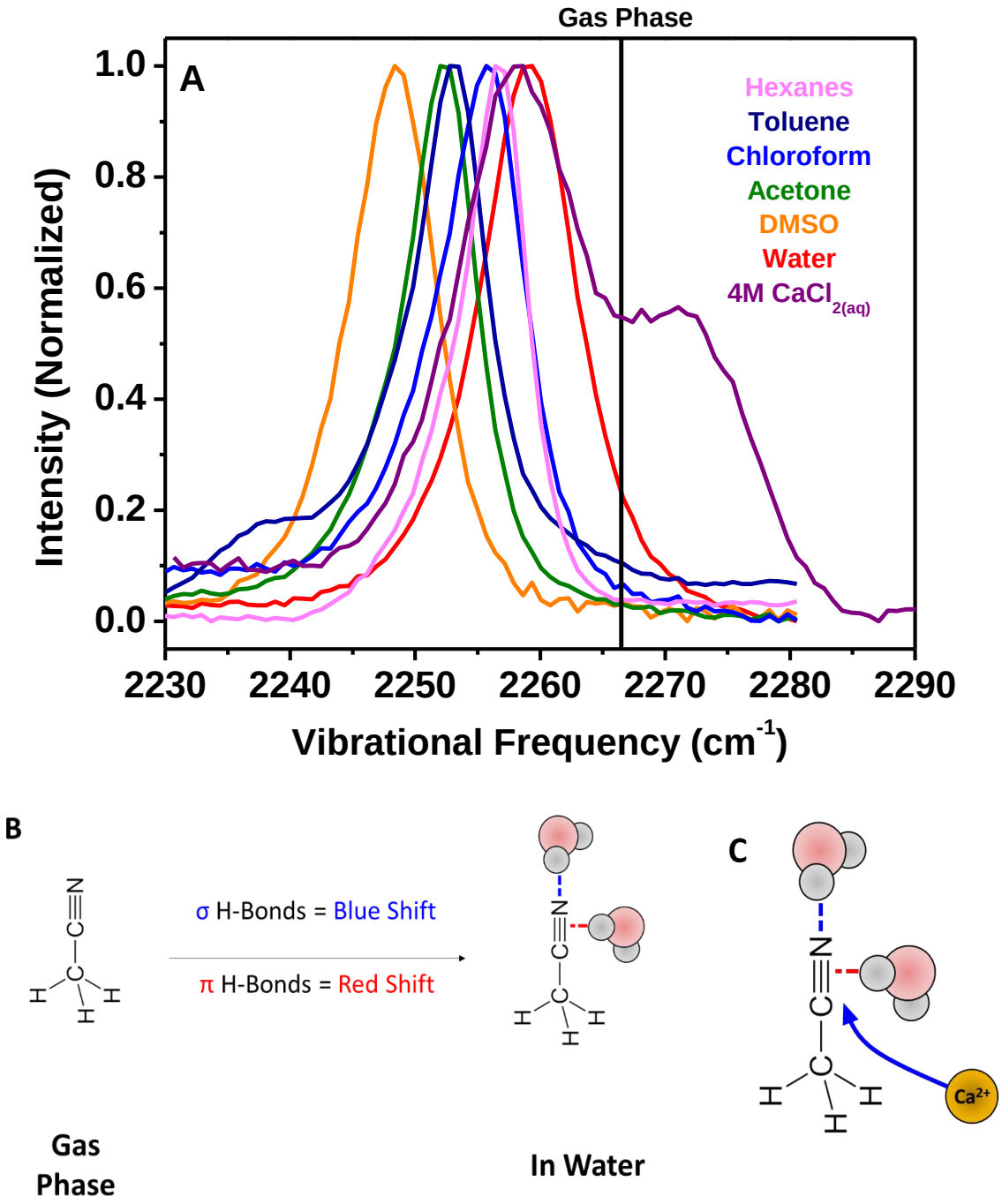

Figure **3-12**: (A) Vibrational spectra of acetonitrile in a series of organic solvents, water and a solution of 4 M $CaCl_2$. The gas phase frequency is marked with a vertical black line.[121] The concentration of acetonitrile was 100 mM. (B) A schematic depicting hydrogen bonding with nitriles. (C) A schematic depicting that dehydration of nitriles occur *via* a cation-pi interaction. The disruption of the pi-hydrogen bond by the cation that gives rise to a blue shift is denoted by a blue arrow.

Upon immersing acetonitrile form the gas phase into hexanes, there is a red shift observed in the vibrational frequency. As the polarity of the solvent is increased, the mode red shifts ever more in accordance with the qualitative prediction from Onsager's reaction field theory. However, upon immersing the probe into water, the frequency displays a net blue shift relative to the frequency observed in DMSO solvent. It has been argued that hydrogen bonding between water and the nitrile group gives rise to this blue shift. Specifically, the lone pair on the nitrogen has slight anti-bonding character and charge transfer through the hydrogen bond, therefore, strengthens the bond.[100]

While the lone pair has anti-bonding character, this is not the only factor to consider. In fact, it has been suggested that the pi-hydrogen bond the forms perpendicular to the dipole removes electron density from bonding orbitals in the triple bond.[122] As such, hydrogen bonding with acetonitrile is expected to impart a convolution of blue-shifted and red-shifted contributions (Figure **3-12** B). This is important for the next set of experiments we performed using salt. We added 4 M $CaCl_2$ to solutions containing acetone and observed a small red shift in the hydrated mode and a pronounced shoulder on the high frequency side of the CN resonance. Moreover, the frequency of the shoulder is higher in frequency than that observed in the gas phase. This is most consistent with Ca^{2+} binding from the side to displace the pi-hydrogen bond (Figure **3-12** C). Indeed, if such an interaction is present in solution then one expects to observe a blue-shifted shoulder instead of a red-shifted shoulder, despite the net blue shift observed when switching from DMSO to water. Moreover, such a cation-pi interaction should not displace the hydrogen bond with the nitrogen lone pair. As such, it is conceivable that the blue-shifted shoulder can be pulled above the gas phase frequency.

Next, we surveyed our library of vibrational spectra (see Appendix B) in order to determine the nature underlying the different types of ion-nitrile interactions. Evidence for cation-pi interactions are present in solutions containing $CaCl_2$, $SrCl_2$, LiCl and NaCl. When one carefully

considers spectra of acetonitrile in the presence of $MgCl_2$, there is no evidence for formation of a cation-pi interaction or a Stark shift. However, the peak does broaden symmetrically as a function of salt concentration. At first glance, this may appear to be what happens with NaCl as well, but careful examination reveals that broadening is not symmetric with NaCl as it is with $MgCl_2$. As such, broadening and blue-shoulders should be carefully distinguished from one another. Moreover, evidence has been presented previously to suggest that broadening in the nitrile band can suggest alteration to number of hydrogen bonds with water.[123] As such, we believe the broadening of the nitrile stretch by $MgCl_2$, or any salt, is evidence for a third type of binding event. This can be clearly studied with $MgCl_2$ due to the lack of a Stark shift and cation-pi interactions. In fact, the lack of a Stark shift suggests that the net electric field is perpendicular to the bond dipole which indicates the Mg^{2+} cation approaches the nitrile from the side. However, this cation simply forms a water-separated interaction perpendicular to the bond dipole which modulates the pi-hydogen bond with water. We summarize this below with a schematic that depicts the three types of binding sites using $CaCl_2$, $MgCl_2$ and CsCl as these salts give rise to the most pronounced pieces of evidence for each of the three binding sites (Figure **3-13**).

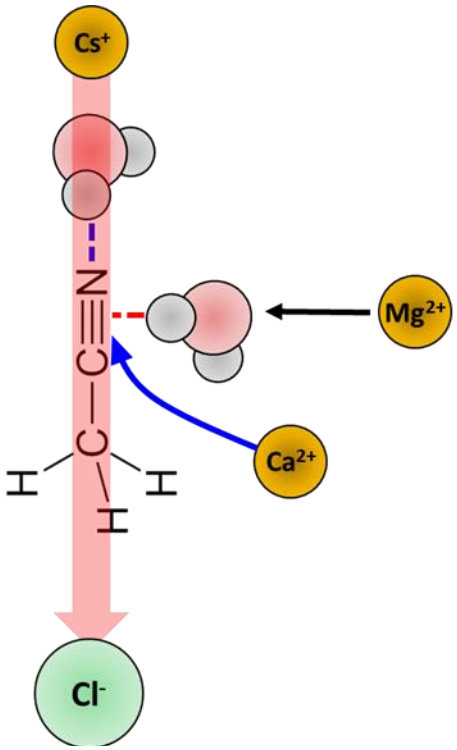

Figure **3-13**: Schematic depicting three possible binding sites for salts around nitrile probes.

The first binding site is assigned to a cation-pi interaction which results in a blue-shifted shoulder in the vibrational spectrum. The second site is assigned to a water-separated cation-pi interaction which symmetrically broadens the C≡N resonance. The third binding site is assigned to a water-separated population of cations and anions that results in a net electric field parallel to the bond dipole. For clarity, it is not these three salts that populate the respective binding sites. Moreover, a salt can populate multiple of these sites in the same solution as evidenced by $CaCl_2$ which gives rise to both a blue-shifted shoulder and a Stark shift. It should be emphasized that the trend which is analogous to the LMWA mentioned above applies to population of the water-separated site depicted for CsCl in Figure **3-13**. As that trend claims, salts possessing well-hydrated cations will populate water-separated sites with carbonyls while poorly-hydrated ones will populate these sites with nitriles. Now we can specify that this LMWA claim applies to colinear interactions

which Stark shift the bond, and not necessarily the cation-pi interaction or contact pairs with carbonyls.

Derivation of Frequency-Field Relationships in Salt Solutions

Equation **3-2** above details the relation between a change in local electric field and a Stark shift in the vibrational spectrum. This relationship is known to hold in pure dielectric liquids. Here we derive the relationship in a solution containing salt. First, we depict the vibrational landscape of the probe (Figure **3-14**).

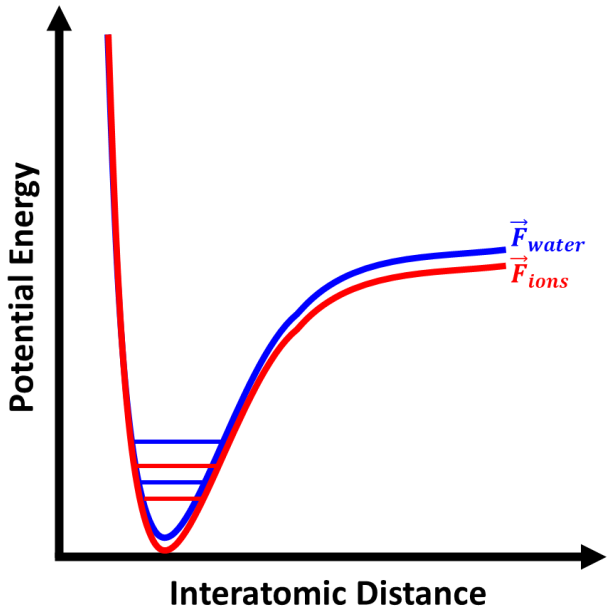

Figure **3-14**: The anharmonic vibrational well for the bond dipole of a chromophore that undergoes a Stark shift due to water-separated ions which impart a net electric field $\vec{F}_{ions}$ pointing from the cation to the anion (red). This shifts the frequency to lower values than found in the presence of water electric field lines $\vec{F}_{water}$ (blue) as indicated in Figure **3-8**. The two lines in each potential well represent the ground and first excited vibrational energy levels.

We start by pointing out that in the case of a stabilizing Stark shift (i.e. a Stark shift to lower frequency), the excited state is lowered more than the ground state due to the greater dipole

moment in the excited state which interacts more strongly with the electric field. As such, we have to define the energy for each of the four vibrational energy levels by the traditional representation for dipole-field coupling:

$$U_{0,i} = -\vec{\mu}_{0,i} \cdot \vec{F}_i \qquad \text{Equation } \mathbf{3\text{-}3}$$

$$U_{1,i} = -\vec{\mu}_{1,i} \cdot \vec{F}_i \qquad \text{Equation } \mathbf{3\text{-}4}$$

Where *U* denotes the energy of a dipole, the subscripts *0* and *1* denote the ground and excited states, respectively, and the subscript *i* denotes either the water or salt environment. Thus, the vibrational transition frequency in the i^{th} environment, $\bar{\nu}_i$, is given by the Plank-Einstein postulate:

$$\Delta U_{0-1,i} = E_{photon} = hc\bar{\nu}_i \qquad \text{Equation } \mathbf{3\text{-}5}$$

As such, the transition frequency, which has been shifted from the gas phase value to the one observes in a condensed phase system, is given by:

$$hc\bar{\nu}_i = \left(-\vec{\mu}_{1,i} \cdot \vec{F}_i\right) - \left(-\vec{\mu}_{0,i} \cdot \vec{F}_i\right) = -\left(\vec{\mu}_{1,i} - \vec{\mu}_{0,i}\right) \cdot \vec{F}_i = -\Delta\vec{\mu}_i \cdot \vec{F}_i \qquad \text{Equation } \mathbf{3\text{-}6}$$

This is the expression for the linear Stark effect where the transition frequency depends linearly on the local field and the slope is called the Stark tunning rate ($\Delta\vec{\mu}_i$). As $\vec{F}_i \rightarrow 0$, the frequency approaches that observed in the gas phase which results in:

$$hc\bar{\nu}_i = -\Delta\vec{\mu}_i \cdot \vec{F}_i + hc\bar{\nu}_{gas\ phase} \qquad \text{Equation } \mathbf{3\text{-}7}$$

Now, when one adds salt to pure water the change in the transition frequency shown in Figure **3-14** is given by:

$$\Delta\Delta U_{0-1,salt-pure\ water} = hc\Delta\bar{\nu}_{salt-pure\ water} = \left(-\Delta\vec{\mu}_{salt} \cdot \vec{F}_{salt} + hc\bar{\nu}_{gas\ phase}\right) - \left(-\Delta\vec{\mu}_{pure\ water} \cdot \vec{F}_{pure\ water} + hc\bar{\nu}_{gas\ phase}\right) \qquad \text{Equation } \mathbf{3\text{-}8}$$

Figure **3-4** shows that the anharmonicity of the probe is conserved upon switching from pure water to a salt solution. As such:

$$\Delta\vec{\mu}_{salt} = \Delta\vec{\mu}_{pure\ water} \equiv \Delta\vec{\mu} \qquad \text{Equation } \mathbf{3\text{-}9}$$

Substituting Equation **3-9** into Equation **3-8** gives:

$$hc\Delta\bar{\nu}_{salt} = -\Delta\vec{\mu}\cdot\left(\vec{F}_{salt} - \vec{F}_{pure\ water}\right) = -\Delta\vec{\mu}\cdot\Delta\vec{F} \qquad \text{Equation } \mathbf{3\text{-}10}$$

Where $\Delta\bar{\nu}_{salt}$ has been used as an abbreviation for $\Delta\bar{\nu}_{salt-pure\ water}$, and is equal to the shift in frequency caused by the change $\Delta\vec{F}$ which results from the addition of salt to water. Equation **3-10** is the same as Equation **3-2** above. Above we argue that the dominate contribution to $\vec{F}_{salt}$ is $\vec{F}_{ions}$. $\vec{F}_{salt}$ represents the total field projected along the bond that one would calculate in an MD simulation that arises from all water molecules and ions in the salt solution, and $\vec{F}_{ions}$ represents the local field that is governed by the ions which reside adjacent to the first hydration shell above and below the dipole. As such, $\Delta\vec{F}$ is dominated by $\vec{F}_{ions}$ due to the local sensitivity of molecular probes.

The Influence of Salt on the Optical Properties of PRODAN

Since ions can readily shift the frequency of vibrational probes, an interesting question arises as to whether such an effect is present in fluorescence spectra of visible dyes. To test this, we added $MgCl_2$ to solutions containing an optical dye, PRODAN, which is known to be highly sensitive to the solvent polarity (Figure **3-15**).[124,125]

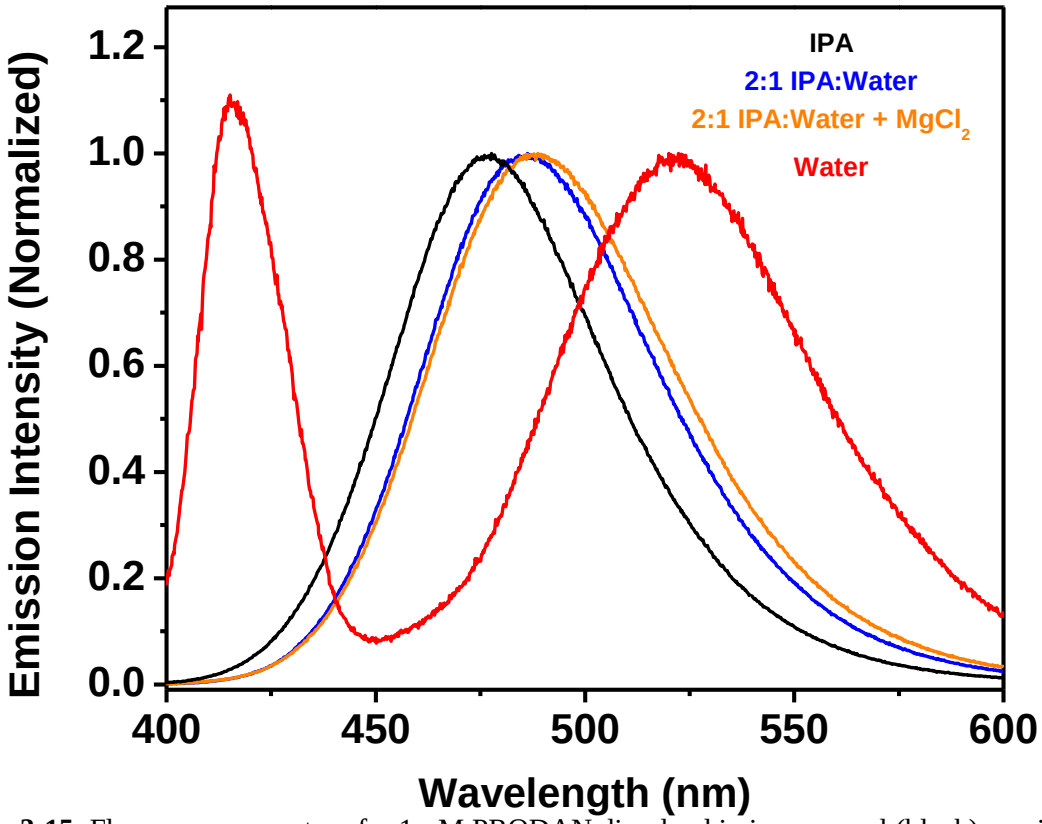

Figure **3-15**: Fluorescence spectra of ~ 1 µM PRODAN dissolved in isopropanol (black), a mixed solvent 2:1 by mol ratio isopropanol : water (blue), a mixed solvent 2:1 by mol ratio isopropanol : water with added $MgCl_2$ (yellow) and pure water (red). The excitation wavelength was 367 nm. The fluorimeter was blanked to the solvent of each solution.

PRODAN is only sparingly soluble in water. In fact, addition of salt to aqueous solutions of PRODAN led to precipitation of the dye. As such, we employed a mixed solvent system composed of isopropanol (IPA) and water to study the effects of salts on optical properties of this dye. The solution containing salt was prepared by mixing an aqueous solution of 100 mM $MgCl_2$ with IPA. Based on the volumes used to prepare this mixed solvent, the apparent concentration of $MgCl_2$ in solution was ~ 10 mM.

When one switches from IPA to 2:1 IPA : water, the emission profile red shifts from 477 nm to 486 nm. Upon switching to water there is an even greater red shift to 522 nm. There is a second mode at 416 nm which has been observed previously, and represents a population of

PRODAN molecules that are hydrated differently than monomeric PRODAN.[126] The solvatochromic shift with increasing solvent polarity is expected due to Onsager's reaction field theory. As such, it is surprising that the solution containing $MgCl_2$ (yellow) is slightly red shifted from the one which does not (blue). We conclude local ion effects shift the emission profile of visible dyes as was concluded for vibrational probes.

Above we present fluorescence data of PRODAN dissolved in a mixed solvent solution containing $MgCl_2$. The emission profile red shifts in the presence of even small amounts of salt (~ 10 mM). Below we examine the effects of this salt addition on the electric absorption spectrum (Figure **3-16**).

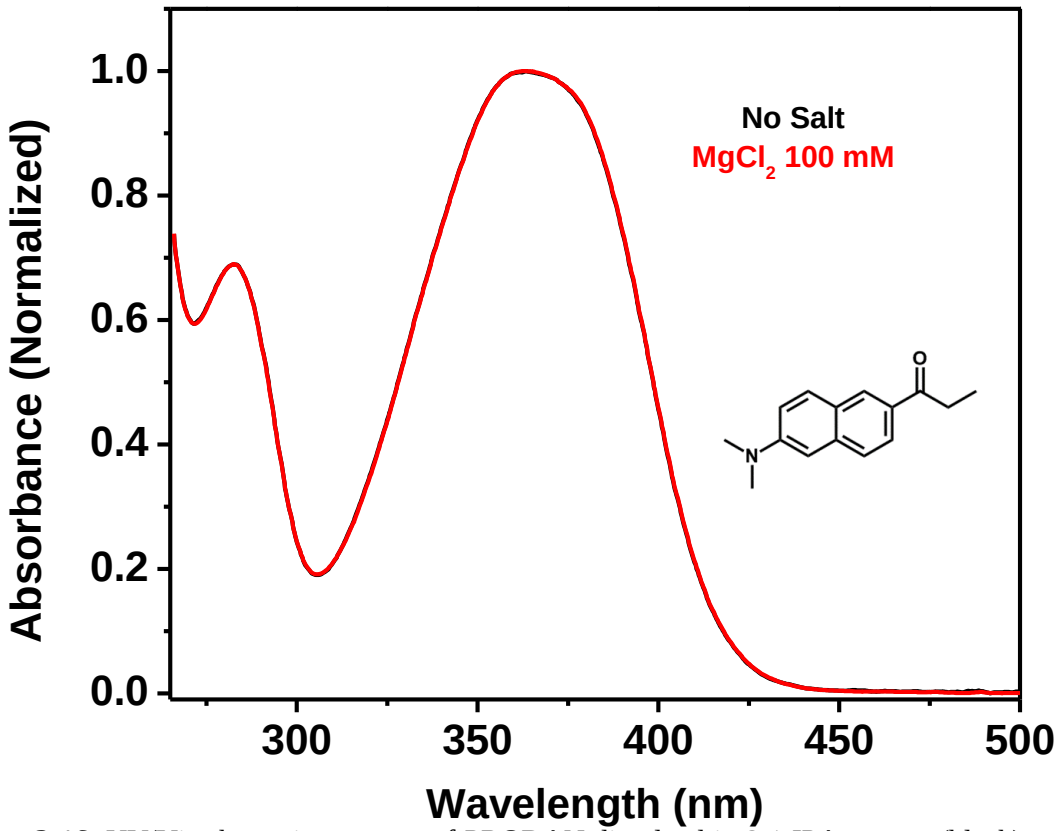

Figure **3-16**: UV/Vis absorption spectra of PRODAN dissolved in 2:1 IPA : water (black) or 2:1 IPA : 100 mM $MgCl_{2(aq)}$. The apparent concentration of salt was ~ 10 mM as mentioned in the text. The spectrometer was blanked to the solvent for each solution. This chemical structure of PRODAN is also provided.

Upon changing the bulk solvent, the UV/Vis spectrum of PRODAN is known to red shift with increasing solvent polarity due to the standard mechanism.[124-126] In the case of salt addition, the fluorescence spectrum red shifts (Figure **3-15**) but the absorption spectrum does not as is shown here. This indicates that the ions preferentially interact with the first excited singlet state. This makes since because the difference in dipole moment between the ground and first excited singlet bands for this dye is very large (~ 5 Debye).[126]

Conclusions

In conclusion, we have found that Stark shifts of vibrational chromophores can be disentangled from frequency shifts that arise from covalent modifications in solutions containing salt. Covalent modification primarily occurs due to modulation of hydrogen bonding with water by the presence of ions in the first hydration shell, while a Stark shift will arise from through space electric fields generated by water-separated ions. The latter class of interactions follow a Hofmeister series that depends on the identity of both the salt and the probe. Specifically, well-hydrated cations like Mg^{2+} and Li^{+} shift carbonyls the most while poorly-hydrated cations like Cs^{+} have the biggest impact on nitriles. However, both nitriles and carbonyl probes follow a direct Hofmeister series in the anion in which I^{-} interacts better with the dipole than Cl^{-}. The dependence on the cation, anion and probe identity reveals that only the most local of ions give rise to a net electric field which points from cation to anion to Stark shift the vibrational resonance. This mechanism is best described as arising from ion binding in water-separated motifs, which is fundamentally different from arguing that intrinsic properties of the ions dissolved in the bulk solution can predict an ion-specific Stark shift. This is highlighted by the fact that highly charge dense Mg^{2+} cations Stark shift ketones and amides substantially while having no effect on the

frequency of acetonitrile at all. In fact, it is not the total electric field from water and ions in the electrolyte that governs Onsager's model in a salt solution, but rather it is the local field that arises from water-separated and ion-specific binding to the probe. Importantly, this also seems to apply to visible dyes such as PRODAN. In fact, our experiments with this dye demonstrate that dyes used to detect changes in a chemical environment at the molecular-level are susceptible to the 'anti-Onsager' effect.

Chapter 4

THE IMPACT OF CATION BINDING ON ELECTRONIC STRUCTURE OF CARBONYL AND PEPTIDE BONDS IN AQUEOUS SOLUTION

Herein, we comment on the interpretation of spectroscopic data in "Arresting an Unusual Amide Tautomer Using Divalent Cations", *J. Phys. Chem. B* **2019**, *123* (40), 8419–8424, by Bagchi and coworkers.[127] In their paper, the authors assign the appearance of a blue-shifted shoulder on the amide I vibration of *N*-methylacetamide (NMA), *N*, *N*-dimethylacetamide (DMA), and urea to the formation of a tautomer-like structure in the presence of divalent metal cations. In other words, the shoulder should originate from a $C{=}N^+$ resonance that is stabilized by the presence of divalent metal cations. This is shown schematically in Figure **4-1**. Moreover, Bagchi and coworkers argue that the $C{=}N^+$ resonance is coincidently located at a position just to the blue of the amide I band upon the introduction of divalent metal cation salts. This assignment represents an alternative to the idea that the blue-shifted shoulder on the amide I band arises from the dehydration of the amide oxygen upon interaction with metal cations.[31,120]

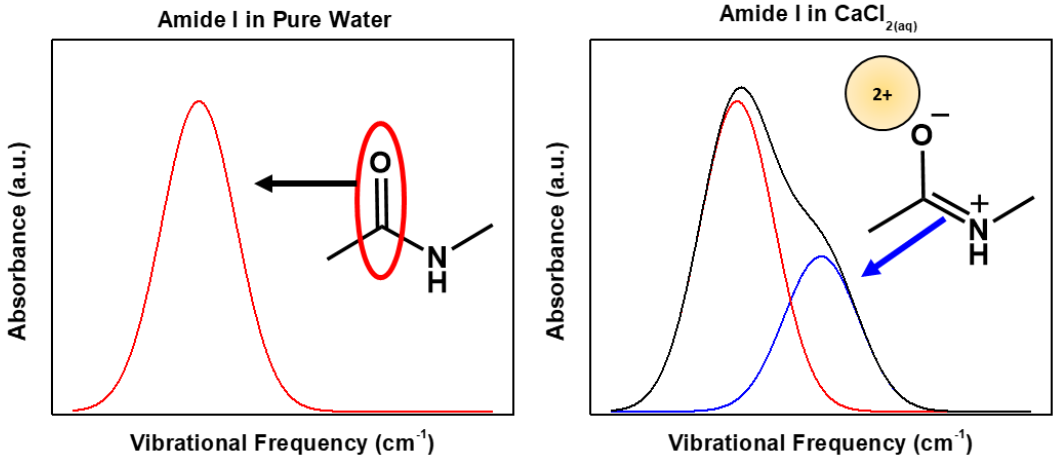

Figure **4-1**: Schematic of an alternative assignment for the blue shoulder on Amide I resonances upon the introduction of metal cations such as Ca^{2+}. In this case, the blue-shifted shoulder is argued to arise from a $C{=}N^{+}$ bond instead of a dehydrated C=O bond.

Bagchi's putative new assignment can be directly tested by studying ^{15}N isotope labeled NMA. Such experiments were performed in our laboratory and are described below.

The Blue Shoulder is not a Tautomer

In a first set of experiments, Elizabeth Elacqua's group (State College, PA) synthesized NMA and ^{15}N-labeled NMA by reacting acetyl chloride with methylamine·HCl and ^{15}N-labeled methylamine·HCl, respectively. Our reaction scheme is shown below (Figure **4-2)**.

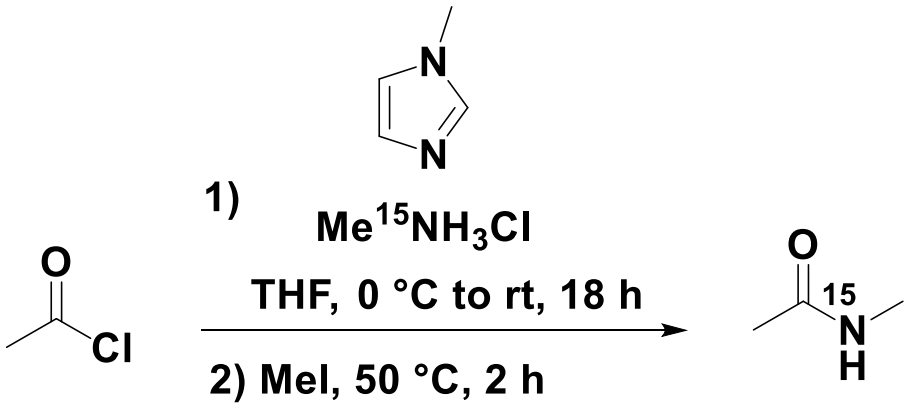

Figure **4-2**: Synthesis of ^{15}N-methylacetamide. ^{15}N-methylamine hydrochloride was purchased from Cambridge Isotope Laboratories, acetyl chloride was purchased from Acros Organics, 1-methylimidazole was purchased from Millipore Sigma, and methyl iodide was purchased from Bean Town Chemical.

^{15}N-methylamine hydrochloride (0.637 g; 9.30 mmol; 1.12 eq) and 1-methylimidazole (1.80 mL; 22.6 mmol; 2.73 eq) were added to a 100 mL flame-dried round bottom flask containing 20 mL anhydrous THF. This was gently stirred and cooled to 0°. Acetyl chloride (0.590 mL; 8.27 mmol; 1.00 eq) was added dropwise, forming a white solid. The flask was sealed and allowed to slowly warm to room temperature while continuing to stir for 18 hours. Upon completion, THF was evaporated off and methyl iodide (9.0 mL; 145 mmol; 17.5 eq) was added and the reaction was heated to 50°C for 2 hours. The solution was then cooled to room temperature and methyl iodide was evaporated to give a yellow oil. This was carefully washed with diethyl ether and decanted off over many sequences. The oil was also dissolved in 1 mL methanol and then precipitated with diethyl ether and decanted to further isolate product. The diethyl ether was evaporated and the resulting residue was filtered through a thin pad of celite and basic alumina to remove any acetic acid and diethyl ether was evaporated to yield 0.080 g of ^{15}N-methylacetamide as a pale-yellow oil/crystalline solid (1.08 mmol; 12 %).

The synthesized compound was characterized with ^{1}H nuclear magnetic resonance (NMR), ^{13}C NMR and mass spectrometry. These data are shown in Figure **4-3**, Figure **4-4** and Figure **4-5**, respectively.

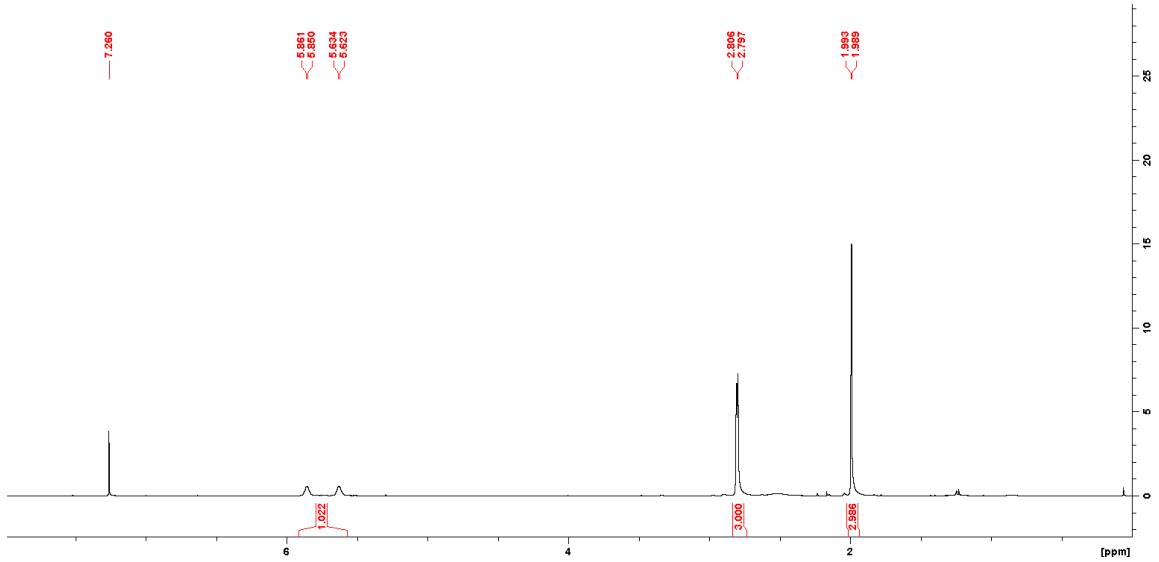

Figure **4-3**: ^{1}H NMR (400 MHz, $CDCl_3$) of *^{15}N*-NMA.

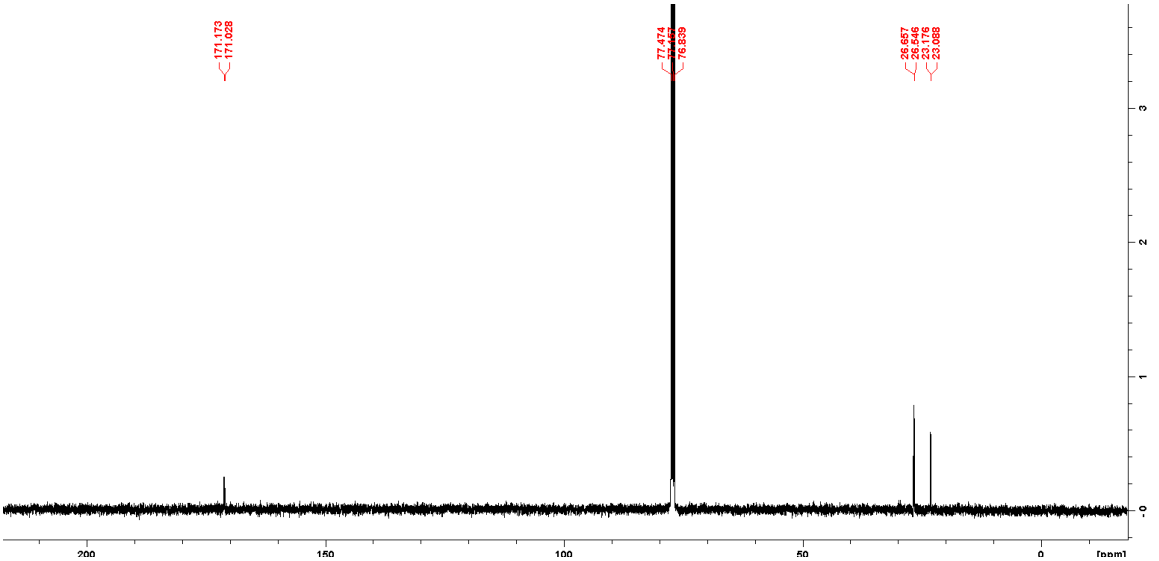

Figure **4-4**: ^{13}C NMR (100 MHz, $CDCl_3$) of *^{15}N*-NMA.

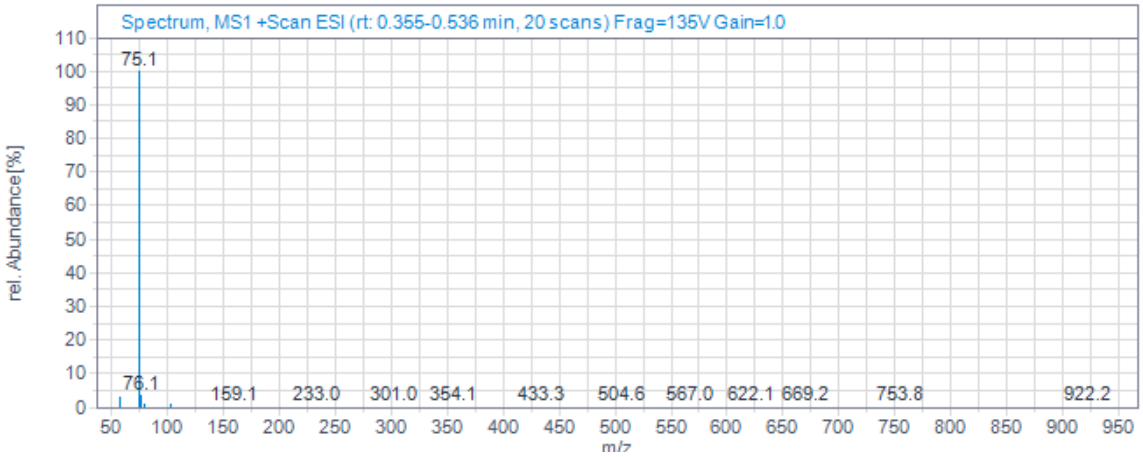

Figure **4-5**: LC-MS of ^{15}N-NMA: $[M+H^+]$ = 75.1.

The resulting amide-containing molecules were introduced into D_2O at a concentration of 100 mM. This is shown below (Figure **4-6** A).

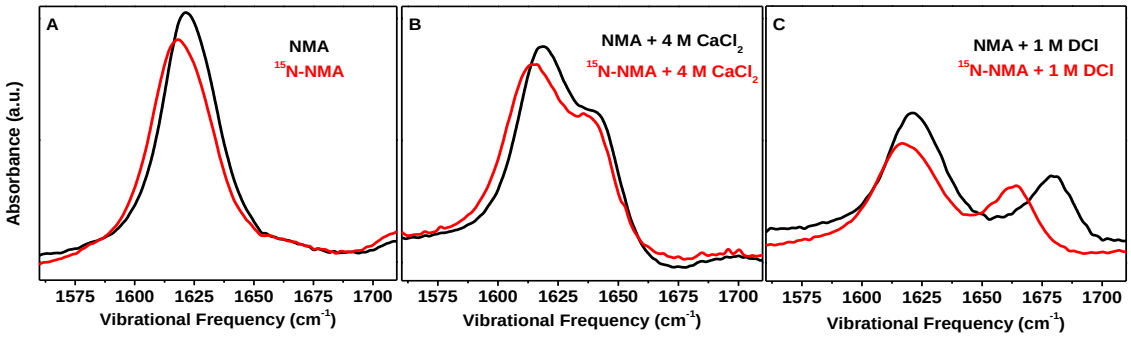

Figure **4-6**: ATR-FTIR absorption spectra of the amide I resonance for solutions containing 0.1 M NMA and 0.1 M ^{15}N-labeled NMA. All solutions were prepared in D_2O. (A) The amide I resonances of NMA and ^{15}N- labeled NMA in D_2O, respectively. (B) The same molecules in the presence of 4 M $CaCl_2$ and (C) upon the addition of 1 M DCl. The IR instrument which was used to collect this data was described in Chapter 2 because the ATR window had to withstand exposure to concentrated acid.

In the absence of salt, there is a small isotope shift upon substitution with the ^{15}N-labeled molecule. This very modest red shift from 1620 cm^{-1} to 1617 cm^{-1} in the case of ^{15}N-labeled NMA is expected because the amide I resonance is not purely C=O in character. Upon adding 4 M $CaCl_2$,

a blue-shifted shoulder appears at 1645 cm^{-1} with NMA as well as with ^{15}N-labeled NMA (Figure **4-6** B). This is not what one would expect if the blue shoulder was from $C=N^+$. Indeed, if the $C=N^+$ assignment was correct, then this mode should have been quite sensitive to the mass of the nitrogen atom. Moreover, one can look for an isotope shift upon the addition of acid to solution. We added 1 M DCl to solution to directly examine this feature (Figure **4-6** C). In the case of NMA, a new peak appears at 1680 cm^{-1} (Figure **4-6** C, black curve). Next, the same experiment was performed with a solution containing ^{15}N-labeled NMA (Figure **4-6** C, red curve). In this case, the new mode red shifts down to 1663 cm^{-1}. These observations confirm that the peak at 1680 cm^{-1} arises from a CN bond while demonstrating that the one at 1645 cm^{-1} does not.

The current results are consistent with previous assignments of the blue-shifted shoulder to the dehydration of the carbonyl oxygen atom when divalent metal cations are present.[31,120] Indeed, in the absence of $CaCl_2$, there should be a small amount of charge transfer to the σ^* orbital of the water, which red-shifts the amide I resonance.[112] When the hydration shell is disrupted by metal ions, the peak is expected to blue shift part way back toward its gas phase frequency. While the above results disprove the idea that the blue-shifted shoulder in the amide I spectra in Figure 1B come from a $C=N^+$ resonance, they do not mean that tautomerization cannot occur when salt is introduced. In fact, a recent study has shown that a trace amount of this structure can be formed, but only in the presence of 6 M $CaCl_2$ and in that case the peak is also at 1680 cm^{-1}.[128]

Finally, we have measured the vibrational spectrum of acetone in the presence and absence of 4 M $CaCl_2$. This data is shown below (Figure **4-7)**.

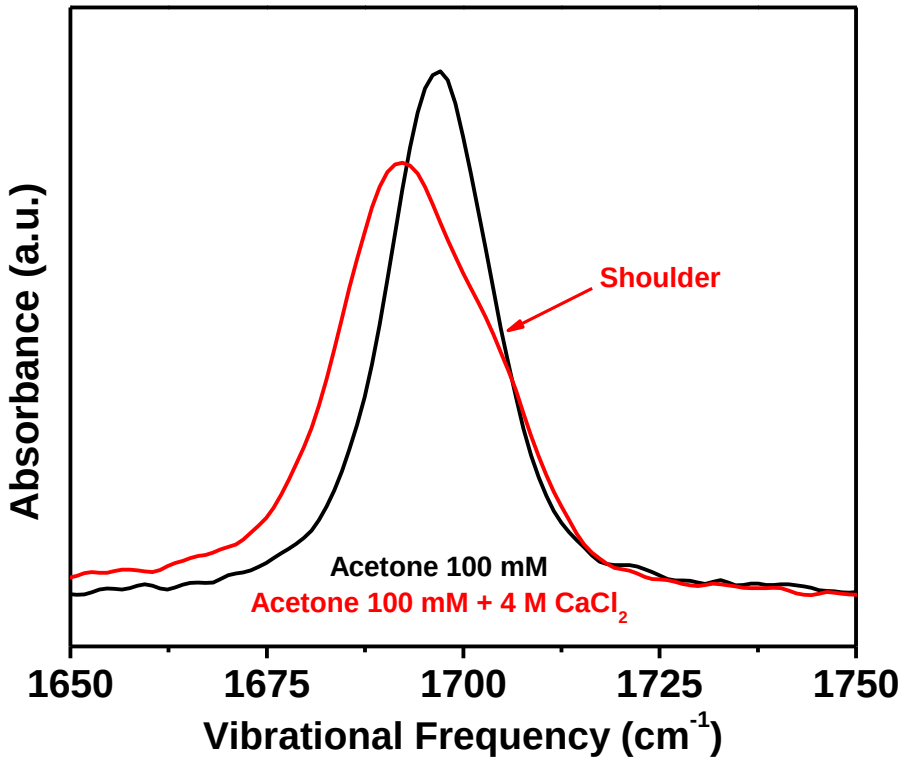

Figure **4-7**: Absorption spectra of the C=O stretch resonance of acetone in the presence and absence of 4 M $CaCl_2$. Both solutions were prepared in D_2O. The acetone concentration was 0.1 M. The blue-shifted shoulder is denoted by an arrow.

As can be seen, a shoulder similar to the one in Figure **4-6** B appears, albeit somewhat less pronounced. As such, a CN resonance is not required for this observation. This is significant, because acetone cannot tautomerize. Curiously, Bagchi and coworkers provide spectra for acetone in the presence of $CaCl_2$ in Figure S2 of their manuscript. The authors claim that these spectra serve as controls to demonstrate that the blue-shifted shoulder is specific to amide-containing molecules. Nevertheless, it is straightforward to demonstrate that such shoulders can also occur with simple ketones such as acetone.

Conclusions

In conclusion, we have demonstrated that formation of a blue-shifted shoulder (at ~ 1645 cm^{-1}) in amide I spectra does not result from tautomer formation. In fact, the C=N resonance of a tautomer is found at yet a higher frequency (~ 1680 cm^{-1}). This has been verified by changing the nitrogen isotope. Specifically, the blue shoulder is not sensitive to the isotope change, which rules out assignment to either a $C=N^+$ or fermi resonance. Moreover, a CN bond is not required to observe the shoulder as demonstrated with acetone. The shoulder is well overlapped with the initial (hydrated) peak in acetone spectra whereas it is better separated in frequency from the initial peak in spectra of NMA. This difference stems from a difference in the electronic structure of the carbonyl bond due to resonance with the nitrogen lone pair. Specifically, the dipole moment of the carbonyl is larger in NMA. This results in a weaker bond, and the change in vibrational frequency upon disruption to the hydrogen bond with water by contact pair formation in NMA should be more pronounced. Indeed, the shoulder found in NMA (1645 cm^{-1}, Figure **4-6** B; black curve) is blue-shifted ~ 25 cm^{-1} from the frequency observed in the absence of salt (1620 cm^{-1}, Figure **4-6** A; black curve). However, the shoulder in acetone is only 5-10 cm^{-1} blue-shifted from the frequency observed in the absence of salt (1697 cm^{-1}, Figure **4-7**). Finally, previous studies have observed blue shifts and shoulders in phosphate and carboxylate resonances as a result of ion pairing. As such, our acetone data are clearly complimented by a diverse set of functional groups all of which show blue shifts due to ion binding are not limited to amide resonances.

Chapter 5

HYDRATION OF HOFMEISTER AND IRVING-WILLIAMS METAL CATIONS IN AQUEOUS SOLUTION

Metal cations are important for numerous processes that occur in water. Studies of specific ion effects have often focused on cations from the Hofmeister series including Na^+, K^+, Mg^{2+} and Ca^{2+}.[4,31,120,129-137] However, transition metal cations from the Irving-Williams series behave differently from Hofmeister cations. Some Hofmeister studies have also looked at specific ion effects of transition metal ions.[138-142] Such studies have not usually considered how differences in electronic structure of the cation contribute to ion specificity. For example, in the hydrated and unbound state of free Ni^{2+}, there is likely charge transfer between first hydration shell water lone pairs and unfilled d-orbitals on the metal ion that is not present in the hydration shell of ions like Ca^{2+}.[143-145] As such, the Hofmeister and Irving-Williams series should have fundamentally different driving forces governing ion selectivity due to the differences in cation-water interactions that must be overcome for dehydration, and thus ion binding, to occur in bulk solutions and at interfaces.

When one forms a dilute NaCl solution there is a significant difference between cation-water and anion-water interactions. While hydration shells around both ions are detectible by neutron scattering measurements, the vibrational spectra of first hydration shell water O-H stretching modes do not show comparable contributions from the cation and anion.[37] Chloride anions transfer a small amount of electron density to antibonding orbitals on the water molecule. This is exemplified by the well-known charge transfer to solvent transition in UV/Vis spectra taken of aqueous solutions containing I^-. Importantly, the Na^+ cation cannot accept electron density from the water lone pair. In fact, previously measured vibrational hydration shell spectra of solutions containing select Hofmeister metal cation chloride salts have suggested negligible impact from the

Na^+ cation on the first shell in comparison to Cl^-. However, this is not expected to be true for cations of the Irving-Williams series such as Mn^{2+} and Ni^{2+}. These cations possess unfilled d-orbitals that are capable of accepting electron density from water lone pairs. Moreover, an interesting question arises as to whether Zn^{2+} cations do this despite having a d^{10} configuration.

Herein, we study the first hydration shell around metal cations in aqueous solution when accompanied by Cl^- counter anions with vibrational hydration shell spectroscopy. Raman Multivariant Curve Resolution (Raman-MCR) is applied to the O-H stretching region for a series of salt solutions containing LiCl, NaCl, KCl, RbCl, CsCl, $MgCl_2$, $CaCl_2$ or $SrCl_2$. Such spectra reveal that Cl^- hydration dominates the Raman-MCR spectrum of solutions containing these salts. However, Li^+, Mg^{2+} and Ca^{2+} each give rise to a small signature at lower frequencies in the spectrum as well. This observation points to unique vibrational frequencies for Cl^- and metal cation hydration waters, in addition to cation-specific effects. Moreover, infrared (IR)-MCR spectra reveal a unique effect for divalent hydration shells when $MnCl_2$, $NiCl_2$ or $ZnCl_2$ are added to solution. All three transition metal cations perturb the O-H stretch IR spectrum more than the Cl^- counter anion. As such, these cations perturb the hydration shell differently than Hofmeister cations, which do not enhance the water intensity more than Cl^-. These observations point to the presence of charge transfer in hydration shells of Irving-Williams cations even in the case of Zn^{2+} that is absent for Hofmeister cations.

Hydration of Hofmeister Metal Cations

All samples were prepared immediately before use. All materials were used as received. All salts were bought commercially from Sigma-Aldrich (St. Louis, MO) with purities of > 99.5%. All water (18.2 MΩ·cm) was produced from a Barnstead Nanopure Water System S5 (Thermo

Fisher). All stock salt solutions were prepared to a concentration of 2 M and diluted to a working condition of 1 M. This was repeated three times for each salt.

Unpolarized Raman spectra were collected on a home-built backscattering setup as described in Chapter 2. All experimental Fourier transform (FT) IR spectra, which are presented in the next section and Appendix C, were collected on a commercial spectrometer described in Chapter 3. All MCR data was produced with software provided by Dor Ben-Amotz and operated in Igor Pro® as described in Chapter 2 and the introduction. Pure water was used as a reference for every salt solution.

In a first set of experiments, we measured Raman-MCR spectra of salt solutions containing Hofmeister cations with Cl^- counter anions. These spectra are shown below (Figure **5-1)**.

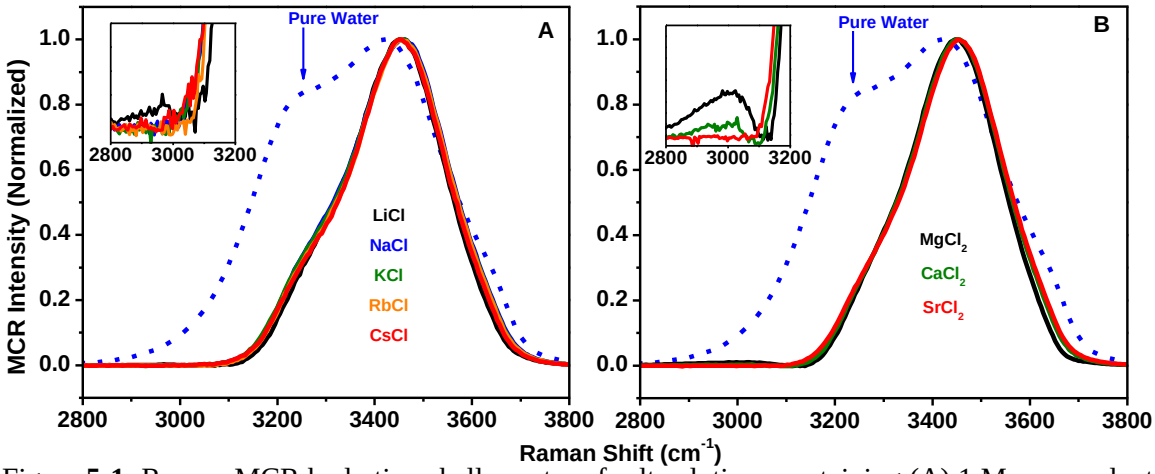

Figure **5-1**: Raman-MCR hydration shell spectra of salt solutions containing (A) 1 M monovalent or (B) 1 M divalent Hofmeister metal cations. Pure water spectra are provided as dotted blue curves for reference. The insets highlight features that apparently arise from cation hydration shells. The spectra are normalized to the peak intensity.

Raman-MCR spectra represent the minimum area non-negative difference between a mixture and pure water. These spectra report on the perturbed O-H stretch features in bulk solutions

containing small solutes such as ions, which are presumed to arise in the first hydration shell. It is apparent that there is a large, common feature at 3450 cm^{-1} which dominates all spectra measured in Figure **5-1**. The Raman spectrum of the O-H stretching mode for pure water is known to show two prominent resonant features at ~ 3250 cm^{-1} and ~ 3420 cm^{-1}. There is evidence for two-state behavior and a fermi resonance contribution to this pair of peaks.[146,147] In the two-state model, a water molecule that is hydrogen bonded to 3 or 4 other waters gives rise to the mode at 3250 cm^{-1}, while waters that hydrogen bond to fewer waters give rise to the mode at 3420 cm^{-1}.[148] As such, the rather stand-alone feature at ~ 3450 cm^{-1} in the spectra presented in Figure 1 should arise from the first hydration shell of Cl^- where there are a significant number of broken water-water hydrogen bonds. Moreover, the spectral line shape is independent of the identity of the cation in the case of monovalent (Figure **5-1** A) and divalent (Figure **5-1** B) salts. This supports assignment of this mode to Cl^- hydration. Finally, this mode has previously been shown to be highly sensitive to the identity of the anion in solutions containing NaCl, NaBr or NaI. This, also, supports assignment of the mode to Cl^- hydration.

Previous studies have shown that Raman-MCR spectra of NaCl, KCl and CsCl solutions are independent of the identity of the cation. Cations such as Na^+, K^+ and Cs^+ may not be expected to perturb the spectrum in a significant way because such cations do not interact with hydration shell waters as tightly as ions like Li^+. As such, previous studies have attempted to study hydration of well hydrated cations by using a solution of NaCl as a stand in for the pure water solvent in efforts to eliminate the contribution from Cl^-.[75,149] In such experiments the mixture solution was LiCl, $MgCl_2$, $CaCl_2$ or $SrCl_2$. Such measurements reveal how the cation perturbs its waters relative to Na^+. Here we have taken a different approach by not removing intensity from Cl^- waters. In doing so, any intensity that arises from cation hydration shells reports on how significantly such waters are perturbed compared to pure water alone.

Upon addition of Hofmeister metal cation salts to solution, the only monovalent cation that gave rise to a measurable effect on the first hydration shell in Raman-MCR spectra was Li^+ (Figure **5-1** A inset). There is a small peak at ~ 3000 cm^{-1} that apparently arises from the presence of this cation. Such an effect was also observed in solutions containing divalent Hofmeister cations (Figure **5-**1 B inset). The perturbing effect of Mg^{2+}, Ca^{2+} and Sr^{2+} cations studied here follows an ion-specific series. Mg^{2+} gives rise to the largest perturbation of its hydration shell followed by Ca^{2+}. Moreover, Sr^{2+} cations do not significantly perturb the hydration shell. This is different from the interpretation arrived at if one performs anion elimination experiments with NaCl. In such studies, Li^+, Mg^{2+}, Ca^{2+} and Sr^{2+} all gave rise to non-zero intensity in comparison to Na^+.[149] While the first three cations give rise to intensity in our data, Sr^{2+} does not. As such, the more significant effect of Sr^{2+} when compared to Na^+ found in previous studies may not represent a significant perturbation, overall, in $SrCl_{2(aq)}$ solutions, especially in comparison to Cl^-.[150] This may have implications for binding events involving Sr^{2+}. Nevertheless, both our data and previous analyses suggest that Cl^- hydration waters vibrate at a higher frequency than that assigned to hydration shells of metal counter cations.

Hydration of Irving-Williams Metal Cations

Next, we turned attention to transition metal ions of the Irving-Williams series. In a second set of experiments, we measured Raman-MCR spectra of solutions containing $MnCl_2$, $NiCl_2$ or $ZnCl_2$. This data will be shown and discussed below. Raman spectra are known to be far less sensitive to perturbations at low frequencies in the O-H stretching region in comparison with IR spectra. This difference originates from the gross selection rules that govern IR and Raman transitions. Specifically, the dynamic dipole moment increases drastically as the strength of

hydrogen bonding increase at lower O-H frequencies due to a non-Condon effect as detailed in chapter 2. This is absent in Raman spectra and, indeed, the polarizability tensor is nearly constant as a function of the O-H stretch frequency. As such, we employed IR-MCR spectra to best compare the first hydration shell around Hofmeister and Irving-Williams metal cations. This data is shown below (Figure **5-2)**.

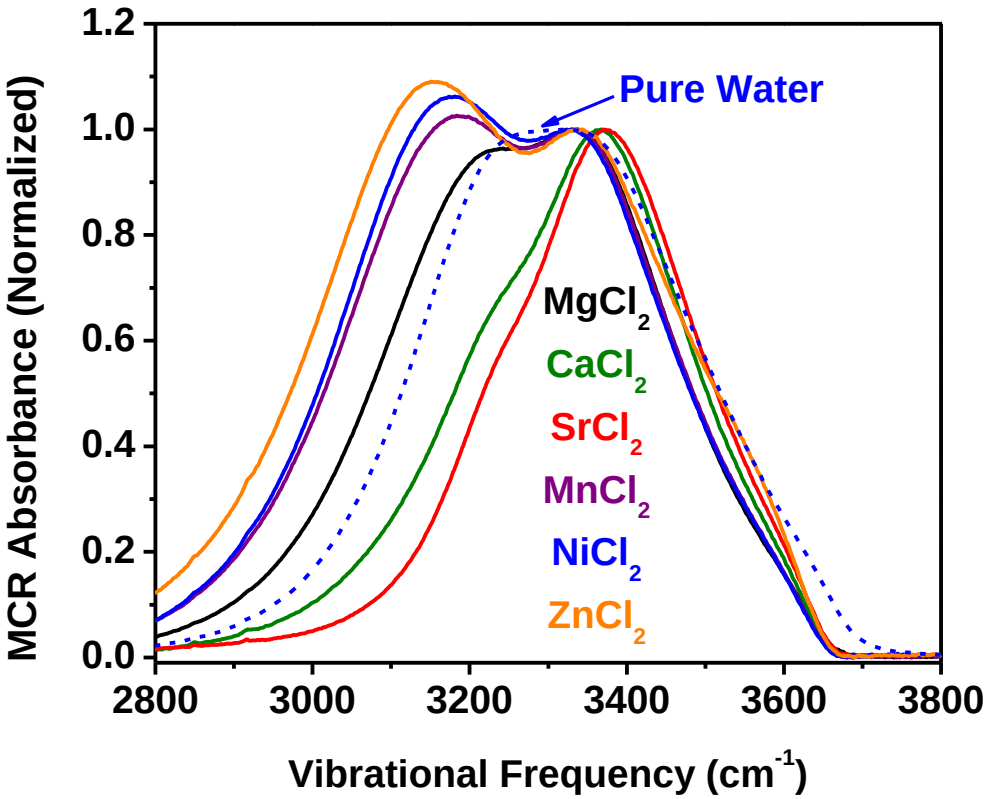

Figure **5-2**: ATR-FTIR-MCR spectra of salt solutions containing 1 M divalent metal cation chloride salts. A pure water spectrum is provided as a dotted blue curve. The spectra are normalized to the peak intensity of the Cl^- hydration shell signature at higher frequencies.

Mn^{2+}, Ni^{2+} and Zn^{2+} cations were chosen because they span the entire Irving-Williams series. Moreover, Zn^{2+} may be expected to behave more similarly to Hofmeister cations than transition metals due to the filled d-orbital set. Here we find a clear distinction between the hydration shells of Hofmeister and Irving-Williams cations. Specifically, Sr^{2+} has no measurable

effect on the hydration shell as was observed in Raman-MCR spectra. However, Ca^{2+} enhances the intensity at lower frequencies. This ordering matches the ordering observed in Raman-MCR spectra (Figure **5-1**). Moreover, Mg^{2+} enhances the intensity the most. While the ordering of Mg^{2+}, Ca^{2+} and Sr^{2+} hydration shells matches what was observed in Raman-MCR, it is obvious that IR-MCR spectra are more sensitive to perturbations at lower frequencies from the data presented in Figure **5-2**. This likely results from the non-Condon effect. Unlike in Raman-MCR spectra, the intensity at low frequencies in the O-H stretching region of IR-MCR spectra is almost as large as the signature of Cl^- hydration shells when Mg^{2+} cations are present. However, we have not found evidence to suggest a cation can give rise to apparently zero intensity in the Raman-MCR spectrum while giving rise to non-zero intensity in the IR-MCR spectrum.

Turing attention to transition metal cations in Figure **5-2**, it is apparent that the first hydration shell around these ions is affected in a completely different way than for Hofmeister cations. When $MnCl_2$ or $NiCl_2$ were added to solution, the intensity of the low frequency shoulder was larger than that from Cl^- hydration shells found at higher frequencies. While the intensity at lower frequencies rigorously represents a convolution of Cl^- and cation hydration shells, it is apparent that the overall intensity is largely enhanced by the contribution from the cation. The greater intensity from transition metals in comparison to Cl^- reveals a completely different cation hydration mechanism than that at play for Hofmeister cations, which did not enhance intensity at low frequencies to a greater extent than Cl^- in IR-MCR spectra. It is likely that this difference in cation hydration is due to charge transfer between water lone pairs and unfilled d-orbitals on Mn^{2+} or Ni^{2+} that are unavailable to Hofmeister ions. Such a phenomenon more closely resembles the mechanism of halide ion hydration, which involves charge transfer, in comparison to the mechanism of hydration for ions like Na^+. Hofmeister cations interact with the lone pairs of water by electrostatic forces. Moreover, the unfilled s-orbital on Na^+ is not accessible to water lone pairs. On the other hand, the d-orbitals on Irving-Williams cations are readily available. Apparently,

coordination of water molecules involving charge transfer with transition metal cations leads to a different pattern in the hydration shell spectrum compared to polarization of water lone pairs by Hofmeister cations.

The ability of IR-MCR to disentangle electrostatic interactions between cations and waters from interactions involving charge transfer provides an opportunity to study hydrated Zn^{2+} cations in the bulk solution. While zinc is often a poor catalyst due to its d^{10} electronic structure, it is a Lewis acid. In fact, the pH of 1 M $ZnCl_2$ was found to be ~ 5.3 while that of 1 M $NiCl_2$ was ~ 5. As such, some charge transfer is expected to be present in the hydration shell of Zn^{2+}. Indeed, the IR-MCR intensity at low frequencies for solutions containing $ZnCl_2$ more closely resembles $MnCl_2$ and $NiCl_2$ than $CaCl_2$ or $MgCl_2$. In fact, the contribution from Zn^{2+} cations enhance the net intensity at lower frequencies more than Cl^- as was observed with Mn^{2+} and Ni^{2+} cations. This suggests that Zn^{2+} cations accept a small amount of electron density from water lone pairs despite possessing a filled set of d-orbitals. Such charge transfer likely takes place between water lone pairs and outer orbitals that are shielded by the filled d-orbital set. Specifically, the 4s orbital is shielded by the d-orbitals, and this is expected to lower the energy of the s-orbital. As such, this outer orbital on Zn^{2+} participates in charge transfer unlike those on Ca^{2+} or Mg^{2+} cations. This is a ligation effect which represents a fundamentally different mechanism for cation hydration that has to be overcome when Zn^{2+} binds to a receptor in comparison to metal cations of the Hofmeister series.

The data presented above beg the question as to if transition metal cations universally perturb the O-H stretch mode more than Cl^-. Specifically, the fact that Ni^{2+}, Mn^{2+} and Zn^{2+} give rise to intensity which is greater than that assigned to Cl^- hydration in IR-MCR spectra is not necessarily true in Raman spectra due to the lack of a non-Condon effect. As such, we provide Raman-MCR spectra of $MnCl_2$, $NiCl_2$ and $ZnCl_2$ solutions in Figure **5-3**.

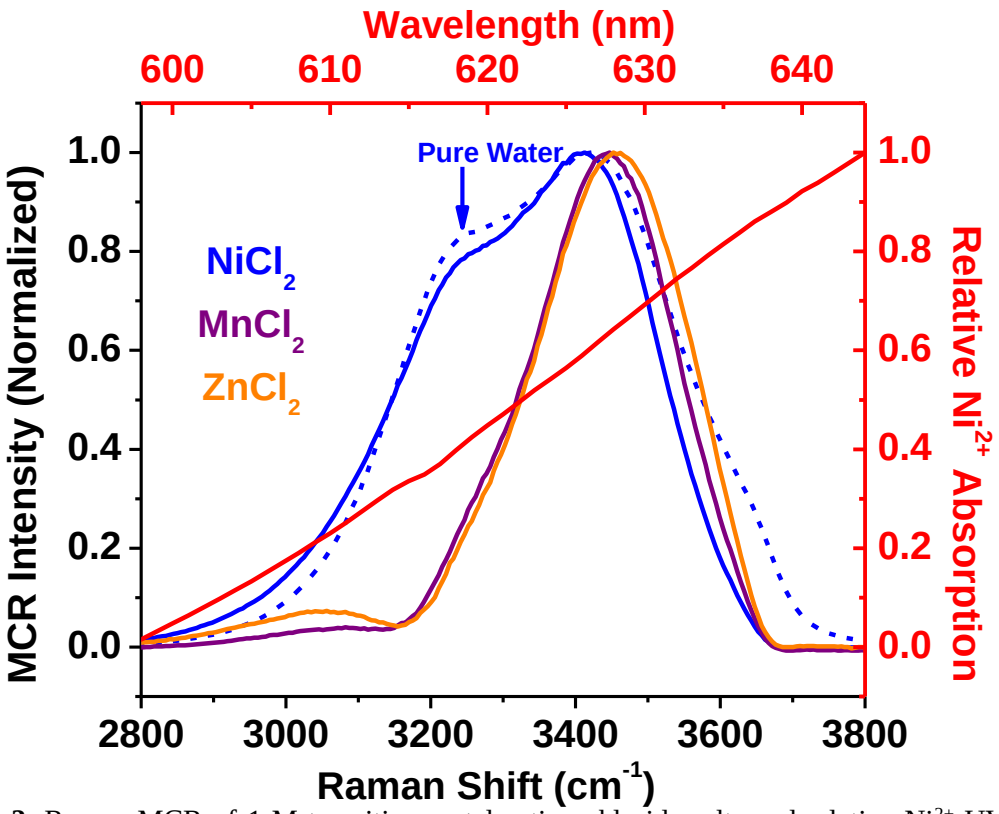

Figure **5-3**: Raman-MCR of 1 M transition metal cation chloride salts and relative Ni^{2+} UV/Vis absorption spectra (red).

Raman-MCR analysis of $MnCl_2$ and $ZnCl_2$ reveal a feature at low frequencies similar to Hofmeister cations as shown in Figure **5-1**. However, $NiCl_2$ gave rise to a green colored solution where the electronic absorption band strongly overlaps with the photon energies of Raman scatter produced using our laser. As such, scaling the bulk water signal with the MCR algorithm gave rise to an artifact in the perturbed O-H signal when Ni^{2+} was present. Specifically, the ability of Ni^{2+} to absorb Stoked shifted Raman scatter from water causes $NiCl_2$ to drastically reduce the signal from the bulk. As such, one has to add this back to the MCR difference spectrum in carrying out the algorithm correctly, and the result looks similar to bulk water. This renders the $NiCl_2$ spectrum useless for our purposes. However, resulting $MnCl_2$ and $ZnCl_2$ spectra were informative.

IR-MCR spectra in Figure **5-2** above show that all transition metals give rise to intensity larger than Cl^- hydration unlike Hofmeister cations. However, this is not true in Raman-MCR spectra (Figure **5-3**). As such, the strongly polarizing effect of cations on the IR transition moment is not the same for the Raman transition polarizability. Regardless of this finding, the intensity of transition metal hydration modes in Raman-MCR spectra at low frequencies is still much more perturbed than for Hofmeister cations. This is revealed by the greater intensity at ~ 3000 cm^{-1} in the presence of Zn^{2+} and Mn^{2+} than was observed for even the most perturbing Hofmeister cation, Mg^{2+}, in Figure **5-1**. As such, there is far greater perturbation of the water modes in Raman spectra by charge transfer to transition metal cations in comparison to Hofmeister cations. In contrast to IR-MCR, this does not give rise to greater intensity than Cl^-. As a result, our conclusions from IR-MCR that Irving-Williams cations perturb water differently than Hofmeister cations due to charge transfer is apparently universally true in vibrational spectra, but the greater intensity from such cations in comparison to Cl^- hydration found in IR spectra is not universally true. Rather, the IR selection rules conveniently highlight such charge transfer in a pronounced way compared with Raman selection rules.

When Cl^- is added to water to form a solution, a water molecule in the first hydration shell points one O-H bond toward the anion and the other toward the second hydration shell. The second shell may give rise to the shoulder near 3250 cm^{-1} that is present in all spectra provided in Figure **5-1**. Specifically, the shoulder may be argued to be a second shell around Cl^- that has a vibrational frequency red shifted from the first shell due to greater tetrahedrality expected in such as second shell. However, previous solvent isotope studies of NaCl solutions using Raman-MCR have shown that this shoulder is absent from the O-H stretching region when HOD in D_2O solvent is used.[37] As such, the shoulder need not be a second shell, but rather could arise from intramolecular coupling within the first shell. However, there is yet another possibility. It was shown in chapter 2 that in solutions containing OH^- anions, first shell O-H bonds pointed towards the anion have a different

vibrational frequency than O-H bonds pointed towards the second shell. This may also be true for Cl^- hydration waters. If one assigns the main peak at 3450 cm^{-1} to the O-H bond pointed at Cl^-, then the shoulder at 3250 cm^{-1} may be assigned to the hydrogen-bonded O-H that points towards the second shell. If such an assignment were true than one would expect using HOD in D_2O to shift the shoulder away from the O-H region of the spectrum and into the O-D region. These three possible assignments for the shoulder cannot be distinguished between in our experiments.

Conclusions

In conclusion, we found that the O-H stretch Raman-MCR spectra of a large library of salts containing monovalent and divalent Hofmeister metal cations and Cl^- counter anions are dominated by the hydration of the anion. The vibrational frequency of such water molecules is ~ 3450 cm^{-1}. However, strongly perturbing Li^+, Mg^{2+} and Ca^{2+} cations give rise to a small but measurable feature in Raman spectra at ~ 3000 cm^{-1}. The intensity of this mode is zero in the case of every monovalent cation expect Li^+. Mg^{2+} gives rise to the most intensity out of the divalent cations studied, while Ca^{2+} perturbs its water to a smaller extent. Moreover, Sr^{2+} did not give rise to a measurable effect in our data. These observations point to selectively in ion hydration shells alone capable of influencing cation binding events across a wide range of chemical systems. Furthermore, IR-MCR spectra revealed features of cation hydration more clearly, and this was exploited to compare the mechanisms of hydration between the Hofmeister and Irving-Williams series. We found that Mg^{2+} and Ca^{2+} both strongly perturb first shell waters in IR-MCR, and the intensity of cation-effected modes follows the same ordering as was observed in Raman-MCR spectra. However, Mn^{2+}, Ni^{2+} and Zn^{2+} all show different effects on the O-H stretching mode. Specifically, intensity of transition metal cation-effected water is larger than the signature of hydration for the counter anion. This was

not observed in the case of Hofmeister cations, and such an observation points to an intrinsic difference in cation hydration between the Irving-Williams and Hofmeister series. Namely, Hofmeister cations polarize first shell waters and do not participate in charge transfer. However, transition metal cations participate in charge transfer events with first shell waters. Such coordination is apparently present the hydration shell of Zn^{2+} despite the presence of a filled d-orbital set. This leads us to conclude that directly comparing the binding of Zn^{2+} with the binding of Hofmeister cations can be difficult to do correctly. This is especially true considering that charge transfer may also be present between ligands, that are found on a receptor, and Zn^{2+}. Our findings also point to the need to capture charge transfer in the hydration shell of Zn^{2+} cations in molecular dynamics simulations.

Chapter 6

THE JONES-RAY EFFECT IS NOT CAUSED BY SURFACE-ACTIVE IMPURITIES

Pure aqueous electrolyte solutions display a minimum in surface tension at concentrations of ~ 2 mM. This effect has been a source of controversy since first reported by Jones and Ray in the 1930s. The Jones-Ray effect has frequently been dismissed as an artifact linked to the presence of surface-active impurities. Herein we systematically consider the effect of surface-active impurities by purposely adding nanomolar concentrations of surfactants to dilute electrolyte solutions. Trace amounts of surfactant are indeed found to decrease the surface tension and influence the surface chemistry. However, surfactants can be removed by repeated aspiration and stirring cycles, that eventually deplete the surfactant from solution creating a "surface chemically pure" interface. Upon following this cleaning procedure, a reduction in the surface tension by millimolar concentrations of salt is still observed. These experiments were conducted by both myself and Sylvie Roke's group at the EPFL (Lausanne, Switzerland). Consequently, our collaboration demonstrates the Jones-Ray effect is not caused by surface active impurities.

Jones-Ray: Effect and Controversy

Aqueous interfaces are important for a plethora of biological, chemical and physical processes.[151] Quantifying interfacial properties has been a major aim in the last few decades and thus various experimental and simulation approaches have been introduced.[152-157] Generally, planar extended interfaces are employed in the experimental studies. For such surfaces, there is the

complication of having a small surface to volume ratio that gives rise to possible undetectable artifacts in the experimental data.[158] This is especially true when the contaminants are surfactants, which can be far more surface active than the materials under study (i.e. salts).

The influence of impurities is a topic that has long been a source of concern in the interfacial chemistry community.[159-166] The discussion was recently refueled by theoretical studies that suggested that surfactant impurities may be responsible for many surface chemical observations, and most notably for the Jones-Ray effect.[167,168] In 1937, Jones and Ray reported the surface tension of an aqueous KCl solutions at very low ionic strength.[169] They measured that the surface tension gradually decreases reaching a surface tension minimum at ~ 1 mM. Above 1-2 mM the surface tension gradually increases again. This observation has been a topic of much debate since the result is counter-intuitive and the change in surface tension is small. Impurities might, therefore, be a plausible cause, which would obviate the need for a discussion about the underlying mechanism.

The Jones-Ray effect has been recently reproduced.[170-172] Figure **6-1** shows the change in surface tension ($\Delta\gamma$) as a function of NaCl concentration in both H_2O and D_2O.

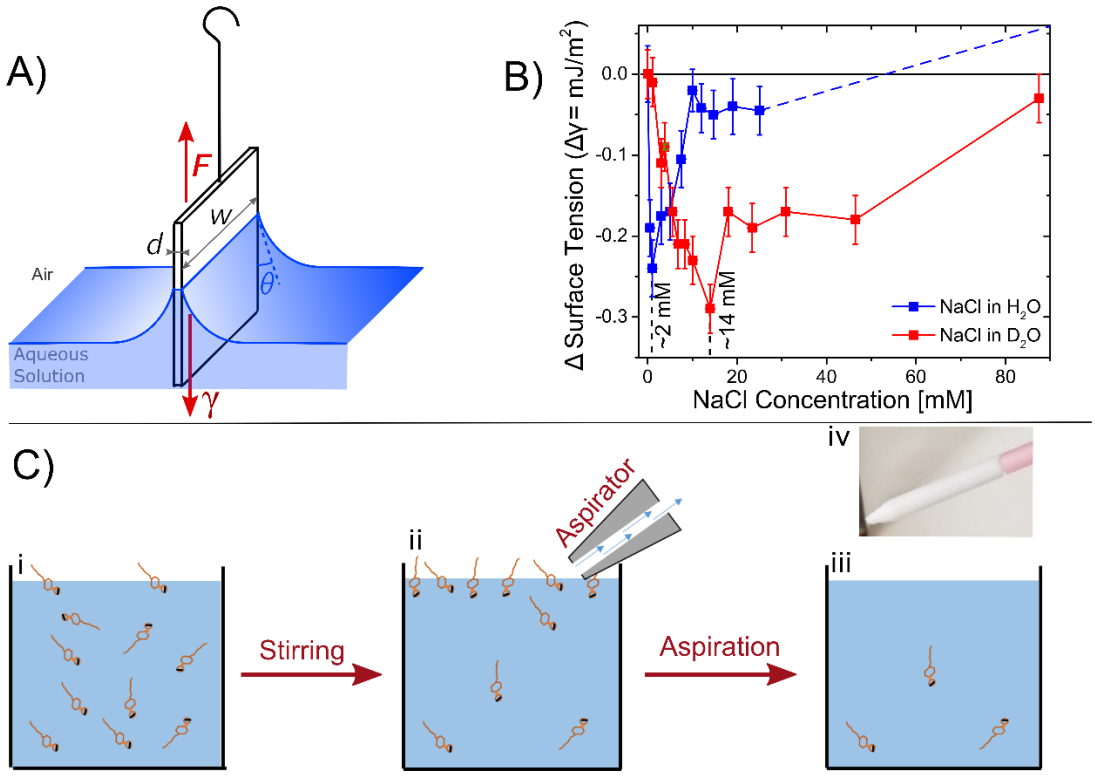

Figure **6-1**: (A) Illustration of the Wilhelmy plate method. (B) Surface tension difference ($\Delta\gamma$) measured as a function of NaCl concentration for solutions in H_2O (blue) and in D_2O (red). The red and blue lines connect the data points and the dashed blue line indicates the surface tension increase based on literature. (C) Interfacial cleaning protocol for removing trace impurities of surfactants. (i-iii) illustrations for the steps of stirring and aspiration cycles, and (iv) a photograph of the Teflon aspirator.

For both H_2O and D_2O, the surface tension decreases at low electrolyte concentrations. For NaCl in H_2O there is a minimum near 2 ± 1 mM. The minimum in surface tension occurs at ~ 14 mM for D_2O. These observations show that small changes in the surface tension of dilute salt solutions can be measured. Moreover, the minimum in the surface tension of the H_2O/air interface appears in the same concentration range as in the original measurements of Jones and Ray. D_2O solutions, on the other hand, display a minimum at a very different (~14 mM), but still low concentration. This difference suggests that the solvent-ion interactions play a major role in determining the free energy difference between the surface and the bulk (rather than the ion-surface

interaction, as in the high salt concentration range). Combining these measurements with elastic second harmonic scattering, reflection UV resonant second harmonic generation and modeling, it was recently concluded that the Jones-Ray effect is not an experimental artifact and relates to the interactions of ions with water.[173] It was proposed that the surface tension minimum originates from bulk ion-induced water-water correlations rather than ion adsorption at the interface. To be clear, these exist on very fast (femtosecond) timescales and do not represent a change in the bulk hydrogen bonding network. Rather, these measurements relate to ultrafast dipole-dipole correlations between water molecules. As ions are added to water, the hydrogen bond network of water responds to the collective electrostatic field of ions by increasing its orientational order. This increase in orientational order in the bulk solution gives rise to an entropic penalty, which drives ions to the surface and lowers the surface tension.

Recent computational studies have suggested that the surface tension changes found in Figure **6-1** B are caused by the presence of minute, undetectably small nanomolar concentrations of surfactants.[167,168] In these studies, it is argued that salt induced screening enhances the impurity adsorption at the interface, which leads to a depression in the surface tension. Although the question still remains as to how this could result in around an order of magnitude difference in salt concentration between H_2O and D_2O, the calculated results open up three questions that we investigate here:

- Can minute amounts of surfactants influence the surface tension and thus the surface chemistry of salt solutions?
- Is this mechanism responsible for the Jones-Ray effect?
- Does it cast doubt over all surface tension measurements?

Influence of Surfactants on Surface Tension

To answer these three questions, we have measured the surface tension with and without the addition of nanomolar concentrations of a negatively charged surfactant, and adopted a simple but effective surface cleaning approach, which consists of repeatedly aspirating the surface before performing the measurements. NaCl (Abcr and Sigma Aldrich 99.999%), and KCl (Acros Chemicals, 99.999%) were first baked at 600°C for 2 hours prior to use. Sodium Dodecylbenzene sulfonate (NaDBS) (Sigma Aldrich, Pharmaceutical secondary standard) is employed as the negatively charged surface-active impurity. A NANOpure Ultrapure Water System (Barnstead) and a Milli-Q-UF-Plus instrument (Millipore Inc.) were employed to obtain 18.1 MΩ.cm water to prepare light water (H_2O) samples. Samples were prepared in glassware that was cleaned by two different methods and identical results were achieved. In the first, the glassware was cleaned with piranha (3:1 H_2SO_4 (95-98%, Sigma) and H_2O_2 (30%, Macron Fine Chemicals) cleaned and rinsed with copious amounts of ultrapure water prior to use. In the second, a cleaning solution was prepared with Deconex® by 1:10 dilution and glassware were filled with this solution sonicated for an hour and washed and rinsed at least 10 times with MilliQ water.

Surface tension measurements were performed using the Wilhelmy plate method. The Wilhelmy plate method, as illustrated in Figure **6-1** A, uses a vertically suspended Pt plate with a perimeter (*l)* which is pulled out of the electrolyte solution towards the air. The force (*F*) acting on this plate was measured with a microbalance, and it was correlated to the surface tension (γ) as shown below (Equation **6-1**).

$$\gamma = \frac{F}{l \cos(\theta)} \qquad \text{Equation } \mathbf{6\text{-}1}$$

Here θ is the contact angle between Pt and water. θ is assumed to have a value of $\theta = 0$ based on literature. With $\theta = 0^{o}$ the measurement accuracy of the method is ~ 0.1 %.

To measure small changes in the surface tension, care needs to be taken to eliminate possible surface-active contaminants. To help eliminate this effect, all solutions were stored in closed glass containers with glass caps. The glassware was cleaned in a piranha solution (3:1 H_2SO_4:H_2O_2), or with Deconex® solutions and only ultra-pure salts were used as described above. Environmental influences including any possible dust contamination, vibrational instability, and temperature were minimized to the extent possible. The measurements were performed in a jacketed beaker and the temperature was monitored to remain at 20 ºC ± 0.05ºC over the course of the experiments. Moreover, personal protective equipment including nitrile gloves and clean room compatible garments were worn at all the times. The Pt Wilhelmy plate was first cleaned with a piranha solution or with Nochromix® (Sigma Aldrich) and then rinsed with copious amounts of MilliQ water to eliminate organic impurities from prior measurements. Additionally, it was cleaned with a hydrogen flame immediately prior to use.

Our method is inspired by a procedure frequently used in the Langmuir monolayers community, as well as in the removal of surface active contaminants from soluble surfactant solutions.[174,175] An aspirator is a small Teflon tip connected to a vacuum pump (Figure **6-1** C,iv) that can be used to remove the top most portion of the aqueous solution including the surface adsorbed molecules. By combining the aspiration procedure with stirring of the aqueous solution, it becomes possible to accelerate the interfacial adsorption of surfactants found in trace amounts in the bulk, which can then be removed, and eventually depleting the number of surfactants in solution.

Figure **6-2** shows the change in surface tension as a function of NaCl concentration in neat H_2O (black) and in H_2O to which 5 nM of sodium dodecylbenzene sulfonate (NaDBS) was added (red).

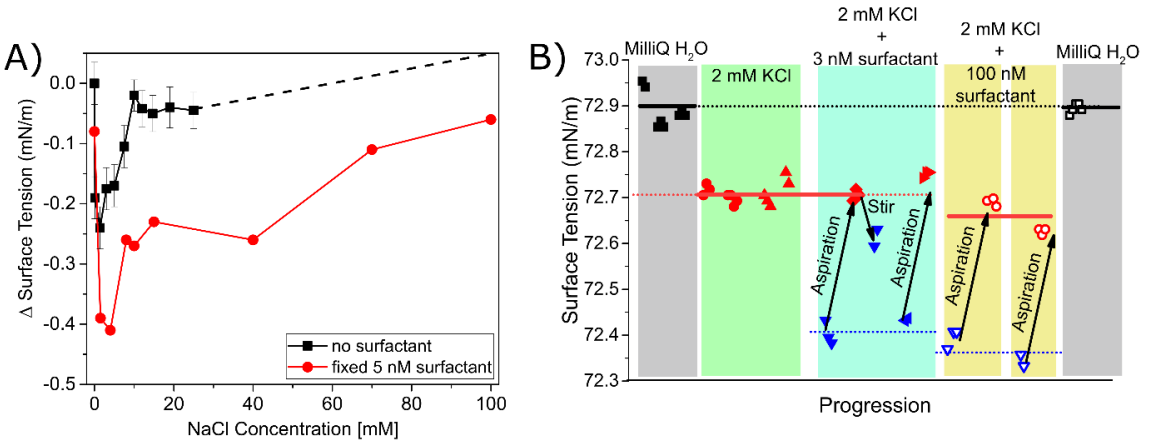

Figure **6-2**: (A) Surface tension data of a salt concentration series for NaCl added to ultrapure water (black trace), and a concentration series of NaCl added to a solution of 5 nM NaDBS. (B) Surface tension values for different aqueous solutions and aspiration/stirring cycles: ultrapure water (grey areas), 2 mM of KCl added to ultrapure water with stirring /aspiration (green), and 3 (100) nM NaDBS added to 2 mM KCl solution shown in cyan (yellow) area. Stirring /aspiration brings back the surface tension value to the pure 2 mM KCl solution value but not to the value of pure water (grey). Blue triangles (open and filled) show data points after stirring and before aspiration, whereas red and black (open and filled) data points show measurement after aspiration. Note that, measurements of different sample solutions with identical composition are indicated with differently shaped data points. Thus, the former measures the impurity contamination, and the latter measures the surfactant free interface.

These Wilhelmy plate measurements show minima in both curves at the same concentration ~ 2 mM, but with significantly different values: $\Delta\gamma$ = -0.24 mJ/m^2 at ~ 2 mM NaCl without NaDBS, and $\Delta\gamma$ = -0.41 mJ/m^2 at 1-4 mM NaCl with 5 nM of NaDBS added. This shows that surfactants can indeed decrease the surface tension minimum, and the mechanism could well be that the presence of charged ions enhances the local concentration of surfactants at the interface, thereby giving rise to an ion concentration dependent minimum in the interfacial tension.

Is the enhancement of surfactant impurities by electrolytes at the interface also an explanation for the Jones-Ray effect? To answer our second question, we have first measured again the Jones-Ray effect but this time with stirring / aspiration cycles. Figure **6-2** B shows the surface tension value of surface chemically pure water 18.1 MΩ.cm- (grey zone), and the surface tension values for a solution of 2 mM KCl that has been subject to 3 stirring / aspiration cycles. It can be

seen that the surface tension values remain ~ 0.2 mN/m lower compared to surface chemically pure water and remain identical for all measurements. This value coincides with the minimum found in Figure **6-1** B. Next, we measured a solution with the same salt concentration with 3 nM NaDBS added. A clear reduction in the surface tension is observed compared to surface chemically pure water and the 2 mM KCl solutions. As anticipated, this extra decrease in the surface tension values can be removed by aspiration of the air/water interface. After aspiration and upon continued stirring, the surface tension drops again on a time scale of 30 minutes. Stirring accelerates the adsorption of surfactant to the surface, as diffusion for nM surfactant concentrations is slow in the absence of convection. Aspirating again moves the surface tension back up to the initial value of the 2 mM KCl solutions, but not to that of neat water. The same behavior is observed if 100 nM of NaDBS is added. Repeated stirring/aspiration cycles will eventually deplete the surface-active species from solution, bringing the surface tension minimum close to the original value of a surface chemically pure 2 mM KCl solution. This shows that charged surfactants can indeed influence the surface tension of aqueous solutions, but a surface cleaning procedure can easily remove such impurity effects. We thus conclude that nM concentrations of surfactants in solution can decrease the surface tension minimum observable for salt solutions, as predicted by recent simulations studies.[167,168] However, stirring / aspiration cycles can remove the surfactants from the system, but do not lead to a disappearance of the Jones-Ray effect. This means that surface-active contaminants are not the cause of the Jones-Ray effect. Rather, ions induce small structural changes to the hydrogen bond network of water that result in a minimum of the surface tension.

In order to test the influence of the type of salt and the general applicability of the method, the results were repeated for aqueous NaCl solution at a different laboratory on another continent. The resulting data is shown here (Figure **6-3)**.

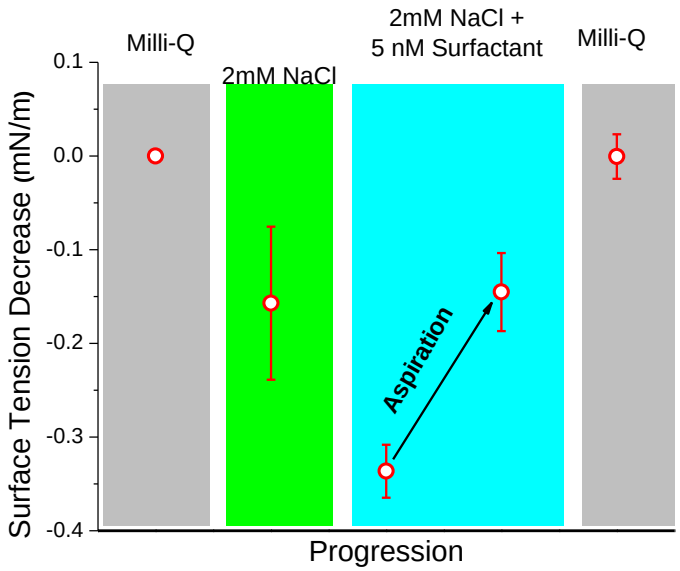

Figure **6-3**: The same approach in data collection as shown in Figure **6-2** was used, except that NaCl was used to prove the non-ion specificity of the Jones-Ray effect. Error bars represent uncertainties from triplicate measurements.

An impurity-based mechanism for the Jones-Ray effect would imply that an inherent level of irreproducibility should be present between researchers and at different locations where piping through which water flows is different, containers are different etc. To address this, we have performed surface tension measurements with the same surface-cleaning procedure at both EPFL and Penn State University, carried out by different researchers (Figure **6-2** & Figure **6-3**). The surface tension of pure water was measured (grey area; left) followed by that of 2 mM NaCl (green area). A solution of 2 mM NaCl and 5 nM sodium dodecylbenzene sulfonate (NaDBS) was introduced to a piranha cleaned glass dish, well stirred and probed (blue area, point #1). This was followed by surface aspiration and subsequent measurement of the surface tension (blue area, point #2) indicated by an arrow. The measured surface tension closely matched that from 2 mM NaCl solutions alone. Changing the solution again to ultrapure water, the initial surface tension value of pure water prior to addition of salt solutions was recovered. This indicates that the data in Figure

6-1 B are indeed ubiquitous. Furthermore, trace surface impurities can and do impact the surface tension, but clearly are not the fundamental reason for the Jones-Ray effect.

Conclusions

In summary, we have investigated the possibility that surfactant-active impurities influence surface chemistry and surface tension measurements in particular. We found a persistent surface tension minimum ($\Delta\gamma \sim$ -0.2 ± 0.05 mN/m) at 1-2 mM ionic strength for electrolyte aqueous solution/air interfaces, even with repeated stirring/aspiration cycles. This clearly indicates that an interplay of electrolytes and water is the underlying mechanism for the Jones-Ray effect, rather than an ion induced enhanced concentration of surfactants in the interfacial region. By contrast, when nanomolar concentrations of charged surfactants are present, the surface tension minimum is still observed at the same concentration, but drops to a lower value ($\Delta\gamma$ = -0.41 mN/m for NaCl). By removing the surfactant rich interfacial region using stirring-aspiration cycles, the surface tension reduces to that of the neat electrolyte solution/air interface. This shows that surface active impurities can give rise to an artifact in the surface tension and quite possibly to many other surface chemistry measurements (depending on how these are executed), but are not the origin of the Jones-Ray effect. The Jones-Ray effect stems from an interplay between ions and water, whereby the ions induce tiny modifications in correlations between water dipoles which results in a sizable entropic penalty over many layers of water at concentrations less than ~ 1 mM.

Chapter 7

CONCLUSIONS AND OUTLOOK

This work has provided insights into ion binding events across a broad range of chemical systems in aqueous solutions. Specifically, ion-ion and ion-dipole interactions have been focused upon. Additionally, transition metal cations of the Irving-Williams series were shown to interact with their hydration waters *via* charge transfer unlike Hofmeister cations. This interaction is reminiscent of a coordinate bond. Moreover, ion-water interactions in the bulk were shown to better explain the Jones-Ray effect than an impurity-based mechanism. Altogether, these results suggest that ion binding is best described by a competition model in which ion-water, receptor-water and ion-receptor affinities all must be considered. Consideration of these three factors promises to be useful for understanding binding events between small organic molecules as well as other species aside from ions. While this approach promises to be useful for understanding macromolecular behavior as well, interactions between these molecules are incredibly diverse. These molecules are capable of forming intramolecular interactions, which should also be assessed as a competition between hydration and direct contacts between function groups.

Using a competitive model to understand how ions bind requires sorting the binding site into either a hydrophobic, polar or charged category. This work presents evidence for counterion pairing in hydroxide solutions which follows a direct Hofmeister series. Moreover, this ion pair adopts a water-separated motif in the case of LiOH. This leads to a counter intuitive result in which ion mobility is slowed while proton sharing between water and hydroxide is promoted within the first hydration shell. This reveals that proton transfer can be impacted by intermolecular interactions such as ion pairing. Importantly, the fact that ion pairing is present at millimolar

concentrations reveals an asymmetry in counterion pairing between hydronium and hydroxide salts. Metal cations and OH^- pair more tightly than H^+ and halide anions. This contributes to apparent differences in mobility of H^+ and OH^- at millimolar concentrations, in addition to known differences in hydration shell structure. Finally, these findings promise to improve the development of energy producing and storing devices. Specifically, we have collected preliminary data of solutions containing CsOH. Ion mobility in solutions containing this salt is the largest of the alkali hydroxide salts. In fact $D_{effective,CsOH}$ is $\sim 8.1x10^{-5}$ cm^2/s at 1 mM, which is close to the value of $D_{effective,HCl}$ (see Appendix A). This is a result of poor ion pairing between Cs^+ and OH^-. Acidic fuel cells perform better than alkaline ones due to higher mobility of H^+ compared to OH^-. Based on our data, the use of CsOH has the potential to overcome this difference and improve the performance of alkaline fuel cells.

The impact of salts on the spectroscopic transition frequency of vibrational and optical probes has the potential to influence Stark shifts in buffers. These liquids usually have ions such as phosphate, sodium, chloride or carbonate. Buffer salts could accumulate around polar optical dyes used to detect binding events at membrane surfaces. They could also impact vibrational stark measurements performed on systems containing carbonyl or nitrile probes exposed to the bulk of a buffer solution. Our findings demonstrate that ion binding similar to that which underpins the Hofmeister effect also governs Onsager's local field model in a solution containing salt.

Studies of ion pairing in hydroxide solutions and Stark shifts in electrolytes reveal the presence of water-separated complexes, which follow either direct or reverse Hofmeister series. Importantly, contact pairing does not have to be present for ions to have measurable macroscopic effects. In fact, water-separated motifs modulate conductivity in basic water and the visible color emitted by dyes. These findings promise to be of both fundamental and applied use.

References

1. Davis, J. G.; Gierszal, K. P.; Wang, P.; Ben-Amotz, D. Water Structural Transformation at Molecular Hydrophobic Interfaces. *Nature* **2012**, *491* (7425), 582–585.
2. Rankin, B. M.; Ben-Amotz, D.; van der Post, S. T.; Bakker, H. J. Contacts Between Alcohols in Water Are Random Rather than Hydrophobic. *J. Phys. Chem. Lett.* **2015**, *6* (4), 688–692.
3. Ben-Amotz, D. Water-Mediated Hydrophobic Interactions. *Annual Review of Physical Chemistry* **2016**, *67* (1), 617–638.
4. Okur, H. I.; Hladílková, J.; Rembert, K. B.; Cho, Y.; Heyda, J.; Dzubiella, J.; Cremer, P. S.; Jungwirth, P. Beyond the Hofmeister Series: Ion-Specific Effects on Proteins and Their Biological Functions. *J. Phys. Chem. B* **2017**, *121* (9), 1997–2014.
5. Marcus, R. A. Ion Pairing and Electron Transfer. *J. Phys. Chem. B* **1998**, *102* (49), 10071–10077.
6. Neal, J. F.; Zhao, W.; Grooms, A. J.; Smeltzer, M. A.; Shook, B. M.; Flood, A. H.; Allen, H. C. Interfacial Supramolecular Structures of Amphiphilic Receptors Drive Aqueous Phosphate Recognition. *J. Am. Chem. Soc.* **2019**, *141* (19), 7876–7886.
7. Kherb, J.; Flores, S. C.; Cremer, P. S. Role of Carboxylate Side Chains in the Cation Hofmeister Series. *J. Phys. Chem. B* **2012**, *116* (25), 7389–7397.
8. Yoshimoto, S.; Itaya, K. Adsorption and Assembly of Ions and Organic Molecules at Electrochemical Interfaces: Nanoscale Aspects. *Annual Review of Analytical Chemistry* **2013**, *6* (1), 213–235.
9. Bruce, E. E.; Okur, H. I.; Stegmaier, S.; Drexler, C. I.; Rogers, B. A.; van der Vegt, N. F. A.; Roke, S.; Cremer, P. S. Molecular Mechanism for the Interactions of Hofmeister

Cations with Macromolecules in Aqueous Solution. *J. Am. Chem. Soc.* **2020**, *142* (45), 19094–19100.

10. Drexler, C. I.; Miller, T. C.; Rogers, B. A.; Li, Y. C.; Daly, C. A.; Yang, T.; Corcelli, S. A.; Cremer, P. S. Counter Cations Affect Transport in Aqueous Hydroxide Solutions with Ion Specificity. *J. Am. Chem. Soc.* **2019**, *141* (17), 6930–6936.
11. Okur, H. I.; Drexler, C. I.; Tyrode, E.; Cremer, P. S.; Roke, S. The Jones–Ray Effect Is Not Caused by Surface-Active Impurities. *J. Phys. Chem. Lett.* **2018**, *9* (23), 6739–6743.
12. Darnell, J.; Lodish, H.; Baltimore, D. Molecular Cell Biology; Scientific American Books: New York, **1990**.
13. Braverman, L. E.; He, X.; Pino, S.; Cross, M.; Magnani, B.; Lamm, S. H.; Kruse, M. B.; Engel, A.; Crump, K. S.; Gibbs, J. P. The Effect of Perchlorate, Thiocyanate, and Nitrate on Thyroid Function in Workers Exposed to Perchlorate Long-Term. *J Clin Endocrinol Metab* **2005**, *90* (2), 700–706.
14. Wojciechowski, K.; Kucharek, M.; Wróblewski, W.; Warszyński, P. On the Origin of the Hofmeister Effect in Anion-Selective Potentiometric Electrodes with Tetraalkylammonium Salts. *Journal of Electroanalytical Chemistry* **2010**, *638* (2), 204–211.
15. DeWalt-Kerian, E. L.; Kim, S.; Azam, Md. S.; Zeng, H.; Liu, Q.; Gibbs, J. M. PH-Dependent Inversion of Hofmeister Trends in the Water Structure of the Electrical Double Layer. *J. Phys. Chem. Lett.* **2017**, *8* (13), 2855–2861.
16. Bauduin, P.; Renoncourt, A.; Touraud, D.; Kunz, W.; Ninham, B. W. Hofmeister Effect on Enzymatic Catalysis and Colloidal Structures. *Current Opinion in Colloid & Interface Science* **2004**, *9* (1), 43–47.
17. Rydeen, A. E.; Brustad, E. M.; Pielak, G. J. Osmolytes and Protein–Protein Interactions. *J. Am. Chem. Soc.* **2018**, *140* (24), 7441–7444.

18. Hofmeister, F. Zur Lehre Von Der Wirkung Der Salze. *Naunyn-Schmiedeberg's Arch. Pharmacol*. **1888**, 24, 247−260.
19. Hofmeister, F. Zur Lehre Von Der Wirkung Der Salze. *Naunyn-Schmiedeberg's Arch. Pharmacol.* **1888**, 25, 1−30.
20. Collins, K. D.; Washabaugh, M. W. The Hofmeister Effect and the Behaviour of Water at Interfaces. *Quarterly Reviews of Biophysics* **1985**, *18* (4), 323–422.
21. Soper, A. K.; Ricci, M. A. Structures of High-Density and Low-Density Water. *Phys. Rev. Lett.* **2000**, *84* (13), 2881–2884.
22. Leberman, R.; Soper, A. K. Effect of High Salt Concentrations on Water Structure. *Nature* **1995**, *378* (6555), 364–366.
23. Paterová, J.; Rembert, K. B.; Heyda, J.; Kurra, Y.; Okur, H. I.; Liu, W. R.; Hilty, C.; Cremer, P. S.; Jungwirth, P. Reversal of the Hofmeister Series: Specific Ion Effects on Peptides. *J. Phys. Chem. B* **2013**, *117* (27), 8150–8158.
24. Iscen, A.; Schatz, G. C. Hofmeister Effects on Peptide Amphiphile Nanofiber Self-Assembly. *J. Phys. Chem. B* **2019**, *123* (32), 7006–7013.
25. Batchelor, J. D.; Olteanu, A.; Tripathy, A.; Pielak, G. J. Impact of Protein Denaturants and Stabilizers on Water Structure. *J. Am. Chem. Soc.* **2004**, *126* (7), 1958–1961.
26. Omta, A. W.; Kropman, M. F.; Woutersen, S.; Bakker, H. J. Negligible Effect of Ions on the Hydrogen-Bond Structure in Liquid Water. *Science* **2003**, *301* (5631), 347–349.
27. Zhang, Y.; Cremer, P. S. Interactions between Macromolecules and Ions: The Hofmeister Series. *Current Opinion in Chemical Biology* **2006**, *10* (6), 658–663.
28. Zhang, Y.; Furyk, S.; Bergbreiter, D. E.; Cremer, P. S. Specific Ion Effects on the Water Solubility of Macromolecules: PNIPAM and the Hofmeister Series. *J. Am. Chem. Soc.* **2005**, *127* (41), 14505–14510.

29. Zhang, Y.; Cremer, P. S. The Inverse and Direct Hofmeister Series for Lysozyme. *PNAS* **2009**, *106* (36), 15249–15253.

30. Rembert, K. B.; Paterová, J.; Heyda, J.; Hilty, C.; Jungwirth, P.; Cremer, P. S. Molecular Mechanisms of Ion-Specific Effects on Proteins. *J. Am. Chem. Soc.* **2012**, *134* (24), 10039–10046.

31. Okur, H. I.; Kherb, J.; Cremer, P. S. Cations Bind Only Weakly to Amides in Aqueous Solutions. *J. Am. Chem. Soc.* **2013**, *135* (13), 5062–5067.

32. van der Vegt, N. F. A.; Haldrup, K.; Roke, S.; Zheng, J.; Lund, M.; Bakker, H. J. Water-Mediated Ion Pairing: Occurrence and Relevance. *Chem. Rev.* **2016**, *116* (13), 7626–7641.

33. Liu, J.; Zhang, J. Z. H.; He, X. Probing the Ion-Specific Effects at the Water/Air Interface and Water-Mediated Ion Pairing in Sodium Halide Solution with Ab Initio Molecular Dynamics. *J. Phys. Chem. B* **2018**, *122* (44), 10202–10209.

34. Fennell, C. J.; Bizjak, A.; Vlachy, V.; Dill, K. A. Ion Pairing in Molecular Simulations of Aqueous Alkali Halide Solutions. *J. Phys. Chem. B* **2009**, *113* (19), 6782–6791.

35. Roy, S.; Baer, M. D.; Mundy, C. J.; Schenter, G. K. Marcus Theory of Ion-Pairing. *J. Chem. Theory Comput.* **2017**, *13* (8), 3470–3477.

36. Collins, K. D.; Neilson, G. W.; Enderby, J. E. Ions in Water: Characterizing the Forces That Control Chemical Processes and Biological Structure. *Biophysical Chemistry* **2007**, *128* (2), 95–104.

37. Perera, P. N.; Browder, B.; Ben-Amotz, D. Perturbations of Water by Alkali Halide Ions Measured Using Multivariate Raman Curve Resolution. *J. Phys. Chem. B* **2009**, *113* (7), 1805–1809.

38. Petersen, P. B.; Saykally, R. J. Confirmation of Enhanced Anion Concentration at the Liquid Water Surface. *Chemical Physics Letters* **2004**, *397* (1), 51–55.

39. Sperling, R.; Treinin, A. Charge-Transfer-to-Solvent Spectra of Polyvalent Anions. II. The Electronic Spectrum of S2O3-2. *J. Phys. Chem.* **1964**, *68* (4), 897–903.

40. Blandamer, M. J.; Fox, M. F. Theory and Applications of Charge-Transfer-to-Solvent Spectra. *Chem. Rev.* **1970**, *70* (1), 59–93.

41. Burak, I.; Treinin, A. Solvent Scale for Charge-Transfer-to-Solvent Spectra of Anions. *Trans. Faraday Soc.* **1963**, *59* (0), 1490–1496.

42. Kloepfer, J. A.; Vilchiz, V. H.; Lenchenkov, V. A.; Bradforth, S. E. Femtosecond Dynamics of Photodetachment of the Iodide Anion in Solution: Resonant Excitation into the Charge-Transfer-to-Solvent State. *Chemical Physics Letters* **1998**, *298* (1), 120–128.

43. Ben-Amotz, D. Hydration-Shell Vibrational Spectroscopy. *J. Am. Chem. Soc.* **2019**, *141* (27), 10569–10580.

44. Fega, K. R.; Wilcox, A. S.; Ben-Amotz, D. Application of Raman Multivariate Curve Resolution to Solvation-Shell Spectroscopy. *Appl Spectrosc* **2012**, *66* (3), 282–288.

45. Duso, A. B.; Chen, D. D. Y. Proton and Hydroxide Ion Mobility in Capillary Electrophoresis. *Anal. Chem.* **2002**, *74* (13), 2938–2942.

46. Johnston, J. The Change of the Equivalent Conductance of Ions with the Temperature. *J. Am. Chem. Soc.* **1909**, *31* (9), 1010–1020.

47. Noyes, A. A.; Kato, Y. The Equivalent Conductance of Hydrogen-Ion Derived from Transference Experiments with Nitric Acid. *J. Am. Chem. Soc.* **1908**, *30* (3), 318–334.

48. Marx, D. Proton Transfer 200 Years after von Grotthuss: Insights from *Ab Initio* Simulations. *ChemPhysChem* **2006**, *7* (9), 1848–1870.

49. Marx, D.; Chandra, A.; Tuckerman, M. E. Aqueous Basic Solutions: Hydroxide Solvation, Structural Diffusion, and Comparison to the Hydrated Proton. *Chem. Rev.* **2010**, *110* (4), 2174–2216.

50. Onsager, L. The Motion of Ions: Principles and Concepts. *Science* **1969**, *166* (3911), 1359–1364.

51. Agmon, N.; Bakker, H. J.; Campen, R. K.; Henchman, R. H.; Pohl, P.; Roke, S.; Thämer, M.; Hassanali, A. Protons and Hydroxide Ions in Aqueous Systems. *Chem. Rev.* **2016**, *116* (13), 7642–7672.

52. Marx, D.; Tuckerman, M. E.; Hutter, J.; Parrinello, M. The Nature of the Hydrated Excess Proton in Water. *Nature; London* **1999**, *397* (6720), 601–604.

53. Tuckerman, M. E.; Marx, D.; Parrinello, M. The Nature and Transport Mechanism of Hydrated Hydroxide Ions in Aqueous Solution. *Nature; London* **2002**, *417* (6892), 925–929.

54. Hassanali, A.; Giberti, F.; Cuny, J.; Kühne, T. D.; Parrinello, M. Proton Transfer through the Water Gossamer. *Proc. Natl. Acad. Sci.* **2013**, *110* (34), 13723–13728.

55. Chen, M.; Zheng, L.; Santra, B.; Ko, H.-Y.; DiStasio Jr, R. A.; Klein, M. L.; Car, R.; Wu, X. Hydroxide Diffuses Slower than Hydronium in Water Because Its Solvated Structure Inhibits Correlated Proton Transfer. *Nature Chemistry* **2018**, *10* (4), 413–419.

56. Walrafen, G. E.; Yang, W.-H.; Chu, Y. C. High-Temperature Raman Investigation of Concentrated Sulfuric Acid Mixtures: Measurement of H-Bond ΔH Values between H_3O^+ or $H_5O_2^+$ and HSO_4^-. *J. Phys. Chem. A* **2002**, *106* (43), 10162–10173.

57. Janoschek, R.; G. Weidemann, E.; Zundel, G. Calculated Frequencies and Intensities Associated with Coupling of the Proton Motion with the Hydrogen Bond Stretching Vibration in a Double Minimum Potential Surface. *Journal of the Chemical Society, Faraday Transactions 2: Molecular and Chemical Physics* **1973**, *69* (0), 505–520.

58. Roberts, S. T.; Petersen, P. B.; Ramasesha, K.; Tokmakoff, A.; Ufimtsev, I. S.; Martinez, T. J. Observation of a Zundel-like Transition State during Proton Transfer in Aqueous Hydroxide Solutions. *Proc. Natl. Acad. Sci.* **2009**, *106* (36), 15154–15159.

59. Mandal, A.; Ramasesha, K.; De Marco, L.; Tokmakoff, A. Collective Vibrations of Water-Solvated Hydroxide Ions Investigated with Broadband 2DIR Spectroscopy. *J. Chem. Phys.* **2014**, *140* (20), 204508.

60. Thämer, M.; Marco, L. D.; Ramasesha, K.; Mandal, A.; Tokmakoff, A. Ultrafast 2D IR Spectroscopy of the Excess Proton in Liquid Water. *Science* **2015**, *350* (6256), 78–82.

61. Walrafen, G. E.; Douglas, R. T. W. Raman Spectra from Very Concentrated Aqueous NaOH and from Wet and Dry, Solid, and Anhydrous Molten, LiOH, NaOH, and KOH. *J. Chem. Phys.* **2006**, *124* (11), 114504.

62. Mandal, A.; Tokmakoff, A. Vibrational Dynamics of Aqueous Hydroxide Solutions Probed Using Broadband 2DIR Spectroscopy. *J. Chem. Phys.* **2015**, *143* (19), 194501.

63. Baer, M. D.; Fulton, J. L.; Balasubramanian, M.; Schenter, G. K.; Mundy, C. J. Persistent Ion Pairing in Aqueous Hydrochloric Acid. *J. Phys. Chem. B* **2014**, *118* (26), 7211–7220.

64. Walewski, Ł.; Forbert, H.; Marx, D. Quantum Induced Bond Centering in Microsolvated HCl: Solvent Separated versus Contact Ion Pairs. *J. Phys. Chem. Lett.* **2011**, *2* (24), 3069–3074.

65. Fulton, J. L.; Balasubramanian, M. Structure of Hydronium (H_3O^+)/Chloride (Cl^-) Contact Ion Pairs in Aqueous Hydrochloric Acid Solution: A Zundel-like Local Configuration. *J. Am. Chem. Soc.* **2010**, *132* (36), 12597–12604.

66. Gutberlet, A.; Schwaab, G.; Birer, Ö.; Masia, M.; Kaczmarek, A.; Forbert, H.; Havenith, M.; Marx, D. Aggregation-Induced Dissociation of $HCl(H_2O)_4$ Below 1 K: The Smallest Droplet of Acid. *Science* **2009**, *324* (5934), 1545–1548.

67. Tuckerman, M. E.; Chandra, A.; Marx, D. Structure and Dynamics of OH^-(aq). *Acc. Chem. Res.* **2006**, *39* (2), 151–158.

68. Zhu, Z.; Tuckerman, M. E. Ab Initio Molecular Dynamics Investigation of the Concentration Dependence of Charged Defect Transport in Basic Solutions via Calculation of the Infrared Spectrum. *J. Phys. Chem. B* **2002**, *106* (33), 8009–8018.

69. Harris, K. R. Relations between the Fractional Stokes−Einstein and Nernst−Einstein Equations and Velocity Correlation Coefficients in Ionic Liquids and Molten Salts. *J. Phys. Chem. B* **2010**, *114* (29), 9572–9577.

70. Noulty, R. A.; Leaist, D. G. Activity Coefficients and Diffusion Coefficients of Dilute Aqueous Solutions of Lithium, Sodium, and Potassium Hydroxides. *J Solution Chem* **1984**, *13* (11), 767–778.

71. Hemmer, P. C. *The Collected Works of Lars Onsager*; World Scientific, 1996.

72. Hutter, J.; Iannuzzi, M.; Schiffmann, F.; VandeVondele, J. CP2K: Atomistic Simulations of Condensed Matter Systems: CP2K Simulation Software. *Wiley Interdiscip. Rev. Comput. Mol. Sci.* **2014**, *4* (1), 15–25.

73. Towns, J.; Cockerill, T.; Dahan, M.; Foster, I.; Gaither, K.; Grimshaw, A.; Hazlewood, V.; Lathrop, S.; Lifka, D.; Peterson, G. D.; et al. XSEDE: Accelerating Scientific Discovery. *Comput. Sci. Eng.* **2014**, *16* (5), 62–74.

74. Martínez, L.; Andrade, R.; Birgin, E. G.; Martínez, J. M. PACKMOL: A Package for Building Initial Configurations for Molecular Dynamics Simulations. *J. Comput. Chem.* **2009**, *30* (13), 2157–2164.

75. Daly, C. A.; Streacker, L. M.; Sun, Y.; Pattenaude, S. R.; Hassanali, A. A.; Petersen, P. B.; Corcelli, S. A.; Ben-Amotz, D. Decomposition of the Experimental Raman and Infrared Spectra of Acidic Water into Proton, Special Pair, and Counterion Contributions. *J. Phys. Chem. Lett.* **2017**, *8* (21), 5246–5252.

76. VandeVondele, J.; Krack, M.; Mohamed, F.; Parrinello, M.; Chassaing, T.; Hutter, J. Quickstep: Fast and Accurate Density Functional Calculations Using a Mixed Gaussian and Plane Waves Approach. *Comput. Phys. Commun.* **2005**, *167* (2), 103–128.

77. Hartwigsen, C.; Goedecker, S.; Hutter, J. Relativistic Separable Dual-Space Gaussian Pseudopotentials from H to Rn. *Phys. Rev. B* **1998**, *58* (7), 3641–3662.

78. Goedecker, S.; Teter, M.; Hutter, J. Separable Dual-Space Gaussian Pseudopotentials. *Phys. Rev. B* **1996**, *54* (3), 1703–1710.

79. Krack, M. Pseudopotentials for H to Kr Optimized for Gradient-Corrected Exchange-Correlation Functionals. *Theor. Chem. Acc.* **2005**, *114* (1–3), 145–152.

80. Becke, A. D. Density-Functional Exchange-Energy Approximation with Correct Asymptotic Behavior. *Phys. Rev. A* **1988**, *38* (6), 3098–3100.

81. Lee, C.; Yang, W.; Parr, R. G. Development of the Colle-Salvetti Correlation-Energy Formula into a Functional of the Electron Density. *Phys. Rev. B* **1988**, *37* (2), 785–789.

82. Grimme, S.; Antony, J.; Ehrlich, S.; Krieg, H. A Consistent and Accurate *Ab Initio* Parametrization of Density Functional Dispersion Correction (DFT-D) for the 94 Elements H-Pu. *J. Chem. Phys.* **2010**, *132* (15), 154104.

83. Marcus, Y.; Hefter, G. Ion Pairing. *Chem. Rev.* **2006**, *106* (11), 4585–4621.

84. Corridoni, T.; Sodo, A.; Bruni, F.; Ricci, M. A.; Nardone, M. Probing Water Dynamics with OH^-. *Chemical Physics* **2007**, *336* (2), 183–187.

85. Sbroscia, M.; Sodo, A.; Bruni, F.; Corridoni, T.; Ricci, M. A. OH Stretching Dynamics in Hydroxide Aqueous Solutions. *J. Phys. Chem. B* **2018**, *122* (14), 4077–4082.

86. Yoshimura, Y.; Kanno, H. Cationic Effects in the Raman OD Stretching Spectra of Aqueous Electrolyte Solutions. *J. Raman Spectrosc.* **1996**, *27* (9), 671–674.

87. Walrafen, G. E. Raman Spectral Studies of the Effects of Perchlorate Ion on Water Structure. *J. Chem. Phys.* **1970**, *52* (8), 4176–4198.

88. Lee, H.; Choi, J.-H.; Cho, M. Vibrational Solvatochromism and Electrochromism of Cyanide, Thiocyanate, and Azide Anions in Water. *PCCP* **2010**, *12* (39), 12658–12669.

89. Bajaj, P.; Götz, A. W.; Paesani, F. Toward Chemical Accuracy in the Description of Ion–Water Interactions through Many-Body Representations. I. Halide–Water Dimer Potential Energy Surfaces. *J. Chem. Theory Comput.* **2016**, *12* (6), 2698–2705.

90. Galib, M.; Baer, M. D.; Skinner, L. B.; Mundy, C. J.; Huthwelker, T.; Schenter, G. K.; Benmore, C. J.; Govind, N.; Fulton, J. L. Revisiting the Hydration Structure of Aqueous Na^+. *J. Chem. Phys.* **2017**, *146* (8), 84504.

91. Hermansson, K.; Bopp, P. A.; Spångberg, D.; Pejov, L.; Bakó, I.; Mitev, P. D. The Vibrating Hydroxide Ion in Water. *Chem. Phys. Lett.* **2011**, *514* (1–3), 1–15.

92. Mondal, J. A.; Namboodiri, V.; Mathi, P.; Singh, A. K. Alkyl Chain Length Dependent Structural and Orientational Transformations of Water at Alcohol–Water Interfaces and Its Relevance to Atmospheric Aerosols. *J. Phys. Chem. Lett.* **2017**, *8* (7), 1637–1644.

93. Colbert, D. T.; Miller, W. H. A Novel Discrete Variable Representation for Quantum Mechanical Reactive Scattering via the *S*-matrix Kohn Method. *J. Chem. Phys.* **1992**, *96* (3), 1982–1991.

94. Schmidt, J. R.; Corcelli, S. A.; Skinner, J. L. Pronounced Non-Condon Effects in the Ultrafast Infrared Spectroscopy of Water. *J. Chem. Phys.* **2005**, *123* (4), 044513.

95. Corcelli, S. A.; Skinner, J. L. Infrared and Raman Line Shapes of Dilute HOD in Liquid H_2O and D_2O from 10 to 90 °C. *J. Phys. Chem. A* **2005**, *109* (28), 6154–6165.

96. Auer, B.; Kumar, R.; Schmidt, J. R.; Skinner, J. L. Hydrogen Bonding and Raman, IR, and 2D-IR Spectroscopy of Dilute HOD in Liquid D_2O. *Proc. Natl. Acad. Sci.* **2007**, *104* (36), 14215–14220.

97. Fournier, J. A.; Carpenter, W. B.; Lewis, N. H. C.; Tokmakoff, A. Broadband 2D IR Spectroscopy Reveals Dominant Asymmetric $H_5O_2^+$ Proton Hydration Structures in Acid Solutions. *Nat. Chem.* **2018**, *10* (9), 932.

98. Onsager, L. Electric Moments of Molecules in Liquids. *J. Am. Chem. Soc.* **1936**, *58* (8), 1486–1493.

99. Levinson, N. M.; Fried, S. D.; Boxer, S. G. Solvent-Induced Infrared Frequency Shifts in Aromatic Nitriles Are Quantitatively Described by the Vibrational Stark Effect. *J. Phys. Chem. B* **2012**, *116* (35), 10470–10476.

100. Sorenson, S. A.; Patrow, J. G.; Dawlaty, J. M. Solvation Reaction Field at the Interface Measured by Vibrational Sum Frequency Generation Spectroscopy. *J. Am. Chem. Soc.* **2017**, *139* (6), 2369–2378.

101. Fried, S. D.; Bagchi, S.; Boxer, S. G. Measuring Electrostatic Fields in Both Hydrogen-Bonding and Non-Hydrogen-Bonding Environments Using Carbonyl Vibrational Probes. *J. Am. Chem. Soc.* **2013**, *135* (30), 11181–11192.

102. Fried, S. D.; Boxer, S. G. Measuring Electric Fields and Noncovalent Interactions Using the Vibrational Stark Effect. *Acc. Chem. Res.* **2015**, *48* (4), 998–1006.

103. Sarkar, S.; Maitra, A.; Banerjee, S.; Thoi, V. S.; Dawlaty, J. M. Electric Fields at Metal–Surfactant Interfaces: A Combined Vibrational Spectroscopy and Capacitance Study. *J. Phys. Chem. B* **2020**, *124* (7), 1311–1321.

104. Marini, A.; Muñoz-Losa, A.; Biancardi, A.; Mennucci, B. What Is Solvatochromism? *J. Phys. Chem. B* **2010**, *114* (51), 17128–17135.

105. Klymchenko, A. S. Solvatochromic and Fluorogenic Dyes as Environment-Sensitive Probes: Design and Biological Applications. *Acc. Chem. Res.* **2017**, *50* (2), 366–375.

106. Fried, S. D.; Bagchi, S.; Boxer, S. G. Extreme Electric Fields Power Catalysis in the Active Site of Ketosteroid Isomerase. *Science* **2014**, *346* (6216), 1510–1514.

107. Fried, S. D.; Boxer, S. G. Electric Fields and Enzyme Catalysis. *Annual Review of Biochemistry* **2017**, *86* (1), 387–415.

108. Bagchi, S.; Fried, S. D.; Boxer, S. G. A Solvatochromic Model Calibrates Nitriles' Vibrational Frequencies to Electrostatic Fields. *J. Am. Chem. Soc.* **2012**, *134* (25), 10373–10376.

109. Saggu, M.; Fried, S. D.; Boxer, S. G. Local and Global Electric Field Asymmetry in Photosynthetic Reaction Centers. *J. Phys. Chem. B* **2019**, *123* (7), 1527–1536.

110. Patrow, J. G.; Sorenson, S. A.; Dawlaty, J. M. Direct Spectroscopic Measurement of Interfacial Electric Fields near an Electrode under Polarizing or Current-Carrying Conditions. *J. Phys. Chem. C* **2017**, *121* (21), 11585–11592.

111. Schneider, S. H.; Boxer, S. G. Vibrational Stark Effects of Carbonyl Probes Applied to Reinterpret IR and Raman Data for Enzyme Inhibitors in Terms of Electric Fields at the Active Site. *J. Phys. Chem. B* **2016**, *120* (36), 9672–9684.

112. Reed, A. E.; Curtiss, L. A.; Weinhold, F. Intermolecular Interactions from a Natural Bond Orbital, Donor-Acceptor Viewpoint. *Chem. Rev.* **1988**, *88* (6), 899–926.

113. Mulder, W. H.; Párkányi, C. Theory of the Salt Effect on Solvatochromic Shifts And Its Potential Application to the Determination of Ground-State and Excited-State Dipole Moments. *J. Phys. Chem. A* **2002**, *106* (49), 11932–11937.

114. Lewis, N. H. C.; Iscen, A.; Felts, A.; Dereka, B.; Schatz, G. C.; Tokmakoff, A. Vibrational Probe of Aqueous Electrolytes: The Field Is Not Enough. *J. Phys. Chem. B* **2020**, *124* (32), 7013–7026.

115. Baiz, C. R.; Błasiak, B.; Bredenbeck, J.; Cho, M.; Choi, J.-H.; Corcelli, S. A.; Dijkstra, A. G.; Feng, C.-J.; Garrett-Roe, S.; Ge, N.-H.; Hanson-Heine, M. W. D.; Hirst, J. D.; Jansen, T. L. C.; Kwac, K.; Kubarych, K. J.; Londergan, C. H.; Maekawa, H.; Reppert, M.; Saito, S.; Roy, S.; Skinner, J. L.; Stock, G.; Straub, J. E.; Thielges, M. C.; Tominaga, K.; Tokmakoff, A.; Torii, H.; Wang, L.; Webb, L. J.; Zanni, M. T. Vibrational Spectroscopic Map, Vibrational Spectroscopy, and Intermolecular Interaction. *Chem. Rev.* **2020**, *120* (15), 7152–7218.

116. Harris, F. E.; O'Konski, C. T. Dielectric Properties of Aqueous Ionic Solutions at Microwave Frequencies. *J. Phys. Chem.* **1957**, *61* (3), 310–319.

117. Schneider, S. H.; Kratochvil, H. T.; Zanni, M. T.; Boxer, S. G. Solvent-Independent Anharmonicity for Carbonyl Oscillators. *J. Phys. Chem. B* **2017**, *121* (10), 2331–2338.

118. Hunt, N. T. 2D-IR Spectroscopy: Ultrafast Insights into Biomolecule Structure and Function. *Chem. Soc. Rev.* **2009**, *38* (7), 1837–1848.

119. Fayer, M. D. Dynamics of Liquids, Molecules, and Proteins Measured with Ultrafast 2D IR Vibrational Echo Chemical Exchange Spectroscopy. *Annu. Rev. Phys. Chem.* **2009**, *60* (1), 21–38.

120. Pluhařová, E.; Baer, M. D.; Mundy, C. J.; Schmidt, B.; Jungwirth, P. Aqueous Cation-Amide Binding: Free Energies and IR Spectral Signatures by Ab Initio Molecular Dynamics. *J. Phys. Chem. Lett.* **2014**, *5* (13), 2235–2240.

121. Shimanouchi, T. Tables of Molecular Vibrational Frequencies Consolidated Volume I. **1972**, 1–160.

122. Choi, J.-H.; Oh, K.-I.; Lee, H.; Lee, C.; Cho, M. Nitrile and Thiocyanate IR Probes: Quantum Chemistry Calculation Studies and Multivariate Least-Square Fitting Analysis. *J. Chem. Phys.* **2008**, *128* (13), 134506.

123. First, J. T.; Novelli, E. T.; Webb, L. J. Beyond PKa: Experiments and Simulations of Nitrile Vibrational Probes in Staphylococcal Nuclease Show the Importance of Local Interactions. *J. Phys. Chem. B* **2020**, *124* (16), 3387–3399.

124. Haskard, C. A.; Li-Chan, E. C. Y. Hydrophobicity of Bovine Serum Albumin and Ovalbumin Determined Using Uncharged (PRODAN) and Anionic (ANS-) Fluorescent Probes. *J. Agric. Food Chem.* **1998**, *46* (7), 2671–2677.

125. Krasnowska, E. K.; Gratton, E.; Parasassi, T. Prodan as a Membrane Surface Fluorescence Probe: Partitioning between Water and Phospholipid Phases. *Biophysical Journal* **1998**, *74* (4), 1984–1993.

126. Vequi-Suplicy, C. C.; Coutinho, K.; Lamy, M. T. Optical Characterization of Prodan Aggregates in Water Medium. *Phys. Chem. Chem. Phys.* **2013**, *15* (28), 11800–11807.

127. Kashid, S. M.; Singh, R. K.; Kwon, H.; Kim, Y. S.; Mukherjee, A.; Bagchi, S. Arresting an Unusual Amide Tautomer Using Divalent Cations. *J. Phys. Chem. B* **2019**, *123* (40), 8419–8424.

128. Cracchiolo, O. M.; Geremia, D. K.; Corcelli, S. A.; Serrano, A. L. Hydrogen Bond Exchange and Ca2+ Binding of Aqueous N-Methylacetamide Revealed by 2DIR Spectroscopy. *J. Phys. Chem. B* **2020**, *124* (32), 6947–6954.

129. Pegram, L. M.; Record, M. T. Hofmeister Salt Effects on Surface Tension Arise from Partitioning of Anions and Cations between Bulk Water and the Air−Water Interface. *J. Phys. Chem. B* **2007**, *111* (19), 5411–5417.

130. Traube, J. The Attraction Pressure. *J. Phys. Chem.* **1910**, *14* (5), 452–470.

131. Denton, J. K.; Kelleher, P. J.; Johnson, M. A.; Baer, M. D.; Kathmann, S. M.; Mundy, C. J.; Rudd, B. A. W.; Allen, H. C.; Choi, T. H.; Jordan, K. D. Molecular-Level Origin of the Carboxylate Head Group Response to Divalent Metal Ion Complexation at the Air–Water Interface. *PNAS* **2019**, *116* (30), 14874–14880.

132. Zhang, T.; Brantley, S. L.; Verreault, D.; Dhankani, R.; Corcelli, S. A.; Allen, H. C. Effect of PH and Salt on Surface PKa of Phosphatidic Acid Monolayers. *Langmuir* **2018**, *34* (1), 530–539.

133. Götte, L.; Parry, K. M.; Hua, W.; Verreault, D.; Allen, H. C.; Tobias, D. J. Solvent-Shared Ion Pairs at the Air–Solution Interface of Magnesium Chloride and Sulfate Solutions Revealed by Sum Frequency Spectroscopy and Molecular Dynamics Simulations. *J. Phys. Chem. A* **2017**, *121* (34), 6450–6459.

134. Post, S. T. van der; Bakker, H. J. The Combined Effect of Cations and Anions on the Dynamics of Water. *Phys. Chem. Chem. Phys.* **2012**, *14* (18), 6280–6288.

135. Pastorczak, M.; Post, S. T. van der; Bakker, H. J. Cooperative Hydration of Carboxylate Groups with Alkali Cations. *Phys. Chem. Chem. Phys.* **2013**, *15* (41), 17767–17770.

136. Nihonyanagi, S.; Yamaguchi, S.; Tahara, T. Counterion Effect on Interfacial Water at Charged Interfaces and Its Relevance to the Hofmeister Series. *J. Am. Chem. Soc.* **2014**, *136* (17), 6155–6158.

137. Cruz-León, S.; Schwierz, N. Hofmeister Series for Metal-Cation–RNA Interactions: The Interplay of Binding Affinity and Exchange Kinetics. *Langmuir* **2020**, *36* (21), 5979–5989.

138. Lin, L.; Husek, J.; Biswas, S.; Baumler, S. M.; Adel, T.; Ng, K. C.; Baker, L. R.; Allen, H. C. Iron(III) Speciation Observed at Aqueous and Glycerol Surfaces: Vibrational Sum Frequency and X-Ray. *J. Am. Chem. Soc.* **2019**, *141* (34), 13525–13535.

139. Baumler, S. M.; V, W. H. H.; Allen, H. C. Hydration of Ferric Chloride and Nitrate in Aqueous Solutions: Water-Mediated Ion Pairing Revealed by Raman Spectroscopy. *Phys. Chem. Chem. Phys.* **2019**, *21* (35), 19172–19180.

140. Lutter, J. C.; Wu, T.; Zhang, Y. Hydration of Cations: A Key to Understanding of Specific Cation Effects on Aggregation Behaviors of PEO-PPO-PEO Triblock Copolymers. *J. Phys. Chem. B* **2013**, *117* (35), 10132–10141.

141. Zanotti-Gerosa, A.; Solari, E.; Giannini, L.; Floriani, C.; Chiesi-Villa, A.; Rizzoli, C. Shaping the Cavity of Calix[4]Arene Using Transition Metals and Binding Alkali-Metal Cations inside the Cavity: The Relevance of the Alkali-Metal Cation–Arene Interaction. *Chemical Communications* **1997**, *0* (2), 183–184.

142. D, M. de O.; Sr, Z.; V, P.; J, H.; H, M.-S.; D, B.-A.; P, J.; E, D.-D. Binding of Divalent Cations to Acetate: Molecular Simulations Guided by Raman Spectroscopy. *Phys Chem Chem Phys* **2020**, *22* (41), 24014–24027.

143. Asthagiri, D.; Pratt, L. R.; Paulaitis, M. E.; Rempe, S. B. Hydration Structure and Free Energy of Biomolecularly Specific Aqueous Dications, Including Zn^{2+} and First Transition Row Metals. *J. Am. Chem. Soc.* **2004**, *126* (4), 1285–1289.

144. Marino, T.; Toscano, M.; Russo, N.; Grand, A. Structural and Electronic Characterization of the Complexes Obtained by the Interaction between Bare and Hydrated First-Row Transition-Metal Ions (Mn^{2+}, Fe^{2+}, Co^{2+}, Ni^{2+}, Cu^{2+}, Zn^{2+}) and Glycine. *J. Phys. Chem. B* **2006**, *110* (48), 24666–24673.

145. Anderson, W. P.; Edwards, W. D.; Zerner, M. C. Calculated Spectra of Hydrated Ions of the First Transition-Metal Series. *Inorg. Chem.* **1986**, *25* (16), 2728–2732.

146. Walrafen, G. E.; Fisher, M. R.; Hokmabadi, M. S.; Yang, W.-H. Temperature Dependence of the Low- and High-frequency Raman Scattering from Liquid Water. *J. Chem. Phys.* **1998**, *85* (12), 6970.

147. Walrafen, G. E. Raman Spectral Studies of the Effects of Temperature on Water Structure. *J. Chem. Phys.* **1967**, *47* (1), 114–126.

148. Morawietz, T.; Marsalek, O.; Pattenaude, S. R.; Streacker, L. M.; Ben-Amotz, D.; Markland, T. E. The Interplay of Structure and Dynamics in the Raman Spectrum of Liquid Water over the Full Frequency and Temperature Range. *J. Phys. Chem. Lett.* **2018**, *9* (4), 851–857.

149. Patra, A.; Roy, S.; Saha, S.; Palit, D. K.; Mondal, J. A. Observation of Extremely Weakly Interacting OH (~ 3600 cm^{-1}) in the Vicinity of High Charge Density Metal Ions (M^{z+}; z = 1, 2, 3): A Structural Heterogeneity in the Extended Hydration Shell. *J. Phys. Chem. C* **2020**, *124* (5), 3028–3036.

150. Roy, S.; Patra, A.; Saha, S.; Palit, D. K.; Mondal, J. A. Restructuring of Hydration Shell Water Due to Solvent-Shared Ion Pairing (SSIP): A Case Study of Aqueous $MgCl_2$ and $LaCl_2$ Solutions. *J. Phys. Chem. B* **2020**, *124* (37), 8141–8148.

151. Chaffey, N. Alberts, B., Johnson, A., Lewis, J., Raff, M., Roberts, K. and Walter, P. Molecular biology of the cell. 4th edn. *Annals of Botany* **2003,** *91* (3), 401-401.

152. Zaera, F. Probing Liquid/Solid Interfaces at the Molecular Level. *Chemical Reviews* **2012,** *112* (5), 2920-2986.

153. Bain, C. D. Studies of adsorption at interfaces by optical techniques: Ellipsometry, second harmonic generation and sum-frequency generation. *Current Opinion in Colloid & Interface Science* **1998,** *3* (3), 287-292.

154. Miranda, P. B.; Shen, Y. R. Liquid Interfaces: A Study by Sum-Frequency Vibrational Spectroscopy. *The Journal of Physical Chemistry B* **1999,** *103* (17), 3292-3307.

155. Perera, P. N.; Fega, K. R.; Lawrence, C.; Sundstrom, E. J.; Tomlinson-Phillips, J.; Ben-Amotz, D. Observation of water dangling OH bonds around dissolved nonpolar groups. *Proceedings of the National Academy of Sciences* **2009,** *106* (30), 12230-12234.

156. Petersen, P. B.; Johnson, J. C.; Knutsen, K. P.; Saykally, R. J. Direct experimental validation of the Jones–Ray effect. *Chemical Physics Letters* **2004,** *397* (1), 46-50.

157. Jungwirth, P.; Tobias, D. J. Specific Ion Effects at the Air/Water Interface. *Chemical Reviews* **2006,** *106* (4), 1259-1281.

158. Adamson, A. W.; Gast, A. P. *Physical chemistry of surfaces*. Wiley-interscience: Sidney, 1997.

159. Henry, C. L.; Parkinson, L.; Ralston, J. R.; Craig, V. S. J. A Mobile Gas−Water Interface in Electrolyte Solutions. *The Journal of Physical Chemistry C* **2008,** *112* (39), 15094-15097.

160. Long, F. A.; Nutting, G. C. The Relative Surface Tension of Potassium Chloride Solutions by a Differential Bubble Pressure Method1. *Journal of the American Chemical Society* **1942,** *64* (10), 2476-2482.

161. Petersen, P. B.; Saykally, R. J. Adsorption of Ions to the Surface of Dilute Electrolyte Solutions: The Jones−Ray Effect Revisited. *Journal of the American Chemical Society* **2005,** *127* (44), 15446-15452.

162. Passoth, G. Uber den Jones-Ray-effekt und die Oberflächenspannung verdünnter elektrolytlosungen. *Z. Physik. Chem* **1959,** *211*, 129.

163. Priester, T.; Bartoszek, M.; Lunkenheimer, K. Influence of Surface-Active Trace Impurities on the Surface Properties of Aqueous Solutions of Oligoethylene Glycol Monooctyl Ethers. *Journal of Colloid and Interface Science* **1998,** *208* (1), 6-13.

164. Rosen, M. J. Purification of surfactants for studies of their fundamental surface properties. *Journal of Colloid and Interface Science* **1981,** *79* (2), 587-588.

165. Miles, G. D.; Shedlovsky, L. Minima in Surface Tension–Concentration Curves of Solutions of Sodium Alcohol Sulfates. *The Journal of Physical Chemistry* **1944,** *48* (1), 57-62.

166. Ward, R. N.; Davies, P. B.; Bain, C. D. Coadsorption of Sodium Dodecyl Sulfate and Dodecanol at a Hydrophobic Surface. *The Journal of Physical Chemistry B* **1997,** *101* (9), 1594-1601.

167. Timothy, D.; Marcel, B.; Christopher, M. *Surfactant Impurities Can Explain the Jones-Ray Effect*. 2018.

168. Uematsu, Y.; Bonthuis, D. J.; Netz, R. R. Charged Surface-Active Impurities at Nanomolar Concentration Induce Jones–Ray Effect. *The Journal of Physical Chemistry Letters* **2018,** *9* (1), 189-193.

169. Jones, G.; Ray, W. A. The surface tension of solutions of electrolytes as a function of the concentration I A differential method for measuring relative surface tension. *Journal of the American Chemical Society* **1937,** *59*, 187-198.

170. Chen, Y.; Okur, H. I.; Gomopoulos, N.; Macias-Romero, C.; Cremer, P. S.; Petersen, P. B.; Tocci, G.; Wilkins, D. M.; Liang, C.; Ceriotti, M.; Roke, S. Electrolytes induce long-range orientational order and free energy changes in the H-bond network of bulk water. *Science Advances* **2016,** *2* (4).

171. Okur, H. I.; Chen, Y.; Wilkins, D. M.; Roke, S. The Jones-Ray effect reinterpreted: Surface tension minima of low ionic strength electrolyte solutions are caused by electric field induced water-water correlations. *Chemical Physics Letters* **2017,** *684*, 433-442.

172. Beattie, J. K.; Djerdjev, A. M.; Gray-Weale, A.; Kallay, N.; Lützenkirchen, J.; Preočanin, T.; Selmani, A. pH and the surface tension of water. *Journal of Colloid and Interface Science* **2014,** *422*, 54-57.

173. Wilkins, D. M.; Manolopoulos, D. E.; Roke, S.; Ceriotti, M. Communication: Mean-field theory of water-water correlations in electrolyte solutions. *The Journal of Chemical Physics* **2017,** *146* (18), 181103.

174. Gaines, G. L. *Insoluble monolayers at liquid-gas interfaces*. Wiley (Interscience) New York, 1966.

175. Lunkenheimer, K.; Pergande, H. J.; Krüger, H. Apparatus for programmed high-performance purification of surfactant solutions. *Review of Scientific Instruments* **1987,** *58* (12), 2313-2316.

Appendix A

EFFECTIVE DIFFUSION CONSTANTS OF CESIUM HYDROXIDE AND HYDROCHLORIC ACID

Herein we provide the measured effective diffusion constant of CsOH and LiOH which we determined using the Nerst-Einstein equation, and compare this to the literature value of HCl (Table **A-1**).

Table **A-1**: Effective diffusion constants of LiOH, CsOH and HCl of 10 mM aqueous salts (10^{-5} cm^2/s) at 298 K.[45-47]

LiOH	5.2
CsOH	7.2
HCl	9.3

As the concentration of CsOH is decreased to 1 mM, the conductivity of the solution increases. As such, the effective diffusion constant of ions in solution increases to ~ $8.1*10^{-5}$ cm^2/s as calculated from the Nernst-Einstein relationship. This matches well that of HCl, which points to the potential ability to improve performance of alkali fuel cells by considering ion pairing.[45-47]

Appendix B

SPECTRAL LIBRARY FOR CHAPTER 3

Herein we provide normalized ATR-FTIR spectra of carbonyl stretching modes in acetone, *N*-methylacetamide (NMA) and *N*,*N*-dimethylacetamide (DMA) as a function of salt concentration and identity. Furthermore, this is done with Raman spectra of the C≡N mode for solutions containing acetonitrile. The library is provided in this Appendix.

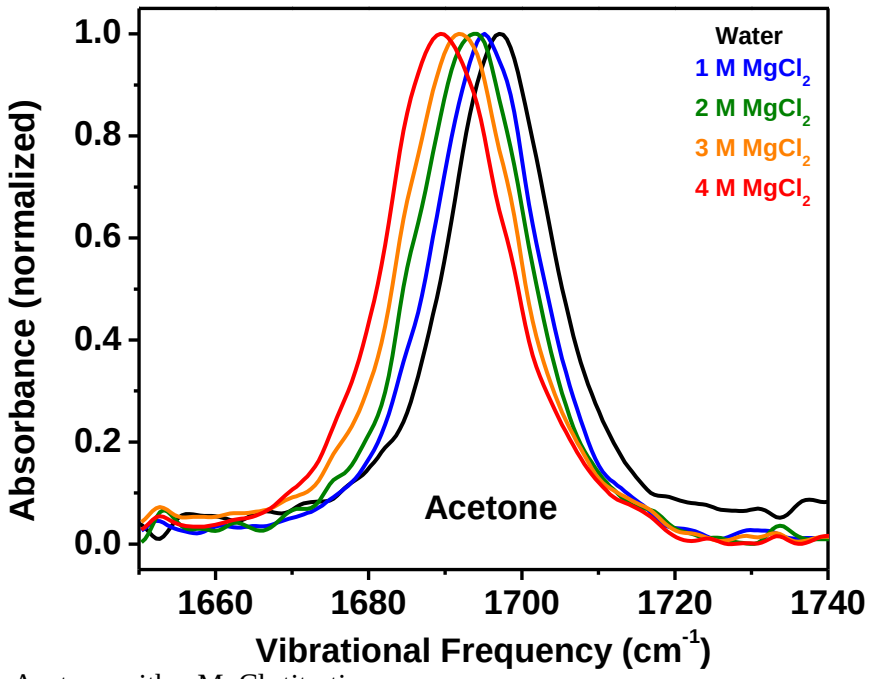

Figure **B-1**: Acetone with a $MgCl_2$ titration.

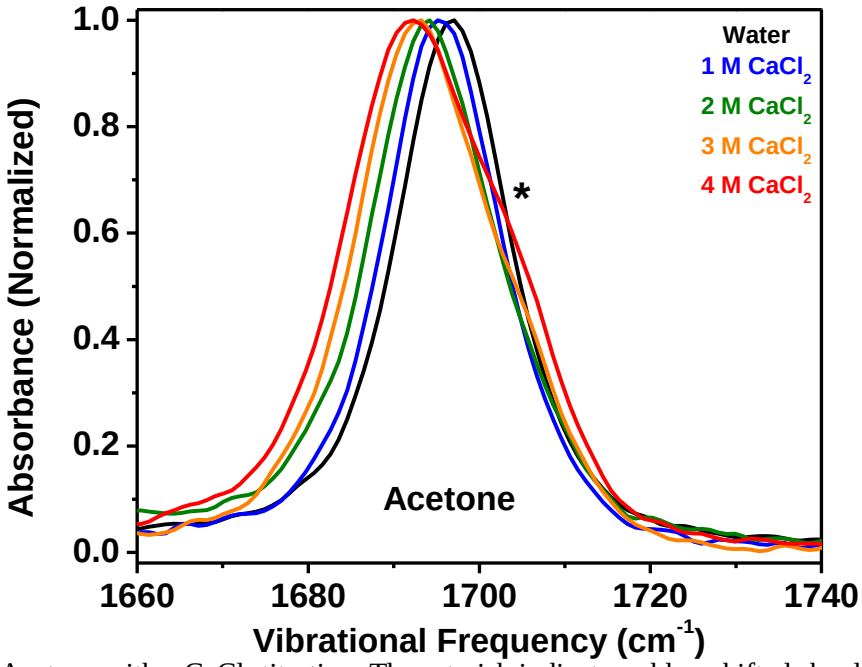

Figure **B-2**: Acetone with a $CaCl_2$ titration. The asterisk indicates a blue-shifted shoulder.

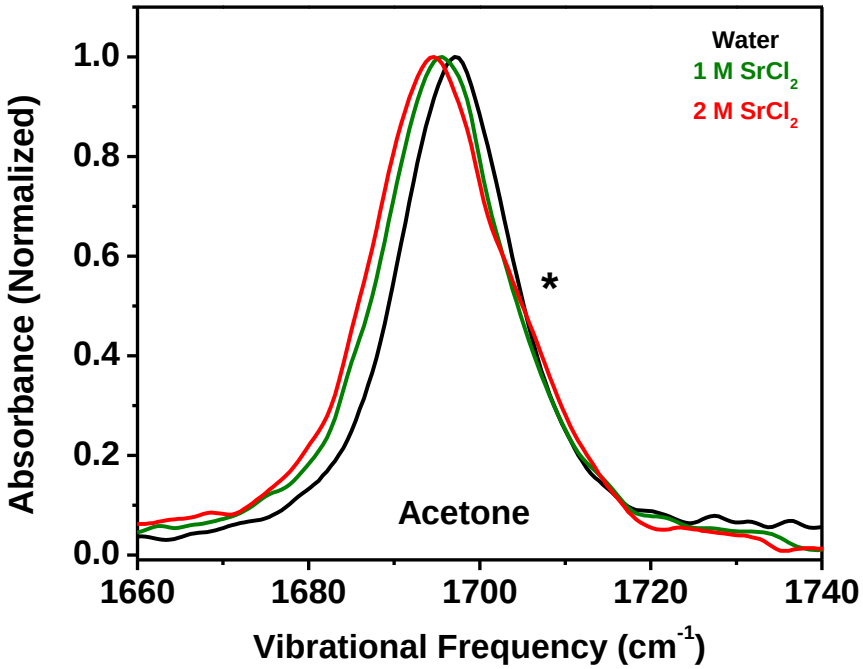

Figure **B-3**: Acetone with a $SrCl_2$ titration. The asterisk indicates a blue-shifted shoulder.

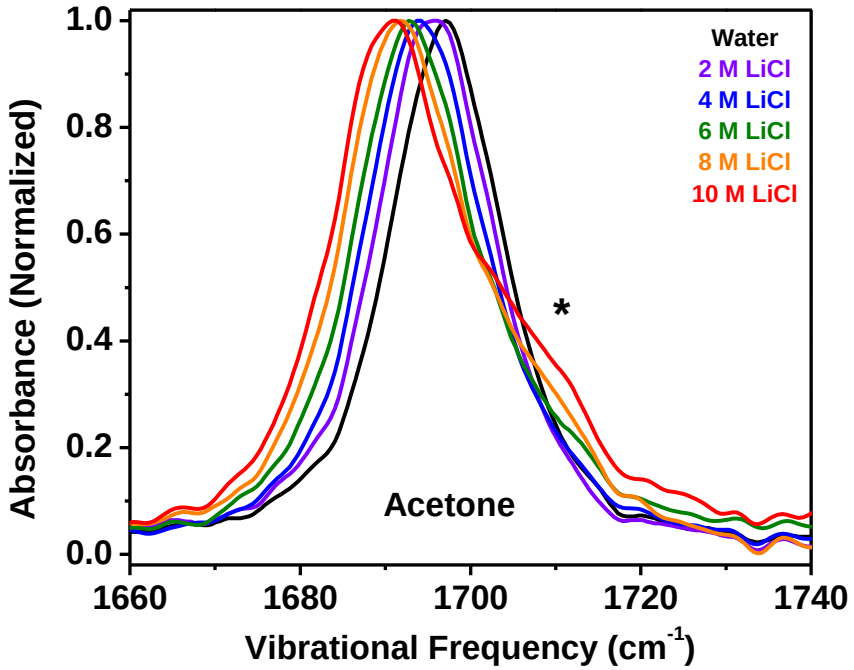

Figure **B-4**: Acetone with a LiCl titration. The asterisk indicates a blue-shifted shoulder.

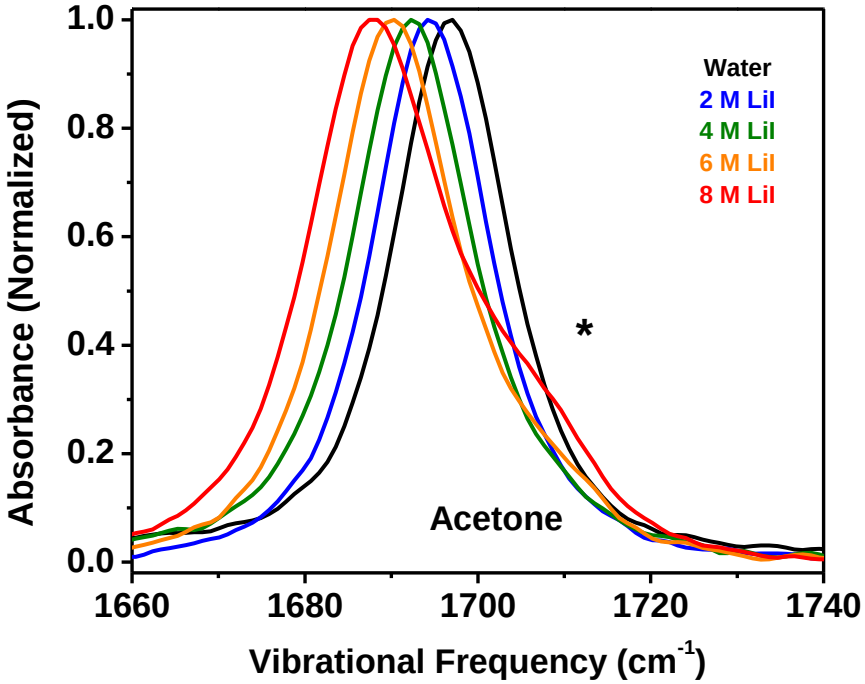

Figure **B-5**: Acetone with a LiI titration. The asterisk indicates a blue-shifted shoulder.

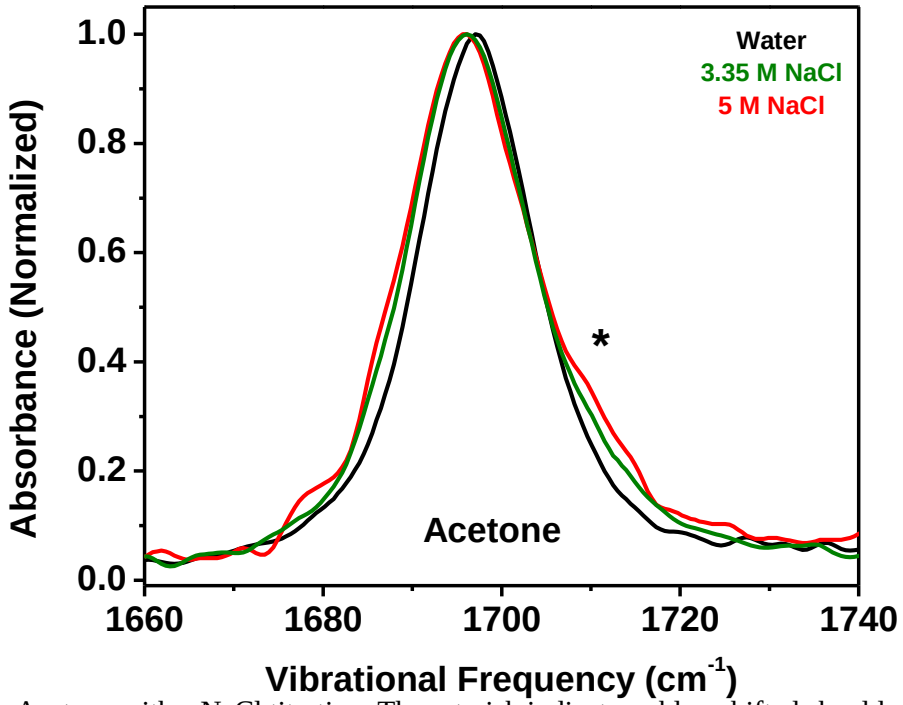

Figure **B-6**: Acetone with a NaCl titration. The asterisk indicates a blue-shifted shoulder.

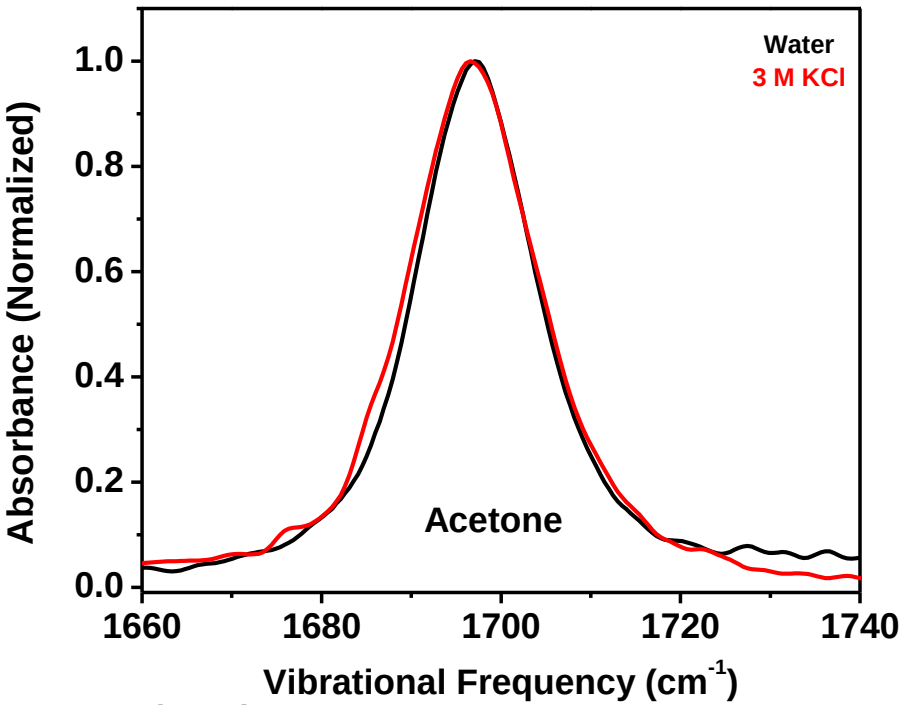

Figure **B-7**: Acetone with a KCl titration.

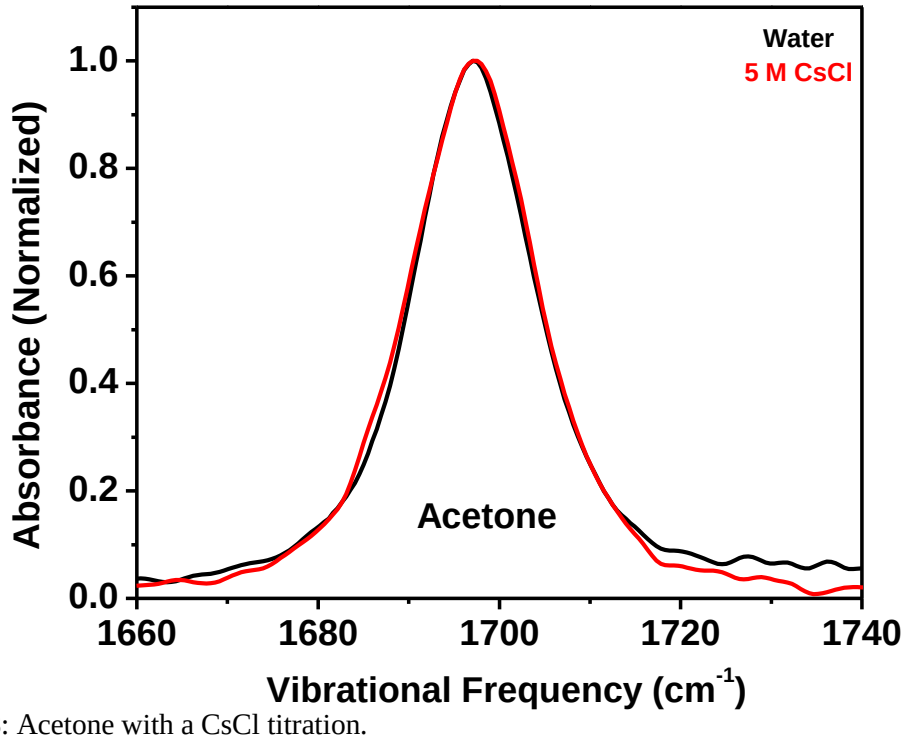

Figure **B-8**: Acetone with a CsCl titration.

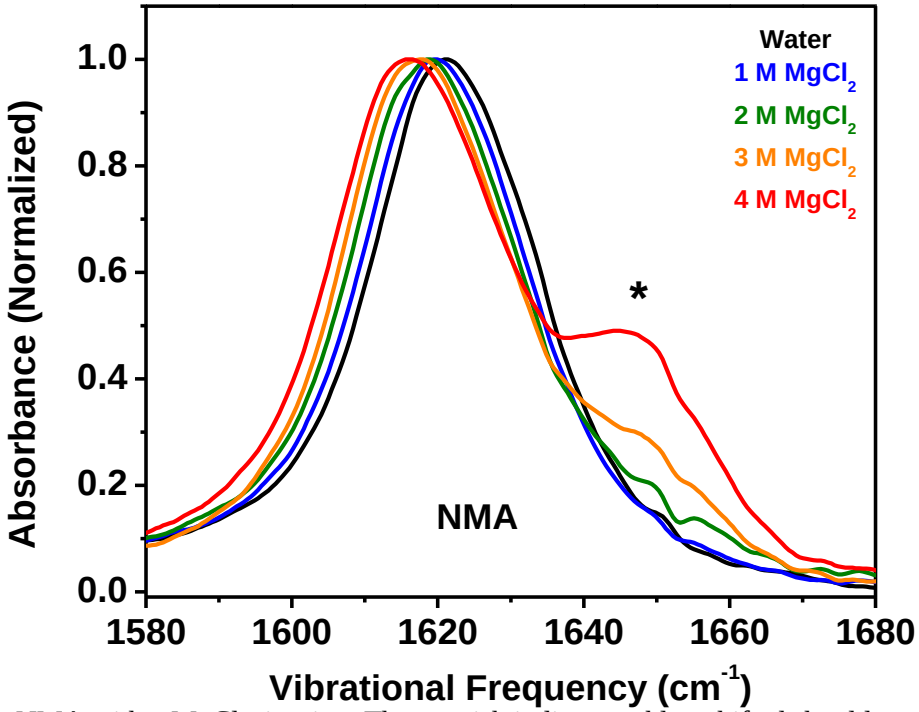

Figure **B-9**: NMA with a $MgCl_2$ titration. The asterisk indicates a blue-shifted shoulder.

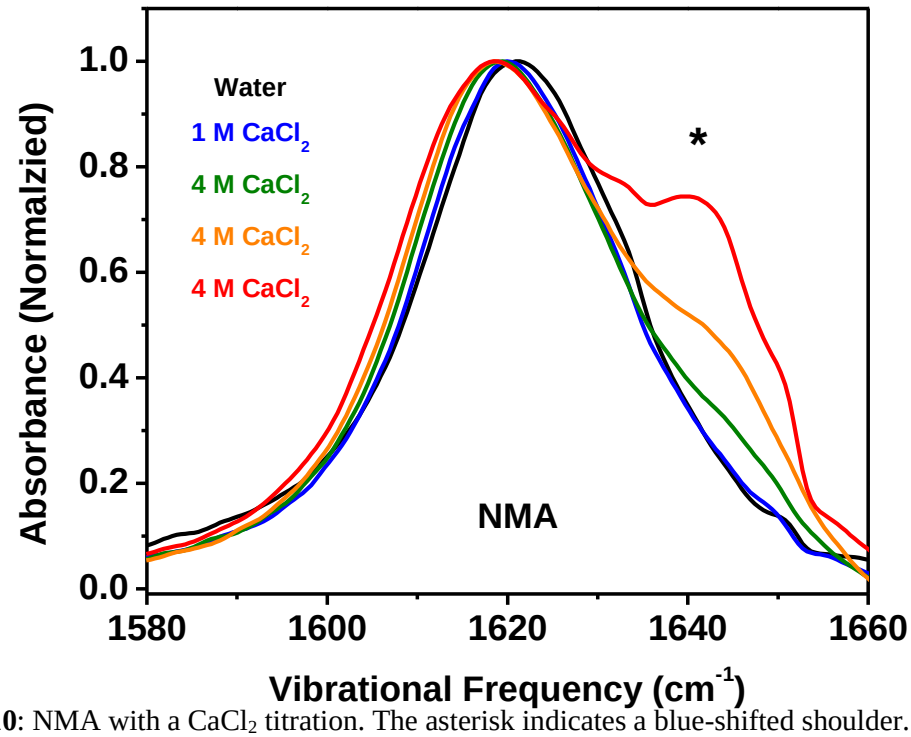

Figure **B-10**: NMA with a $CaCl_2$ titration. The asterisk indicates a blue-shifted shoulder.

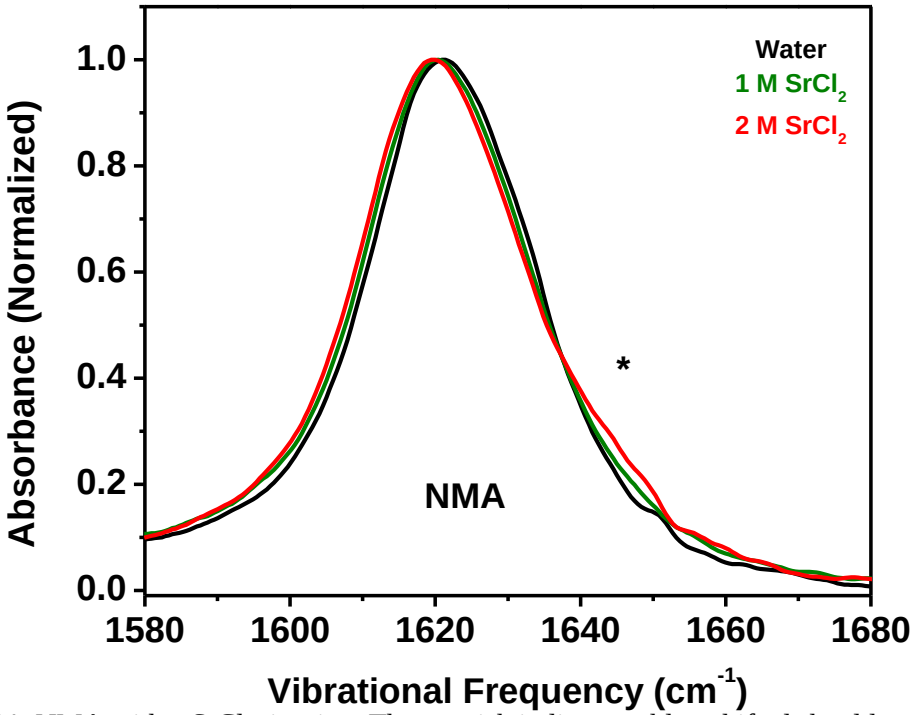

Figure **B-11**: NMA with a $SrCl_2$ titration. The asterisk indicates a blue-shifted shoulder.

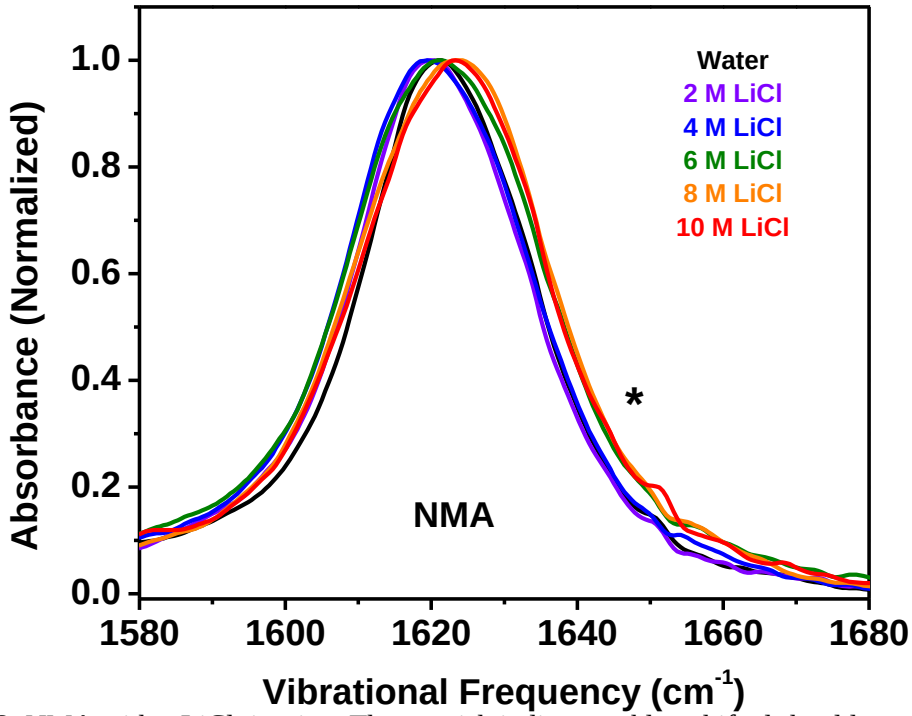

Figure **B-12**: NMA with a LiCl titration. The asterisk indicates a blue-shifted shoulder.

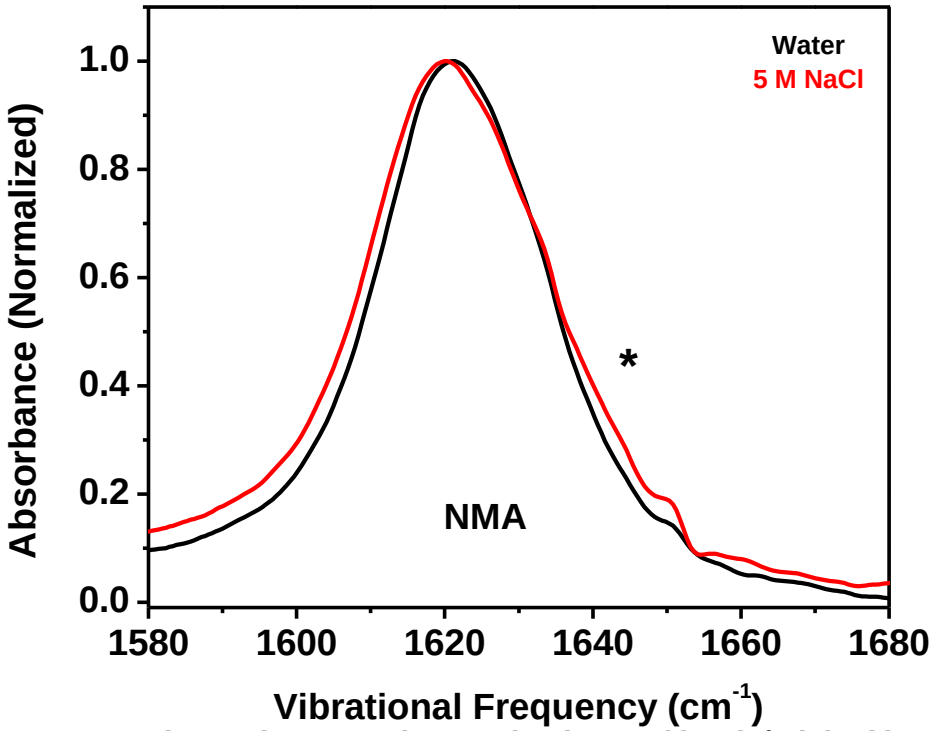

Figure **B-13**: NMA with a NaCl titration. The asterisk indicates a blue-shifted shoulder.

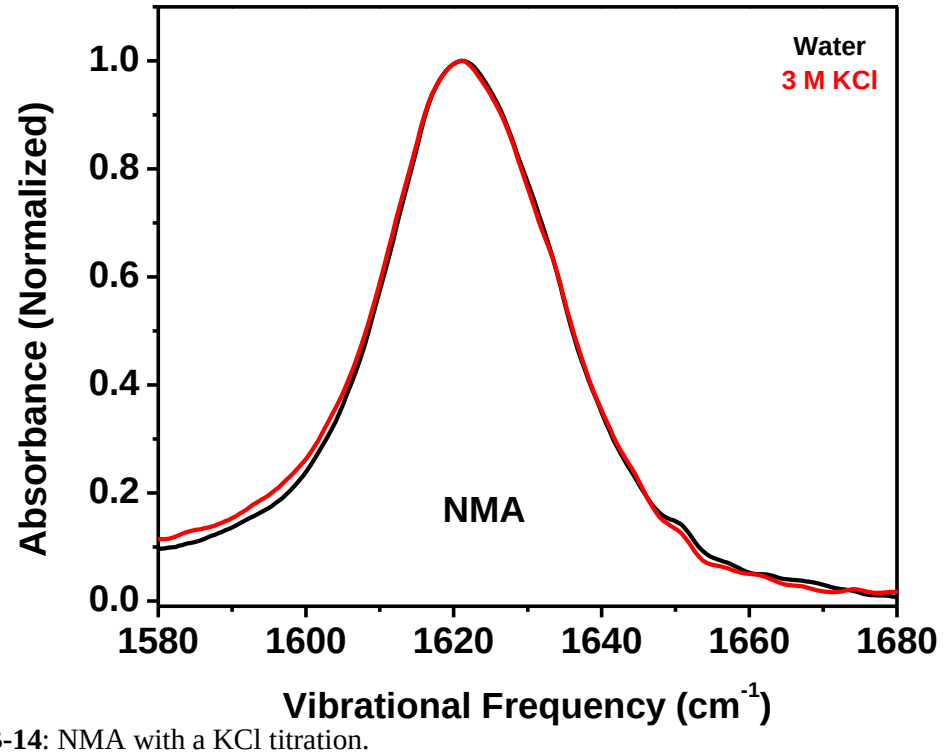

Figure **B-14**: NMA with a KCl titration.

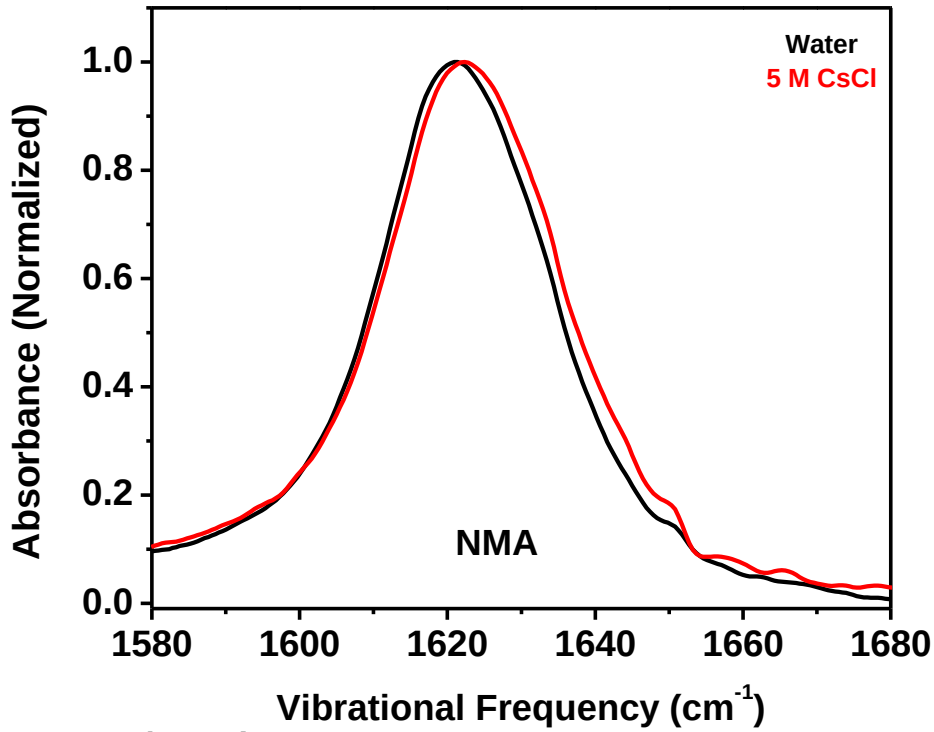

Figure **B-15**: NMA with a CsCl titration.

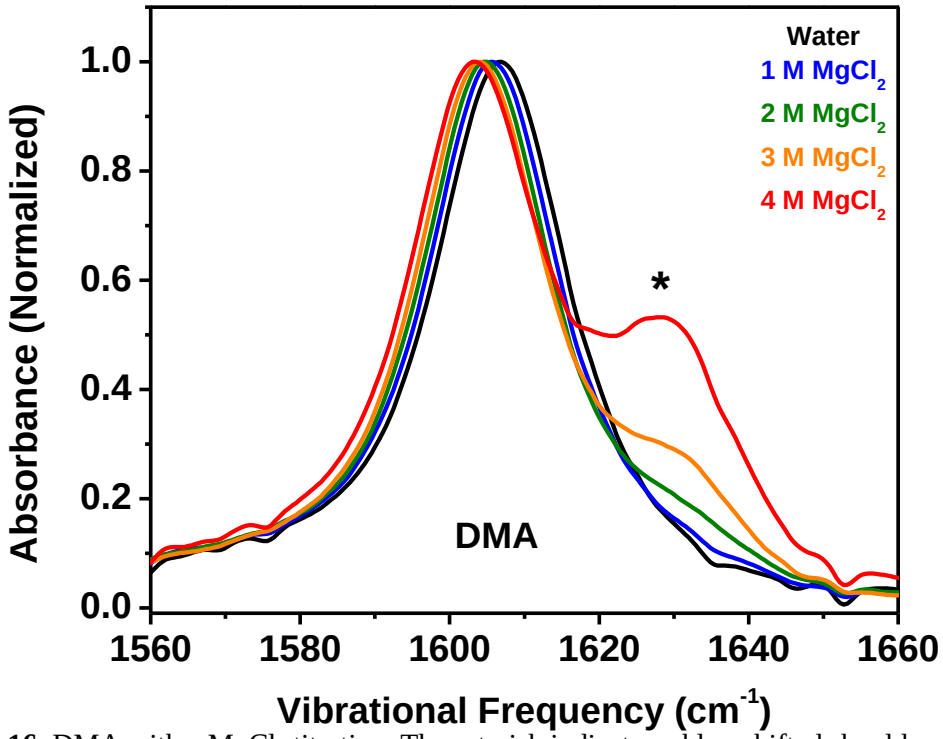

Figure **B-16**: DMA with a $MgCl_2$ titration. The asterisk indicates a blue-shifted shoulder.

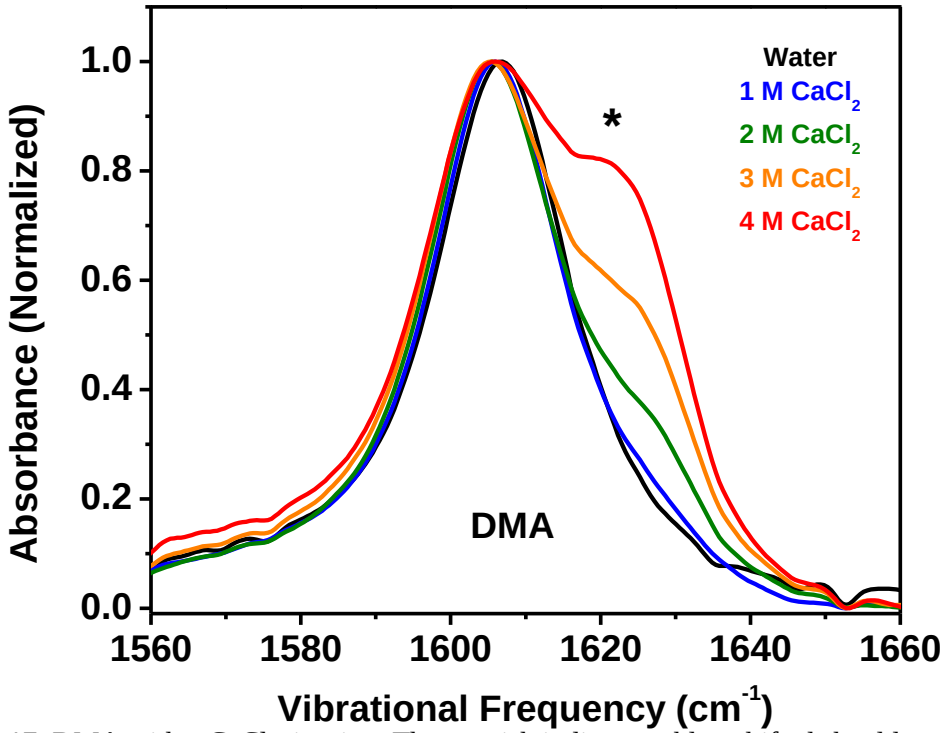

Figure **B-17**: DMA with a $CaCl_2$ titration. The asterisk indicates a blue-shifted shoulder.

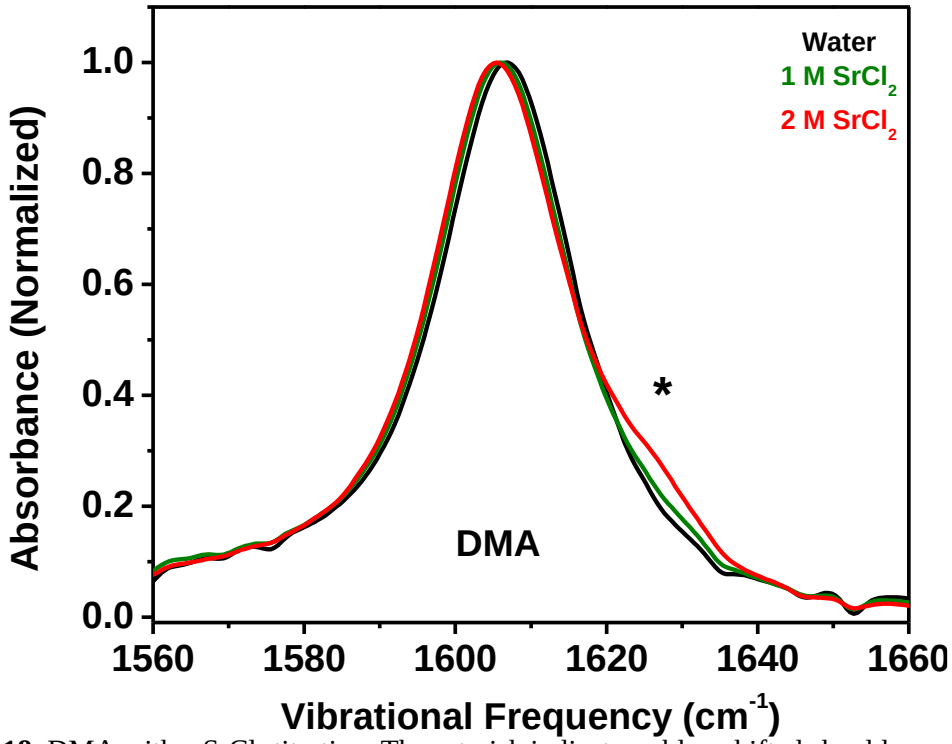

Figure **B-18**: DMA with a $SrCl_2$ titration. The asterisk indicates a blue-shifted shoulder.

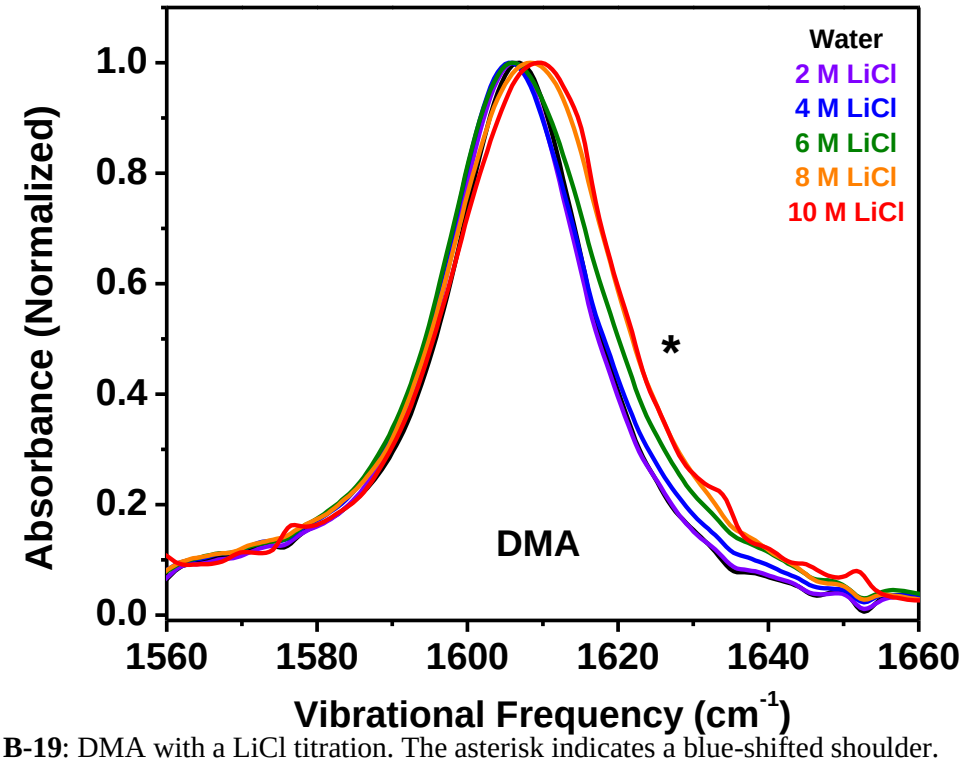

Figure **B-19**: DMA with a LiCl titration. The asterisk indicates a blue-shifted shoulder.

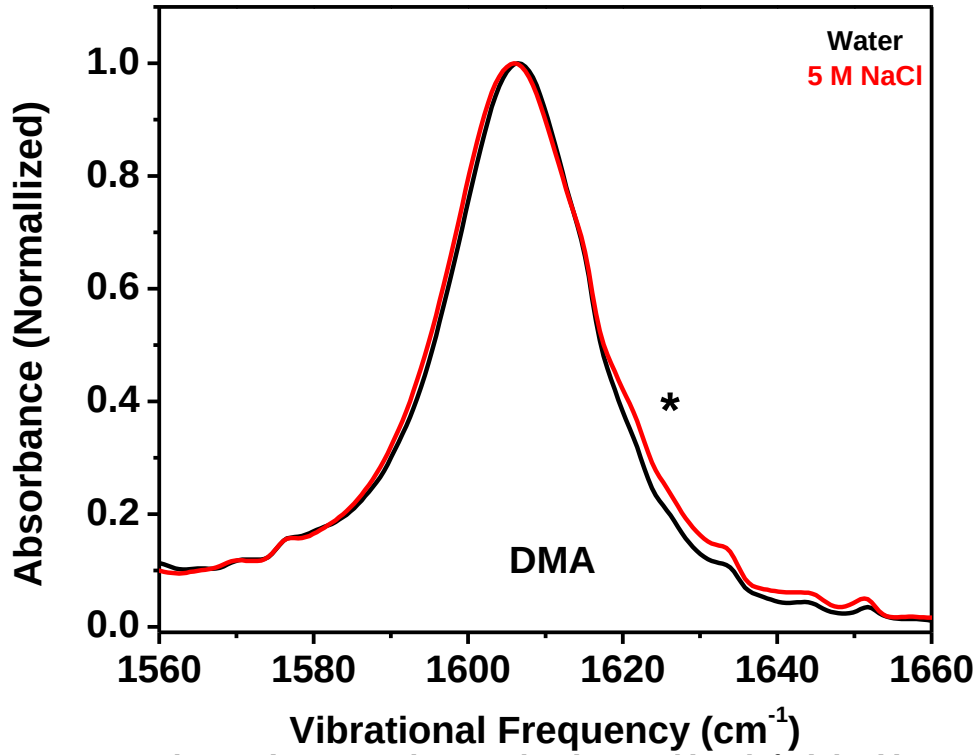

Figure **B-20**: DMA with a NaCl titration. The asterisk indicates a blue-shifted shoulder.

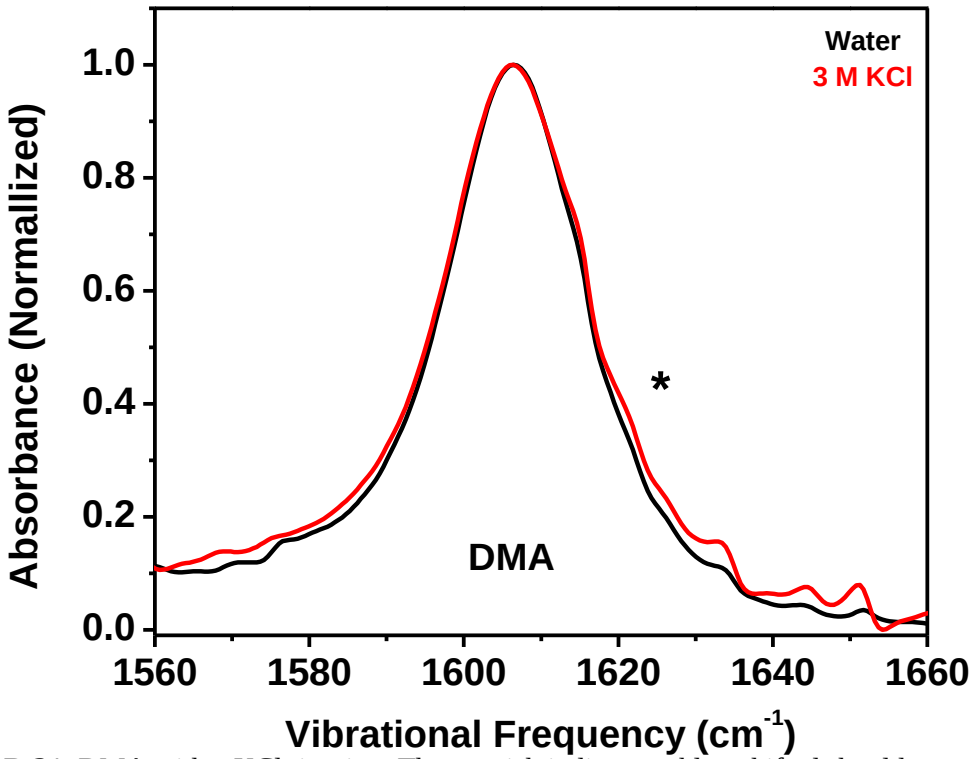

Figure **B-21**: DMA with a KCl titration. The asterisk indicates a blue-shifted shoulder.

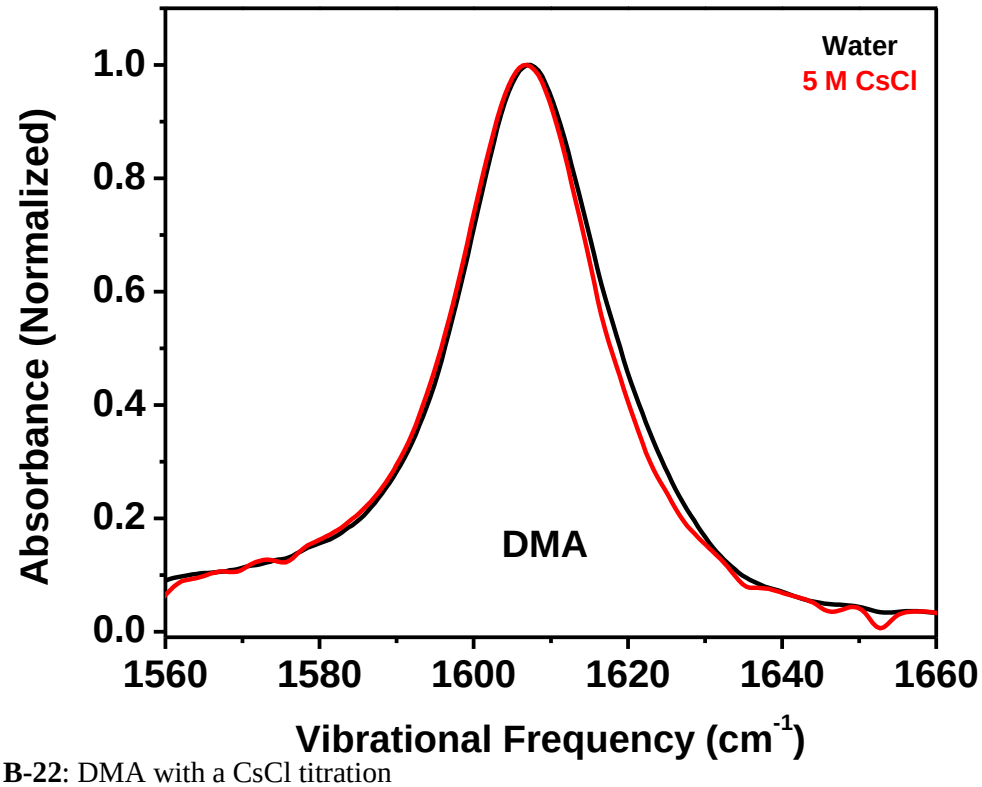

Figure **B-22**: DMA with a CsCl titration

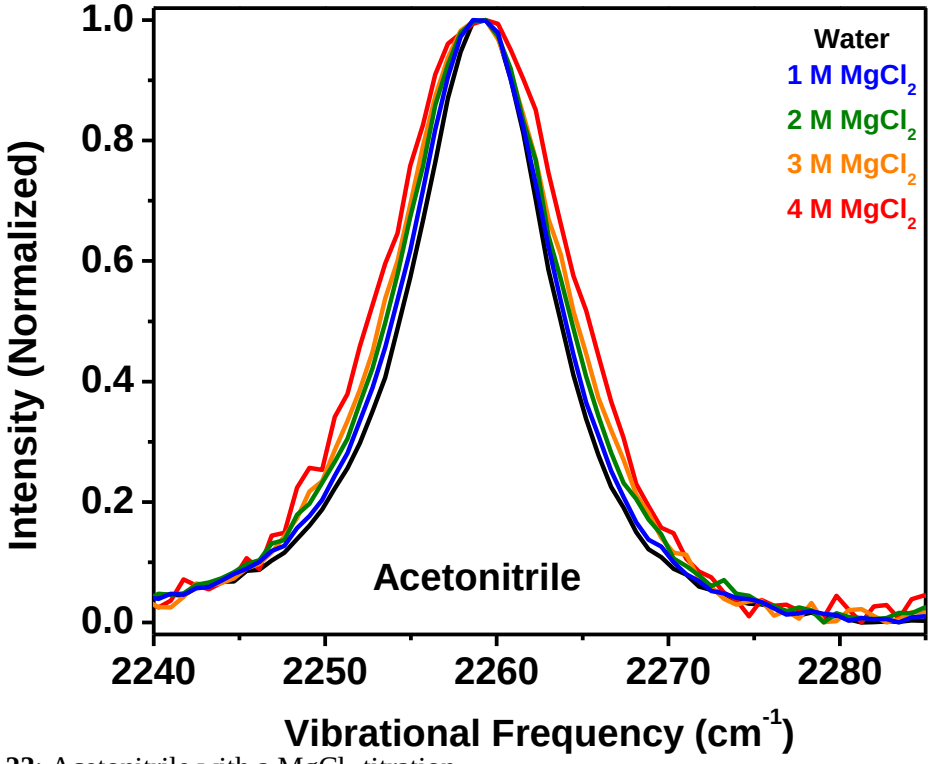

Figure **B-23**: Acetonitrile with a $MgCl_2$ titration.

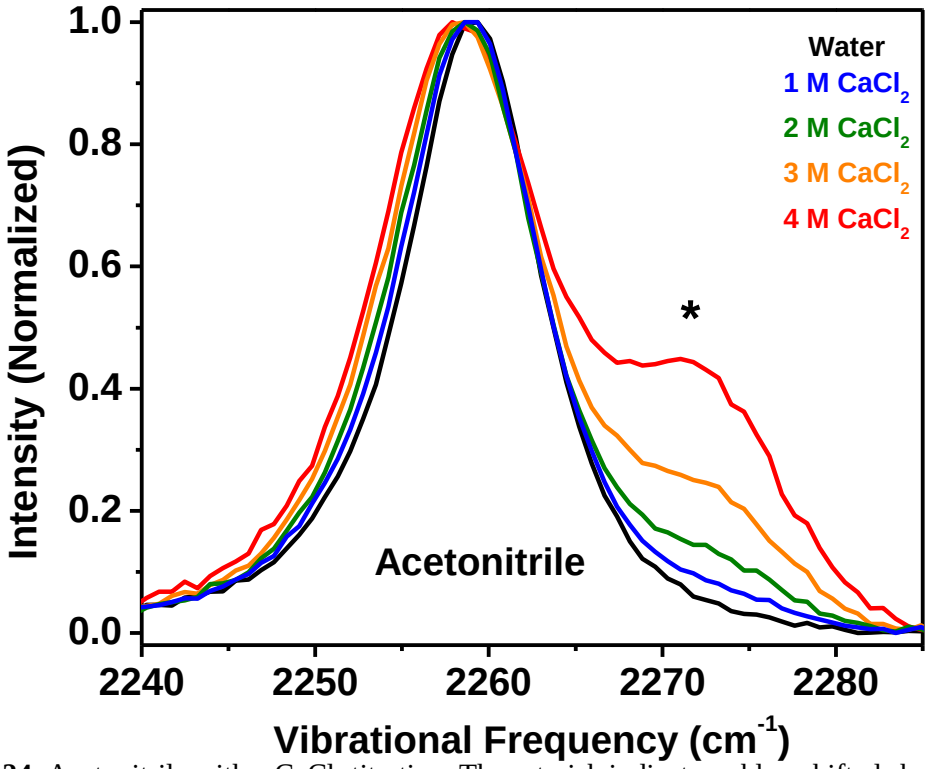

Figure **B-24**: Acetonitrile with a $CaCl_2$ titration. The asterisk indicates a blue-shifted shoulder.

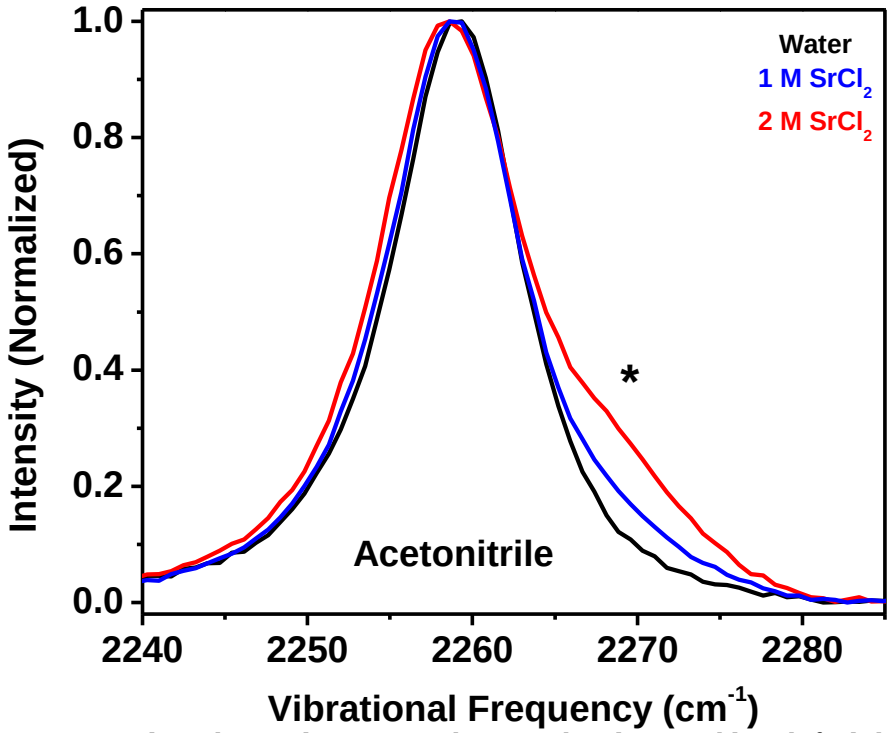

Figure **B-25**: Acetonitrile with a $SrCl_2$ titration. The asterisk indicates a blue-shifted shoulder.

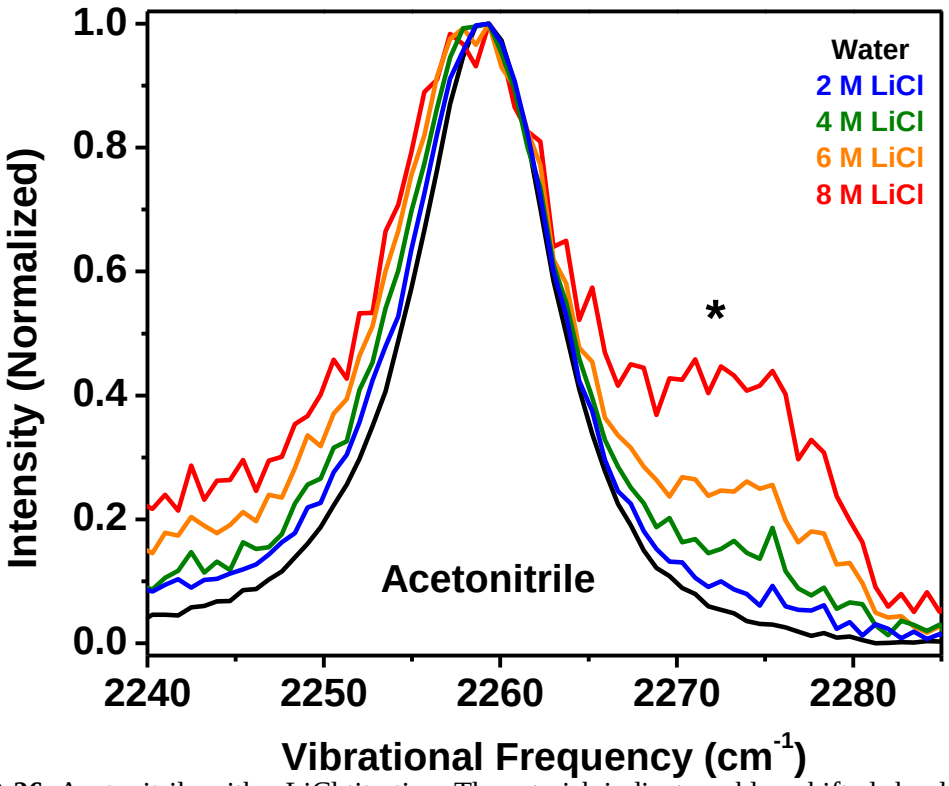

Figure **B-26**: Acetonitrile with a LiCl titration. The asterisk indicates a blue-shifted shoulder.

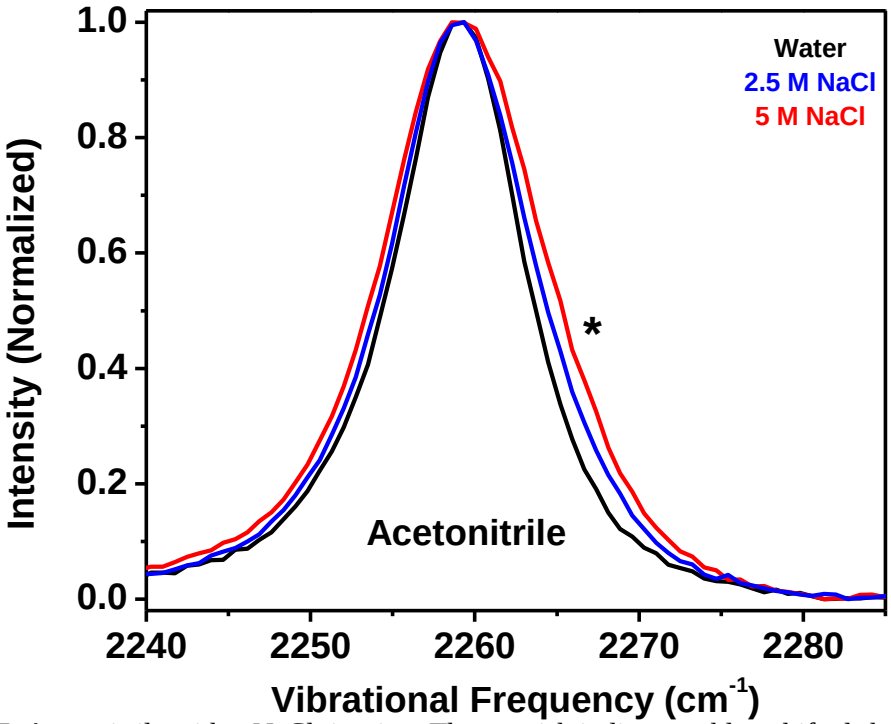

Figure **B-27**: Acetonitrile with a NaCl titration. The asterisk indicates a blue-shifted shoulder.

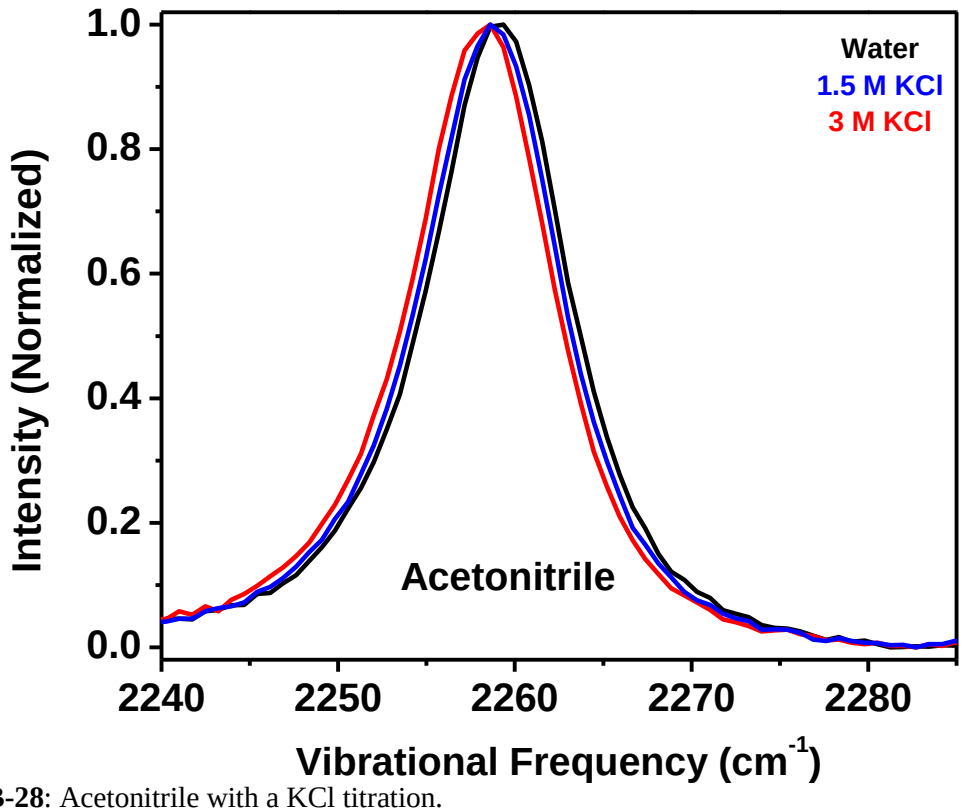

Figure **B-28**: Acetonitrile with a KCl titration.

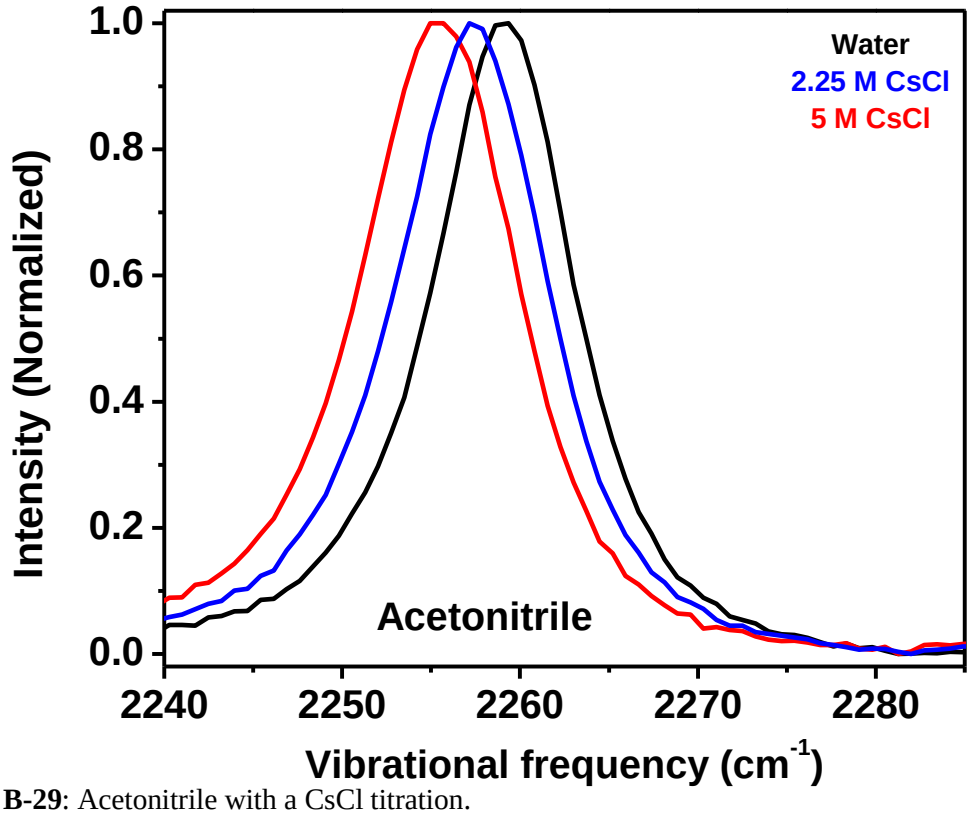

Figure **B-29**: Acetonitrile with a CsCl titration.

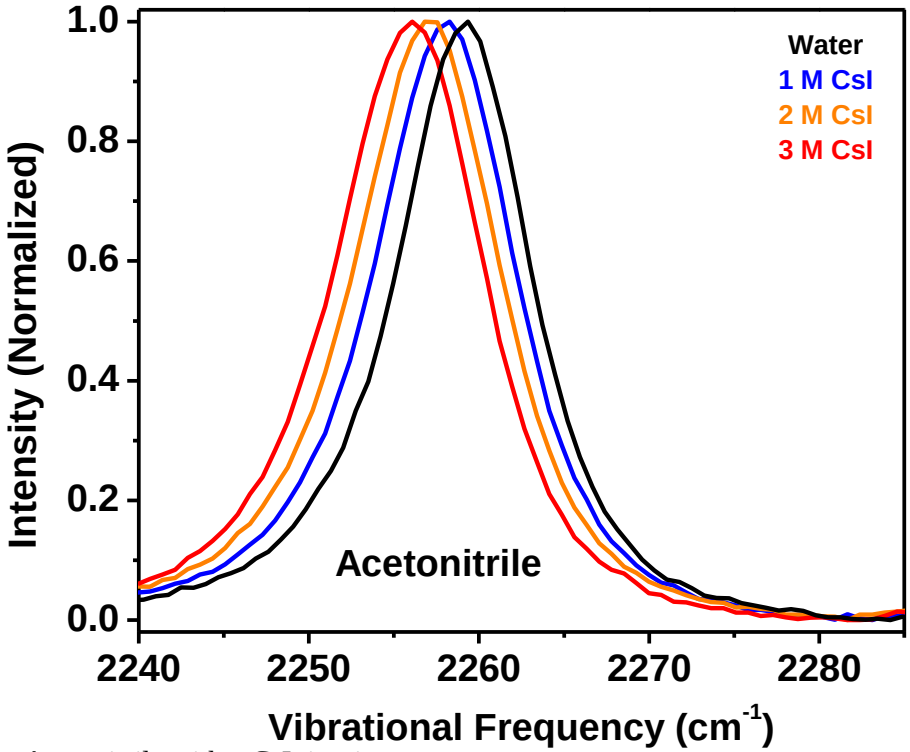

Figure **B-30**: Acetonitrile with a CsI titration.

Appendix C

IR-MCR OF ALKALI CHORIDE SALTS FROM CHAPTER 5

ATR-FTIR-MCR spectra of LiCl, NaCl, KCl, RbCl and CsCl are provided in Figure **C-1**. This compliments Figure **5-1** which shows, with Raman-MCR, that only Li^+ cations significantly perturb the O-H stretch vibration out of this set of monovalent salts.

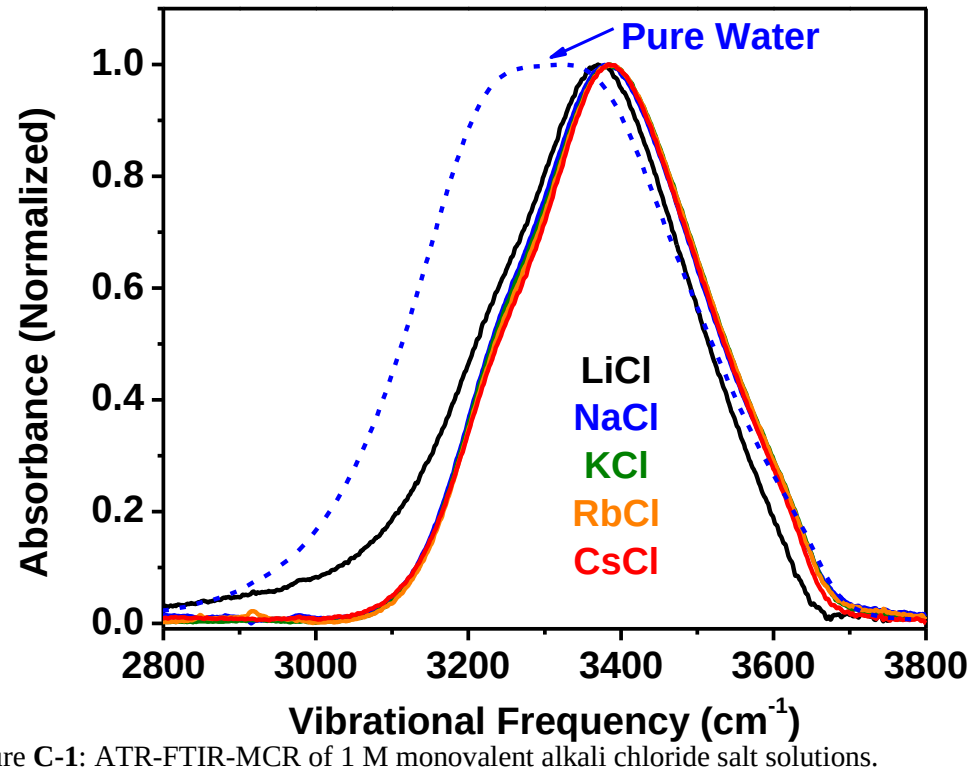

Figure **C-1**: ATR-FTIR-MCR of 1 M monovalent alkali chloride salt solutions.

The better sensitivity of IR-MCR highlights the stand out effect of Li^+ on its hydration shell compared to all other monovalent alkali cations. This is, still, much smaller than the contribution of Mg^{2+} to $MgCl_2$ in Figure **5-2**.

VITA

Chad Isaac Drexler

EDUCATION

The Pennsylvania State University (2015-2021)
Doctor of Philosophy – Chemistry
Research Advisor: Paul S. Cremer, Ph.D.

University of North Florida (2011-2015)
Bachelors of Science – Chemistry – Summa Cum Laude
Minor – Physics
Research Advisor: Thomas J. Mullen, Ph.D.

SELECTED ACADEMIC AND PROFESSIONAL AWARDS

1) Jane L. Apple Fellowship, Eberly College of Science, The Pennsylvania State University, University Park, PA (2020)
2) Young Investigator Lecturer, Chemistry and Physics of Liquids 2019, Gordon Research Conference, Holderness, NH (2019)
3) Graduate Student Teaching Fellowship, Department of Chemistry, The Pennsylvania State University, University Park, PA (2017)
4) Graduate Student Teaching Award, Troxwell Endowment Fund, Department of Chemistry, The Pennsylvania State University, University Park, PA (2016)
5) Outstanding Student Award, the American Institute of Chemists (2015)
6) NSF Research Experience for Undergraduates Fellowship, UC Merced's AiMM REU program, Merced, CA (2014)

PEER REVIEWED PUBLICATIONS

1) Bruce, E. E.[#]; Okur, H. I.[#]; Stegmaier, S.; **Drexler, C. I.**; Rogers, B. A.; van der Vegt, N. F. A.; Roke, S.; Cremer, P. S. Molecular Mechanism for the Interactions of Hofmeister Cations with Macromolecules in Aqueous Solution. *J. Am. Chem. Soc.* **2020**, *142* (45), 19094–19100.
2) **Drexler, C. I.**[#]; Miller, T. C.[#]; Rogers, B. A.; Li, Y. C.; Daly, C. A.; Yang, T.; Corcelli, S. A.; Cremer, P. S. Counter Cations Affect Transport in Aqueous Hydroxide Solutions with Ion Specificity. *J. Am. Chem. Soc.* **2019**, *141* (17), 6930–6936.
3) Okur, H. I.[#]; **Drexler, C. I.**[#]; Tyrode, E.; Cremer, P. S.; Roke, S. The Jones–Ray Effect Is Not Caused by Surface-Active Impurities. *J. Phys. Chem. Lett.* **2018**, *9* (23), 6739–6743.
4) **Drexler, C. I.**; Causey, C. P.; Mullen, T. J. 1-Adamantanethiol as a Versatile Nanografting Tool. *Scanning* **2015**, *37* (1), 6–16.
5) **Drexler, C. I.**[#]; Moore, K. B.[#]; Causey, C. P.; Mullen, T. J. Atomic Force Microscopy Characterization and Lithography of Cu-Ligated Mercaptoalkanoic Acid "Molecular Ruler" Multilayers. *Langmuir* **2014**, *30* (25), 7447–7455.
[#]Equal Contribution